© Copyright by Jiasong Li 2016
All Rights Reserved

Assessing the Biomechanical Properties of Cornea using Optical Coherence Elastography

A Dissertation

Presented to

The Faculty of the Department of Biomedical Engineering

University of Houston

In Partial Fulfillment

Of the Requirement for the Degree

Doctor of Philosophy

In Biomedical Engineering

by

Jiasong Li

May 2016

Assessing the Biomechanical Properties of Cornea using Optical Coherence Elastography

_____

Jiasong Li

Approved:

_____

Chair of the Committee
Kirill V. Larin, Professor,
Department of Biomedical Engineering

Committee Members:

_____

Metin Akay,
John S Dunn Endowed Chair

Professor,

Department of Biomedical Engineering

_____

Michael D. Twa, Professor and
Associate Dean
School of Optometry
University of Alabama at Birmingham

_____

Howard Gifford, Associate Professor,
Department of Biomedical Engineering

_____

Lowell T. Wood, Professor,
Department of Physics

_____

Suresh K. Khator, Associate Dean,
Cullen College of Engineering

_____

Metin Akay,
John S Dunn Endowed Chair
Professor and Chair,
Department of Biomedical
Engineering and Chair,

Acknowledgements

During the five years while completing my Ph.D., I have received infinite help, support, and encouragement from a great number of individuals. I want to express my deepest gratitude to my mentor, my advisor, Professor Kirill V. Larin, for his mentoring, guidance, caring, and support in every step of my progress. His incredible passion, perspective, and expertise in the field of biomedical optics and biomechanics illuminated my research and provided me with a broad vision.

I would like to thank my dissertation committee, Professor Metin Akay, Professor Michael D. Twa, Professor Howard Gifford, and Professor Lowell T. Wood for their assistance throughout my dissertation work.

I want to thank Professor Michael D. Twa and Srilatha Vantipalli for their essential support on many of the experiments, training of skills, shared experience of experiments, as well as their knowledge of the function and properties of eyes. I appreciate the great assistance provided by Dr. Salavat Aglyamov from Professor Stanislav Emelianov's group, Dr. Zhaolong Han, and Manmohan Singh, from our group, who helped me with many important experiments and offered in-depth discussions of the data.

I would like to thank all my colleagues and friends from the Biomedical Optics Laboratory. I appreciate Dr. Ravi Kiran Manapuram, Dr. Narendran Sudheendran, and Dr. Shang Wang for their nice guidance and suggestions when I just joined the group. I also thank Zlexander Schill, Chen Wu, Chih-hao Liu, Raksha Raghunathan, Floredes Menodiado, Tina Kazami, Thomas Hsu, Achuth Nair, and Shezaan Noorani, for working with me and bringing their expertise. None of my work can be achieved without any of you guys.

I would like to thank my wife, Shan Xu. She was always there cheering me up and stood by me through the good times and bad. I would like to thank my lovely daughter, Allison Yixuan Li, who made my work and life more fun, enjoyable, and motivated. Last but most, I owe my thankfulness to my parents, grand-parents, uncle and aunt, my sister, and all my relatives, for their unshakeable love and support.

Assessing the Biomechanical Properties of Cornea using Optical Coherence Elastography

An Abstract

of a

Dissertation

Presented to

The Faculty of the Department of Biomedical Engineering

University of Houston

In Partial Fulfillment

Of the Requirement for the Degree

Doctor of Philosophy

In Biomedical Engineering

by

Jiasong Li

May 2016

ABSTRACT

This dissertation reports on the development of measurement methods to assess the biomechanical properties of cornea based on low-coherence optical imaging, focusing on optical coherence elastographic techniques, to meet the growing demand for noninvasive high-resolution tissue characterization with improved diagnosis and treatment of ocular diseases. The research work was based on optical coherence tomography (OCT), a rapid, high-resolution, three-dimensional imaging modality that enables noninvasive depth-resolved imaging. The dissertation work is summarized in seven sections: 1) characterization the biomechanical properties of tissue mimicking phantoms, an ocular phantom, and mouse cornea *in vivo* using optical coherence elastography (OCE); 2) assessment the biomechanical properties of mouse corneas of different ages *in vivo* using air-pulse OCE; 3) the development of a method to spatially map the localized elasticity of the rabbit cornea *in situ* after partial riboflavin/UV-A corneal collagen cross-linking using OCE; 4) rapid characterization of the biomechanical properties of porcine corneas before and after UV-induced collagen cross-liking at different intraocular pressures by OCE; 5) the development of method to differentiate untreated and cross-linked porcine corneas of the same measured stiffness with OCE; 6) evaluation of the effects of Riboflavin/UV-A corneal collagen crosslinking on porcine corneal mechanical anisotropy with noncontact OCE; 7) a comparison of two non-contact methods to assess mechanical properties of tissue mimicking phantoms: optical coherence elastography and Michelson interferometric vibrometry. These techniques, methods and applications are demonstrated with the experiments performed on tissue mimicking phantoms (gelatin, agar, and silicone) and corneas (mouse, rabbit, porcine,

both *ex vivo*, *in situ*, and *in vivo*) under different conditions (normal vs. cross-linking, various intraocular pressures, etc.). This dissertation represents the frontier and emerging research area of optical coherence elastography and is expected to contribute to the field of biomechanical assessment with research and clinical based applications.

Table of Contents

Acknowledgements ..... **v**

ABSTRACT ..... **viii**

Table of Contents ..... **x**

List of Figures ..... **xv**

List of Tables ..... **xxi**

CHAPTER 1 – Introduction and Background **1**

1.1 Tissue characterization 1

1.2 The cornea 2

1.3 Common elastographic methods 3

1.4 Optical coherence tomography (OCT) 5

1.4.1 Time domain OCT (TDOCT) 8

1.4.2 Fourier domain OCT (FDOCT) 9

1.4.3 Spectral Domain OCT (SDOCT) 9

1.4.4 Swept Source OCT (SSOCT) 11

1.4.5 Phase-resolved OCT (PhS-OCT) 12

1.5 Optical Coherence Elastography (OCE) 13

1.6 Organization of this dissertation 16

CHAPTER 2 – Characterizing the biomedical properties of tissue mimicking phantoms, ocular model, and mouse cornea *in vivo* using OCE. **17**

2.1 Method 17

2.1.1 System setup 17

2.1.2 Experimental materials 18

2.1.3 Quantification methods 23

2.2 Results and discussion 24

2.2.1 Gelatin Phantom 24

2.2.2 Contact lens 27

2.2.3 Silicone eye model and in vivo study of 18-month-old mouse cornea 29

2.3 Conclusion 31

CHAPTER 3 – Air-pulse optical coherence elastography for assessment of the biomechanical property in mouse cornea of different ages *in vivo* 33

3.1 Introduction 33

3.2 Materials and Method 34

3.3 Results 36

3.4 Discussions 40

3.5 Conclusion 41

CHAPTER 4 – Elasticity localization after partial riboflavin/UV-A corneal collagen cross-linking in the rabbit using optical coherence elastography 43

4.1 Introduction 43

4.2 Materials and Method 45

4.2.1 Experimental materials and system setup 45

4.2.2 Quantification methods 48

4.3 Results 49

4.3.1 Tissue-mimicking agar phantoms 49

4.3.2 Corneal samples 51

4.4 Discussion 53

4.5 Conclusion 56

CHAPTER 5 – Characterizing the biomechanical properties of cornea before and after UV-induced collagen cross-liking at different intraocular pressures by optical coherence elastography 58

5.1 Materials and Method 58

5.2 Results 62

5.3 Discussion 67

5.4 Conclusion 70

CHAPTER 6 – Differentiating untreated and cross-linked porcine corneas of the same measured stiffness with optical coherence elastography 72

6.1 Introduction 72

6.2 Materials and Method 73

6.3 Results and discussion 74

6.4 Conclusion 79

CHAPTER 7 – Evaluating the effects of Riboflavin/UV-A corneal collagen crosslinking on porcine corneal mechanical anisotropy with noncontact optical coherence elastography 80

7.1 Introduction 81

7.2 Materials and methods 83

7.2.1 Experimental setup 83

7.2.2 Group Velocity Calculations 85

7.2.3 Anisotropy Calculations 86

7.3 Results 86

7.4 Discussion 95

7.5 Conclusion 100

CHAPTER 8 – Assessing mechanical properties of tissue phantoms with non-contact optical coherence elastography and Michelson interferometric vibrometry 101

8.1 Introduction 101

8.2 Materials and Method 102

8.3 Results 105

8.4 Discussion 108

8.5 Conclusion 112

CHAPTER 9 – Conclusion 113

References **115**

First Author Journal Publications **145**

List of Figures

Figure 1.1: Cross-section image of human eye……..…….3

Figure 1.2: Schematic of a conventional TDOCT system, ADC: Analog-to-digital card 8

Figure 1.3: Schematic of a typical SDOCT system……...10

Figure 1.4: Schematic of a typical SSOCT system……...12

Figure 2.1: Schematic of the system setup used for *in vivo* study of the mouse cornea biomechanical properties……...…….…19

Figure 2.2: (a) Physical dimension of the agar phantoms. (b) Excitation (red) and measurement positions (black)……..20

Figure 2.3: Experimental setup for contact lens experiments……....22

Figure 2.4: Image and physical of the silicone eye model in (a) top view and (b) side view……...…….....22

Figure 2.5: (a) Excitation and measurement locations in mouse cornea *in vivo*. (b) 3D OCT image showing relative position of the air-pulse port and the mouse cornea *in vivo*. The scale along the long-axis was 4.8 mm, the short-axis was 4.4 mm, and the z axis was 2.2 mm……23

Figure 2.6: Phase responses recorded at various measurement points away from the source of excitation in 14% gelatin phantom……...….….25

Figure 2.7: The group wave propagation velocity as a function of the concentration of gelatin (n = 9 for each concentration)…….....26

Figure 2.8: Typical delay map measured in 12% gelatin phantom ……..27

Figure 2.9: Young's moduli of gelatin phantoms calculated from the air-pulse induced elastic group wave velocity and as measured by the uniaxial mechanical testing system…….28

Figure 2.10: 2D rendered graph showing the time delay distribution on the surface of contact lens with 0.9% saline below the lens…….…….29

Figure 2.11: The measured time delay of elastic waves on (a) silicone phantom eye model and (b) 18-month-old mouse cornea *in vivo*…….30

Figure 3.1: (a) Dimensions of gelatin phantoms. (b) Five measurement positions near the center of phantom were randomly selected…….....36

Figure 3.2: Relaxation rate of 16% gelatin phantom with various excitation air-pulse pressure……..37

Figure 3.3: Relaxation rate of 8%, 12% and 16% gelatin phantom with 1.5 Pa air-pulse excitation.....38

Figure 3.4: Relaxation rate of gelatin phantoms in various concentrations. Three samples were measured for each concentration with five different positions in every sample…….……38

Figure 3.5: Sample signal from 12-month-old mouse *in vivo*.....39

Figure 3.6: Relaxation rate of the mouse cornea of different ages *in vivo*……...40

Figure 4.1 Schematic of experimental setup……..46

Figure 4.2: OCE measurement methods for the (a) homogeneous phantoms, and (b) heterogeneous phantom. For the heterogeneous phantom, the darker region was 2% agar (w/w) and the lighter regions was 1% agar (w/w). The yellow dots indicated the measurement positions..…….…….....46

Figure 4.3: OCE measurement methods for the corneas. Central brown circle indicates the masked (untreated) area. Yellow points indicate measurement locations. The rest area of the cornea was CXL treated……..…….……47

Figure 4.4: DNF maps in the homogeneous agar phantoms where the black dots represent the OCE measurement positions and the DNF scale is the same for direct comparison. DNF maps of the (a) homogeneous 1%, and (b) homogeneous 2%.....50

Figure 4.5: DNF map in the heterogeneous agar phantoms where the black dots represent the OCE measurement positions and the DNF scale is the same as figure 4.4 for direct comparison……..…..……50

Figure 4.6: A non-paired T test to compare of the square root of Young's modulus as measured by uniaxial mechanical testing to the DNF of the same concentration of homogeneous phantoms, and the corresponding heterogeneous phantom components. ……...…51

Figure 4.7: DNF maps of the rabbit corneal samples. Maps of the (a) control before CXL, (b) control after CXL. The black dots are OCE measurement positions and the DNF scales are the same for direct comparison……52

Figure 4.8: DNF map of a typical partially CXL rabbit cornea. The black dots are OCE measurement positions and the DNF scales are the same as Fig. 4.7 for direct comparison……..….52

Figure 4.9: Overview of the DNFs of the corneal samples where the blue and red boxes correspond to the virgin and CXL data sets from the corresponding samples. The central inscribed box is the mean, the central line is the median, and the boundaries are the 25% and 75%.....53

Figure 5.1: (a) Averaged CCT of UT and CXL corneas (n=4) at different IOPs. (b) Normalized central corneal thickness and linear fit of UT and CXL corneas at different IOPs…….....…….. 64

Figure 5.2: Three typical temporal displacement profiles on the cornea from OCE measurement positions at the indicated distances from the air-pulse excitation point. The elastic wave propagation and amplitude attenuation can be seen from the displacement profiles……65

Figure 5.3: (a) Elastic wave group velocity of untreated and cross-linked porcine corneas (n=4) as a function of IOP. (b) Young's moduli of corneas estimated by the shear wave equation 5.1 using the OCE measured elastic wave group velocity….....66

Figure 5.4: Typical relaxation process vertical temporal displacement profiles from a focused air-pulse induced deformation at the corneal apex from the same cornea before and after CXL treatment at an IOP of 25 mmHg…….…..67

Figure 5.5: (a) Relaxation rate of the UT and CXL corneas (n=4) as a function of IOP. (b) Young's moduli of the corneas obtained by the vertical displacement elasticity reconstruction method.....67

Figure 6.1: (a) EW velocities of the 14.0% gelatin (w/w) and 1.1% (w/w) agar phantom samples measured by PhS-SSOCE; (b) Comparison of estimated and measured Young's moduli of the 14.0% gelatin and 1.1% agar phantoms……75

Figure 6.2: (a) Normalized elastic wave displacement amplitude attenuation curves of the same 14.0% agar phantom at two excitation pressures; (b) Comparison of the normalized elastic wave displacement amplitude attenuation curves of 14.0% gelatin and 1.1% agar phantoms…….....76

Figure 6.3: Comparison of the normalized elastic wave displacement amplitude attenuation curves and exponential fit of an UT and CXL porcine cornea at the same measured stiffness but different IOPs.....78

Figure 7.1: (a) OCE experimental setup. (b) En-face view of a 3D OCT image of a porcine cornea. The red "X" indicates the excitation position and the arrows are elastic wave propagation directions that were imaged by the PhS-SSOCE system……..84

Figure 7.2: Group velocity polar maps of the air-pulse induced elastic wave for a pair of virgin porcine corneas ((a) and (b)) at different IOPs. 15, 20, 25, and 30 indicates the IOP in the unit of mmHg, and "+" indicates increasing IOP, and "-" indicates decreasing IOP……..88

Figure 7.3: Sample-wise mean velocity at different IOPs (n=4, 2 pairs of fellow eyes)……...89

Figure 7.4: Spatial map of the group velocity of the air-pulse induced elastic wave for a pair of virgin porcine corneas ((a) and (b)) at different IOPs. 15, 20, 25, and 30 indicates the IOP in mmHg, and "+" indicates the increase of IOP, and "-" indicates the decrease of IOP…….…….90

Figure 7.5: The r_θ values for each OCE measured angle in the cornea for a pair of virgin porcine corneas ((a) and (b)) at different IOPs. 15, 20, 25, and 30 indicates the IOP in mmHg, and "+" indicates the increase of IOP, and "-" indicates the decrease of IOP…….....91

Figure 7.6: Standard deviation of r_θ as quantified for all angles while IOP was cycled (n=4, 2 pairs of virgin porcine eyes)……92

Figure 7.7: Group velocity polar maps of the air-pulse induced elastic wave for a pair of porcine corneas ((a): Virgin and (b): CXL) at different IOPs. 15, 20, 25, and 30 indicates the IOP in mmHg, and "+" indicates increasing IOP, and "-" indicates decreasing IOP……..94

Figure 7.8: Mean velocity of a sample of all meridional angles at a given IOP of paired corneas where one eye was (a) Virgin and the fellow eye was (b) CXL……...95

Figure 7.9: Spatial map of the group velocity as calculated by the sliding window algorithm of the air-pulse induced elastic wave for a pair of porcine corneas ((a): Virgin and (b): CXL) at different IOPs. 15, 20, 25, and 30 indicates the IOP in mmHg……..96

Figure 7.10: Standard deviation of r_θ as quantified for all angles while IOP was cycled ((a), Virgin cornea, and (b) CXL cornea)…….. 97

Figure 8.1: Schematic of PhS-SSOCE experimental setup…….……....103

Figure 8.2: Schematic of LMIV experimental setup…….……..105

Figure 8.3: Sample surface responses of a 1% agar phantom recorded during (a) OCE and (b) LMIV experiment at the indicated distances from the air-pulse excitation….106

Figure 8.4: Elastic wave propagation velocity measured by OCE and LMIV. Statistical testing was performed by a paired t-test to demonstrate that the velocity measurements made by both systems were not different. The respective P-values are labeled……..107

Figure 8.5: Young's modulus (*E*) estimated by the OCE system, LMIV, and as measured by mechanical testing (MT)……..107

Figure 8.6: Phase velocity of the air-pulse induced elastic wave at 180 Hz in a sandwich-type agar phantom (top) with OCT image of the phantom (bottom). The layer boundaries are marked by the dashed red line…….110

List of Tables

Table 5.1: Young's moduli obtained by the elasticity reconstruction model utilizing the temporal vertical displacement profiles (estimated) and from uniaxial mechanical compression testing (measured)…….……....63

Table 6.1: PhS-SSOCE measured EW velocities of an UT and CXL cornea at different IOPs ……...77

Table 8.1: Approximate cost in $US of the OCE and LMIV systems used in this study…….…….112

CHAPTER 1 – Introduction and Background

1.1 Tissue characterization

Tissues can be characterized based on specific properties (such as optical, mechanical, electrical, etc), which can be assessed through qualitative and quantitative means [1]. Tissue properties provide crucial information for biological studies, disease diagnosis, and therapeutic intervention of various diseases. Specifically, tissue functions can be better understood with the knowledge of particular tissue properties. For example, the accurate measurement of the refractive index distribution in crystalline lens could assist the investigation of its contribution to the accommodation of the eye [2]. Aside from a fundamental understanding of physiology, tissue properties are useful for differentiating pathological tissue from normal tissue for predicting disease and guiding treatment through dynamic monitoring of the tissue properties. For instance, tumorigenesis increases the stiffness of tissue, and the tumor margin can be detected by mapping the mechanical contrast [3, 4].

One particular tissue property, its stiffness, provides an effective indicator for tissue characterization since various pathologies can affect tissue biomechanical properties, and subsequently can provide additional contrast between different types of tissues. The tissue elasticity is determined by the structure and composition of tissue [5]. Based on published results, it is clear that the elasticity variation is significant among different types of cells and tissues, which potentially can be used for contrast in tissue imaging and differentiation, providing the possibility of improved characterization of tissue [6-19].

The scale of elasticity measurement is very important as the tissue appears to have different mechanical properties at different scales [20]. For example, tumor cells have been found to have much lower Young's modulus compared with the healthy cells [21]. Conversely, solid tumors have higher stiffness than normal tissue at the macroscopic level, which can also be gleaned from palpation during physical examination or surgical resections [22]. Thus, techniques that enable micro-level measurement of tissue elasticity are required to better understand tissue functions and improve tissue characterization techniques for better diagnosis and treatment of diseases.

1.2 The cornea

A schematic of a human eye is shown in Fig. 1.1. The cornea is a critical component of the eye and forms the outermost layer, protects the eye from the outside environment, and provides most of the refractive power of the human visual system. The refractive power of the cornea is determined by three parameters: the intraocular pressure (IOP), the refractive index of cornea, and the shape of cornea. The biomechanical properties of cornea have been shown to be different under normal, diseased, and post-surgical states [23, 24]. Ectatic diseases such as keratoconus degenerate the pellucid margin, progressively reduce the thickness, distort and soften the cornea, which eventually can lead to uncorrected vision loss [25, 26]. Therefore, accurately assessing the biomechanical properties of cornea can help to identify the early stages of corneal degenerative diseases, such as keratoconus [27, 28].

Refractive surgeries, such as LASIK and PPK reduce the dependence on prescription eyeglasses or contact lenses for vision correction by altering the shape and refractive power of the cornea. In such procedures, the biomechanical properties of cornea are

noticeably altered [29-31]. Thus, actually measuring the biomechanical properties of cornea can help to track the outcome of these refractive surgeries or aid in planning and customizing personalized procedures.

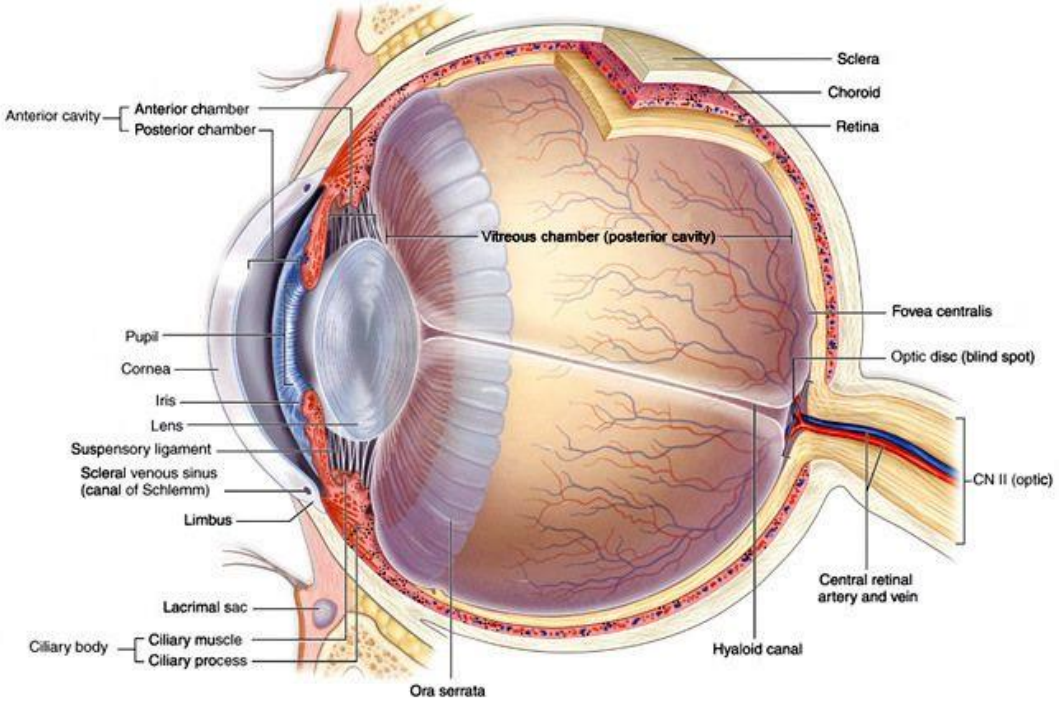

Figure 1.1. Cross-section image of human eye. (Public media of http://www.eyemedicalcare.com)

1.3 Common elastographic methods

A variety of imaging and detection techniques have been proposed and developed to characterize the mechanical properties of various tissues. For example, ultrasonic imaging utilizes the acoustic impedance of the tissue as the imaging contrast, x-ray imaging detects the attenuation of x-rays in tissue, and uniaxial compression or tension

tests measure the mechanical strength of the tissue [32-34]. Also, functional imaging approaches enable the detection of particular tissue properties in addition to the intrinsic contrast mechanism of the method, such as blood flow measurement using ultrasonic imaging [35]. Optical methods have several advantages and unique features that separate them from other tissue characterization techniques, such as high spatial resolution, highly-localized detection, no ionizing radiation, nondestructive imaging, and capability of *in vivo* real-time monitoring [36-40].

In the specific field of measuring the biomechanical properties of the cornea, the majority of techniques are based on inducing a deformation in the tissue and measuring the tissue response. The excitation can be provided by mechanical force, acoustic radiation force, or a pressure force produced by a pulsed laser [41-44]. Many imaging modalities, such as ultrasound imaging, magnetic resonance imaging, acoustic radiation force imaging, dynamic corneal imaging, and supersonic shear imaging, have been proposed to image the response of the cornea to an excitation [42, 44-57]. However, due to the relatively low spatial resolution, all of these methods require a significantly large amplitude of tissue displacement in order to produce a measurable signal, which may not be convenient for the cornea during *in vivo* studies. Holographic imaging has been used to study the elasticity of soft materials and tissues successfully. However, tissue motion may reduce the accuracy of this method in monitoring the deformation, which limits this method from *in vivo* applications [58]. Brillouin microscopy is another method that has been successfully used to achieve the depth-dependent biomechanical properties in the human cornea *in vivo*, and provides high resolution 3D elasticity maps of cornea [59-61]. This technique does not need an external excitation since it relies on Brillouin scattering.

However, translating the Brillouin signal to quantitative biomechanical parameters such as Young's modulus and viscosity is still an open question.

The Ocular Response Analyzer (ORA) and the CorVis are two clinically available methods to evaluate the biomechanical properties of cornea [62-66]. Both devices require a large amplitude air puff that displaces large volumes of tissue since they are marketed as devices for the measurement of intraocular pressure. The large displacement introduces a significant nonlinear component to the measured properties, and results from recent clinical studies demonstrated the inability of ORA to identify keratoconus-suspect corneas [63, 67].

Optical coherence tomography (OCT) is a noncontact, rapid, high-resolution, 3-D, well-developed, and widely used imaging modality that has become a staple in ophthalmology [68]. Thus, OCT can overcome the limitation of spatial resolution of previous techniques to significantly reduce the amplitude of the externally induced displacement for characterizing the biomechanical properties of the cornea. This dissertation examines its application for high-resolution noninvasive assessment of corneal biomechanical properties.

1.4 Optical coherence tomography (OCT)

OCT was introduced to the field of ophthalmology to noninvasively image the cross-section of human retina with micron-scale spatial resolution in 1991 [68]. After 25 years of development, OCT has been applied in many research and clinical areas, such as intravascular imaging, blood flow detection and velocimetry, cancer imaging, developmental biology, elastography, dermatology, and dentistry [69-75]. Besides the

noninvasive detection and the three-dimensional imaging, OCT has three particular features that allow for extensive development and applications:

1) High spatial resolution. Because OCT a broadband light source, which results in a limited coherence length. This translates to 1-10 μm of axial resolution [76]. By adopting various signal processing techniques, the spatial resolution can be improved to nanometer level [77].

2) Millimeter-scale imaging depth in highly scattering media such as tissue. By utilizing near-infrared light, with wavelengths usually between 800 nm and 1700 nm, the penetration depth of ballistic photons inside the tissue can reach a few millimeters, which enables OCT to maintain sufficient depth of imaging in many applications with high resolution [78].

3) Fast acquisition speed. Taking advantage of the fast-paced development of laser hardware, the OCT imaging rates are now primarily limited by detectors and acquisition hardware. Currently the fastest non-multiplexed OCT system can reach 28 million A-lines per second [79].

OCT is based on low-coherence interferometry (LCI), which was developed to characterize optical components with high axial resolution by measuring the field of the optical beam rather than its intensity [80]. The functional form of the electric field in a light wave is

$$E(t) = E_0 \cos(2\pi \nu t - \frac{2\pi}{\lambda} z), \tag{1.1}$$

where ν is the frequency of the wave, t is the time of propagation, λ is the wavelength, and z is the propagation distance. In a simple Michelson interferometer, the reference beam field $E_r(t)$ coherently combines with the sample arm field $E_s(t)$ and interferes to

form fringes. If Δl is the path length difference between two light beams, the interference signal can be expressed as

$$I_0(t) = |E_r(t) + E_s(t)|^2 = |E_r|^2 + |E_s|^2 + E_r E_s \cos(2\frac{2\pi}{\lambda}\Delta l), \qquad (1.2)$$

where the cosine term contains the interference information, and Δl suggests that the modulation frequency of the interference depends on the difference in path lengths between the two fields. It also shows that a sharp cosine envelope or a short time duration cosine term can resolve small changes in the path length. Therefore, depth information can be resolved with spatial resolution on the order of the wavelength.

The axial resolution of OCT, l_c, can be expressed based on the central wavelength and the bandwidth of the light source [81]

$$l_c = \frac{2ln2 \cdot {\lambda_0}^2}{\pi \Delta\lambda}, \qquad (1.3)$$

where λ_0 is the central wavelength of the light source, and Δl is the FWHM of the laser spectrum, known as bandwidth. Equation 1.3 clearly demonstrates the relationship between axial resolution and the laser source spectrum. Specifically, a larger bandwidth and smaller central wavelength results in a superior axial resolution. However, it is known that longer wavelengths of light can penetrate deeper inside biological tissue (within so called therapeutic window, which ranges between ~ 800 nm and 1300 nm), particularly wavelengths with low water absorption. However, longer wavelengths require significantly broader spectra to obtain similar axial resolutions and thus, there is a tradeoff between axial resolution and imaging depth.

1.4.1 Time domain OCT (TDOCT)

The basic principle of the first generation OCT, which is termed Time Domain OCT (TDOCT), is to detect backscattered photons from a tissue of interest within a coherence length of the source using a two-beam interferometer, as shown in Fig. 1.2 [68]. A broadband low-coherent laser light source is split into two beams by a 50/50 beam splitter. The two arms are usually referred to as the reference arm, which has a mirror, and the sample arm, which is directed at the object of interest. The back-scattered light from the sample arm combines with the reflected light from the reference arm to generate the fringe. Because of the low coherence of the light source, interference will only occur when the optical path length difference between two arms does not exceed the coherence length of the laser source. The fringes are then recorded by a photodetector.

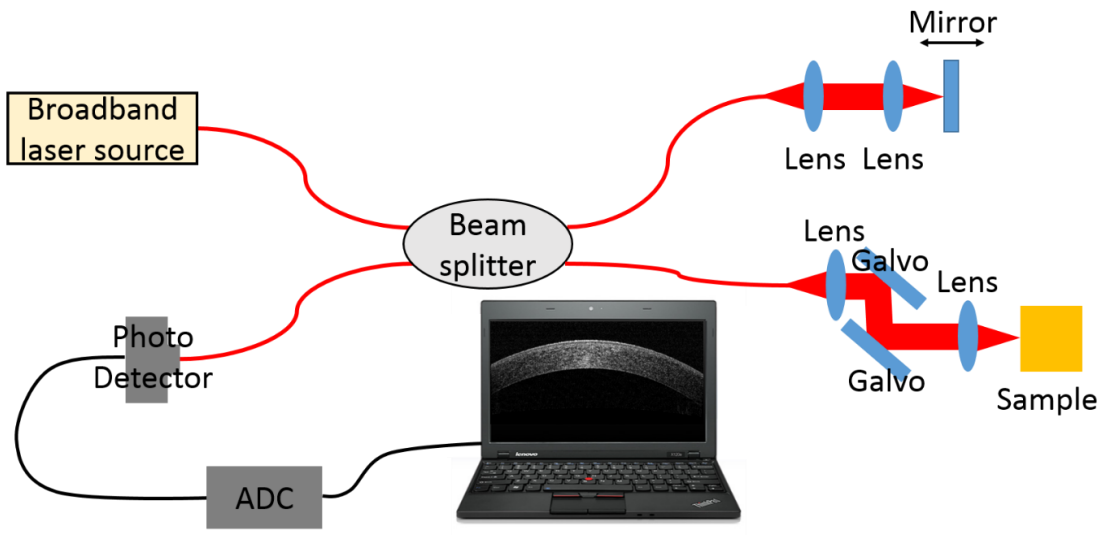

Figure 1.2. Schematic of a conventional TDOCT system, ADC: Analog-to-digital card.

In TDOCT, the mirror in reference arm is translated back and forth to measure the echo time delay of the back-scattered light from the sample (Fig. 1.2). Back scattered

light from the various depths is obtained at different times corresponding to the mirror movement, making the information time encoded. The interference signal at different transverse points of the sample is collected by scanning a pair of galvanometer-mounted mirrors. Thus, 3D cross-sectional images can be constructed.

1.4.2 Fourier domain OCT (FDOCT)

The next major development in OCT was improving the acquisition speed by eliminating the need for translating the reference arm to obtain depth information with the added benefit of improved detection sensitivity. This new OCT technique was termed Fourier Domain OCT (FDOCT) [82]. As with TDOCT, FDOCT also utilizes a broadband source, but now the depth information is spectrally encoded by the modulation frequencies of the interference spectrogram. FDOCT is further sub-divided into Spectral Domain OCT (SDOCT) and Swept Source OCT (SSOCT).

1.4.3 Spectral Domain OCT (SDOCT)

An SDOCT system is very similar to a TDOCT system. However, instead of a photodetector, the spectrum of the interference signal is detected by a grating-based spectrometer and a high-speed line-scan charge-coupled device (CCD) detector. Fig. 1.2 shows an SDOCT schematic. After discarding the constants, the detected fringe signal can be expressed as [83]

$$I(k) = s(k)\sqrt{I_1 I_2}\cos(2nk\Delta x), \tag{1.4}$$

where $k=2\pi/\lambda$ is the wavenumber, λ is the wavelength, $I(k)$ is the intensity of the interference signal in term of k, $s(k)$ is the power spectrum of the light source (same for both of the reference arm and sample arm), I_1 and I_2 are the intensity of light from both arms, and $n\Delta x$ is the optical path length difference between two arms scaled for

refractive index *n*. By performing a Fourier transform on equation 1.4, the back scattered light intensity at each depth can be resolved.

The sensitivity of OCT is given by

$$S = \frac{\eta P T_{exp}}{h\nu}, \tag{1.5}$$

where η is the detector efficiency, P is the light power incident on sample, T_{exp} is the exposure time, and $h\nu$ is the photon energy. In SDOCT, the exposure time is approximately the same as axial scan time, $T_{exp} = T_{ascan}$. In TDOCT, light from different depths is detected sequentially, which means the exposure time of one axial scan is equally split on m positions (where m is the resolvable element in one axial scan), thus, the exposure time of one position is $T_{exp} = T_{scan}/m$. Therefore, FDOCT has a significant advantage over TDOCT in terms of system detection sensitivity [84]. Currently, the A-line speed of SDOCT is predominantly limited by the speed of CCD.

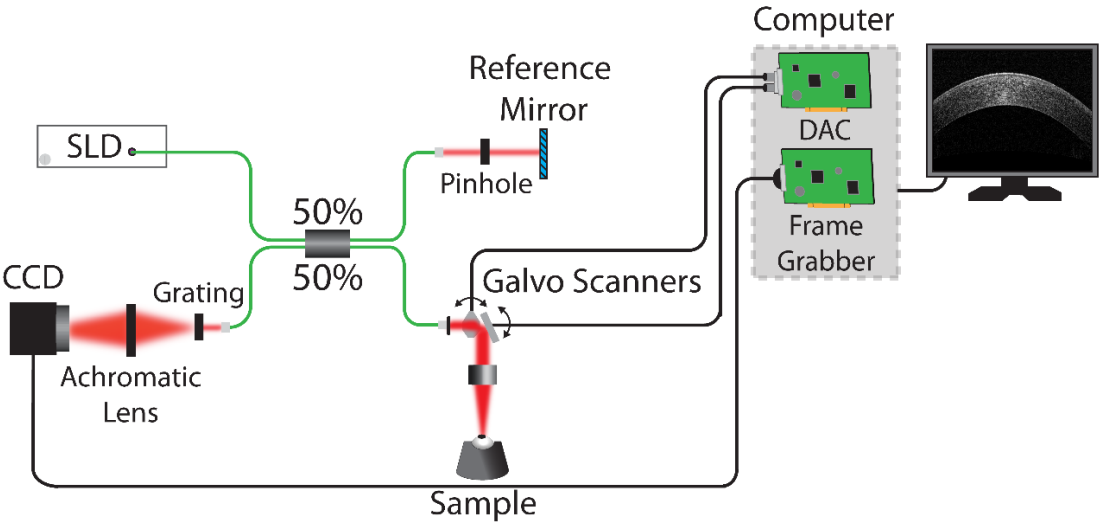

Figure 1.3 Schematic of a typical SDOCT system.

1.4.4 Swept Source OCT (SSOCT)

As I have described previously, the penetration depth of ballistic photons determine the effective imaging depth of an OCT system. However, in an FDOCT system, the full imaging depth also relies on how well the wavelength information is separated and sampled, which can be considered as the sampling frequency of the signal in equation 1.4. The imaging depth of FDOCT in air, *D*, has been derived as [85]

$$D = \frac{\lambda^2}{4\delta\lambda}, \tag{1.6}$$

where λ is the central wavelength, and $\delta\lambda$ is the wavelength sampling.

Equation 1.6 clearly suggests that besides the central wavelength of the system, how well the wavelengths are sampled also affects the theoretical imaging depth. In SDOCT, the resolving capability is limited by the total number of pixels in the detector in the spectrometer. Currently, there are commercially available line-scan cameras with up to ~16,000 pixels at line-scan speeds of 100,000 lines/s. However, these detectors are not cost-effective for the majority of applications.

A swept source laser, which chirps the broadband light into very narrow line width pulses ($\leq$ 0.1 nm) over time, has been utilized for OCT in swept source OCT (SSOCT). Similar to TDOCT and SDOCT, the light from a broadband swept source laser source is split into the sample arm and reference arm in an SSOCT system. The returning light from both arms is coupled into a 50/50 fiber coupler to form the interference fringes. Instead of using a CCD to record the fringes as in SDOCT, a balanced photodetector is used to record the light intensity over time, and the acquisition is precisely synchronized with the swept laser to obtain the spectral interferogram. The fastest speed of commercially available balanced photodetectors are in the order of GHz. Thus, one of

the advantages of SSOCT compared with spectroscopic SDOCT is the higher possible imaging depth. Moreover, ultrafast balanced photodetector are in order of magnitudes more cost effective than high-speed, high-resolution line-scan cameras. Moreover, SSOCT sources are primarily in the 1300 nm range, which provides greater depth penetration in tissue than the majority of SDOCT sources, which are in the 800 nm range.

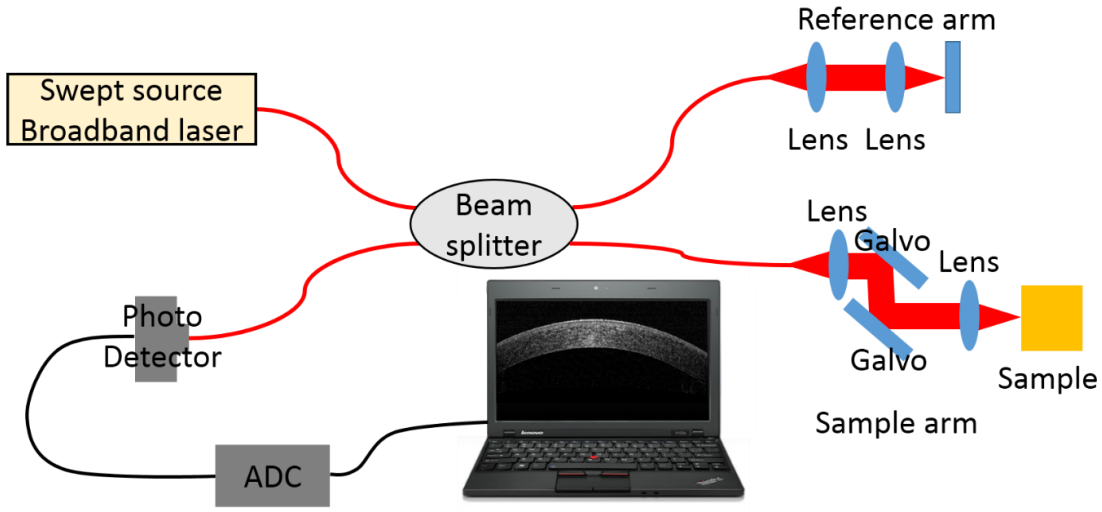

Figure 1.4 Schematic of a typical SSOCT system.

1.4.5 Phase-resolved OCT (PhS-OCT)

The typical axial resolution of OCT is at the micrometer level. However, by analyzing the phase information from interference signal, the sensitivity of OCT to detect sample displacement can reach nanometer scale, and PhS-OCT has been applied to various applications, such as cell biology, angiography, elastography, and more [86-90].

The sensitivity of PhS-OCT measurements relies on the phase stability of the system, which mainly depends on the presence of mechanical moving parts in the system in addition to the inherent phase stability of laser source. Since TDOCT has an axially moving mirror in the reference arm, the phase stability of TDOCT is inferior to FDOCT.

In the case of SSOCT, a mechanical mirror sweeps inside the laser to generate the different narrow bands of light that ultimately form the broadband light. In an SDOCT system, there is generally no mechanical movement apart from the scanning mirrors, therefore, the phase stability of SSOCT is generally worse than SDOCT. Due to this reason, most of the early phase-resolved investigations utilized SDOCT, most commonly known as spectral domain phase microscopy (SDPM), which is capable of providing picometer scale sensitivity [86]. However, the A-line speed of SDOCT is limited by the speed of CCD camera, and thus, SDOCT is implemented in the wavelength range around 800 nm due to the relatively high cost of high speed line-scan InGaAs cameras that are required to detect longer wavelengths. In order to take advantage of longer wavelengths that allow deeper penetration, phase resolved techniques have been implemented in SSOCT as well, even though the phase stability offered by SSOCT is lower compared to SDOCT mainly due to the instabilities in the swept laser source [91]. Therefore, in order to achieve adequate phase sensitivity, phase stabilized techniques have been developed and adopted into phase-resolved SSOCT systems [92].

1.5 Optical Coherence Elastography (OCE)

Optical Coherence Elastography (OCE) is a rapidly developing technique that focuses on the micro-scale assessment of tissue elasticity [93] and has potential to become useful in numerous clinical applications varying from ophthalmology to cardiovascular imaging [94-96]. OCE was introduced by Schmitt in 1998, who utilized OCT to measure the microscopic deformation of biological tissue under compressive stress induced by a piezoelectric actuator [97]. Two-dimensional cross-correlation speckle tracking measured the internal tissue displacement with micrometer-scale. This

work also provided the first demonstration for the *in vivo* application of OCE on human skin.

Similar to the other elastography methods briefly introduced in section 1.3, a conventional OCE system is a combination of loading system that induces displacement in tissue, and an OCT system to image the deformation. By analyzing the tissue response to the excitation, biomechanical properties can be assessed by utilizing appropriate mechanical models. With the application of phase-solved OCT, the detection accuracy of OCE can achieve nanometer scale [90, 98-106]. Currently, OCE techniques are primarily based on three types of techniques for quantifying tissue biomechanical properties: 1) the local displacement or strain inside the tissue under compressive stress, 2) the resonance frequency of the oscillation in tissue, 3) analyzing the propagation of an elastic wave. The focus of this dissertation is to quantify the biomechanical properties of cornea. Utilizing the first technique, the sample must be mechanically compressed, which is not very suitable for *in vivo* use. Nevertheless, compressional OCE has shown promise in research applications [107, 108]. Oscillations can be induced in tissue with nanoparticles in a magnetic field or by acoustic excitation. However, introducing nanoparticles into the cornea is not feasible for clinical applications and sound waves introduce complexity for quantitative biomechanical characterization because the geometry of the sample significantly determines how the sample responds to the sound waves [109-111]. Acoustic radiation force can also provide excitation, but requires a transmission medium such as a gel or direct contact with the cornea, which may not be suitable for live imaging [112]. Therefore, this dissertation is primarily focused on analyzing the propagation of an elastic wave in corneal tissue to obtain the quantitative

biomechanical properties of the cornea as the elastic wave can be induced completely noninvasively with a micro air-pulse [113-116].

To study the biomechanical properties of the cornea, various dynamic OCE techniques have been developed. Qu. et al. utilized acoustic radiation force for excitation and phase-resolved OCT to image the corneal response [112]. Three dimensional elastograms of a healthy and a highly cross-linked cornea were obtained, and a partially stiffened region of a cornea was also resolved. However, the whole cornea was submerged in liquid or ultrasound gel, which limits the application of this method for live imaging. Song et al. introduced using single-shot laser to induce the displacement in cornea, which was imaged by OCT [117]. The propagation speed of the induced elastic wave was successfully estimated, which can be further converted into Young's modulus by appropriate mechanical models. Nonetheless, an ultraviolet light source (263 nm) was used to induce the elastic wave in cornea. Considering the laser safety exposure limits for the cornea, there was a tradeoff between excitation power and the wave amplitude. In this study, the largest amplitude was achieved as ~80 nm, and thus, the wave only propagated a very short distance, which means that this method may not be suitable for providing the elasticity information of the whole cornea. Mechanical excitation was introduced by Manapuram et al. [90]. A metal wire with a rounded tip was attached to a speaker to excite the mouse cornea periodically *in vivo*. A 2-D map of the propagation speed of the elastic wave, as well as the amplitude attenuation were obtained. However, this method required physical contact on the cornea. Thus, an OCE system with the ability of noncontact, noninvasive, minimal amplitude excitation, high sensitivity, and fast A-line speed is highly desired in the field of corneal biomechanics.

1.6 Organization of this dissertation

This dissertation is focused on the development of novel OCE techniques to noninvasively assess the biomechanical properties of cornea with high resolution and their applications.

In chapter 2, the biomechanical properties of cornea *in vivo* were characterized by OCE with a focused air-pulse excitation. In chapter 3, The OCE system and measurement methodology were improved to assess the changes in the biomechanical properties of mouse cornea *in vivo*. In chapter 4, the localized air-pulse method was applied to map the stiffness of cornea before and after cross-linking and after spatially heterogeneous cross-linking. In chapter 5, a faster and more quantitative method was developed to estimate the overall elasticity of cornea at different IOPs. In chapter 6, an algorithm to differentiate samples of the same measured elasticity is detailed. In chapter 7, a method with the capability to spatially map the shear elasticity of the cornea and determine the shear anisotropy is described. In chapter 8, a low-cost alternative interferometry technique is introduced for elastographic assessment and compared with OCE. In chapter 9, the conclusion of this dissertation is presented with the implications of future work.

CHAPTER 2 – Characterizing the biomedical properties of tissue mimicking phantoms, ocular model, and mouse cornea *in vivo* using OCE.

In this chapter, a phase-stabilized swept source optical coherence tomography system was utilized to detect the propagation of low-amplitude (micron-level) elastic waves in tissue mimicking gelatin phantoms, an ocular phantom, and mouse corneas *in vivo*, which was induced by a focused air-pulse delivery system. The group velocity of the wave propagation in tissue mimicking phantoms was estimated and further converted to Young's modulus using the mechanical model of a surface wave. The measured group velocity was faster in higher concentration of gelatin phantoms, and the estimated Young's moduli of these phantoms matched the stiffness as assessed by mechanical testing. For the ocular model and cornea samples, 2D maps of the elastic wave propagation time delay were plotted, which potentially can be converted to elasticity maps with appropriate reconstruction models. Therefore, this non-contact measurement technique utilizes low-force tissue excitation that potentially can be used to assess the biomechanical properties of ocular and other delicate tissues *in vivo*.

2.1 Method

2.1.1 System setup

Elastic waves are induced in the sample using a home-built air-pulse delivery system that produces a focused air stream with a duration of <1 ms [118]. The spatial-temporal profile of the air pulse is characterized as a Gaussian shape. Briefly, the system employs an air gate and a control unit to provide the short-duration air–pulse. An extra channel for signal output from the control unit allows proper synchronization with the PhS-

SSOCT measurement system. The air source pressure can be obtained from a pressure gauge, and the air-pulse is expelled out of a cannula port with a flat edge and inner diameter of ~150 μm. The localized air-pulse excitation can be precisely positioned with a 3D linear micrometer stage. This enables a highly localized noncontact excitation for studying the biomechanical properties of the cornea completely noninvasively when combined with OCT.

A PhS-SSOCT imaging system was combined with this air-pulse system to detect air-pulse elastic waves in the sample. The schematic of the experimental setup for the *in vivo* study of mouse cornea is shown in Fig. 2.1. Briefly, the PhS-SSOCT system was comprised of a broadband swept laser source (HSL2000, Santec, Inc., USA) with the central wavelength of 1310 nm, the bandwidth of ~150 nm, the scan rate of 30 kHz, and the output power of ~36 mW. Interference was produced by the back-scattered light from the sample and reflected light from the reference arm, and the fringes were detected by a balanced photodetector. A fiber Bragg grating was used for triggering the A-scan acquisition to reduce the phase noise. Details of the system description can be found in previous publications [90-92]. The axial resolution of the system was ~11 μm, and the phase stability of the system was experimentally measured to be ~16 mrad (corresponding to ~3.3 nm displacement in air). The air-pulse system generated a TTL signal which was recorded by the analog-to-digital converter (ADC) to synchronize the PhS-SSOCT system and the focused air-pulse delivery system.

2.1.2 Experimental materials

In order to simulate soft tissue samples of controlled stiffness, gelatin phantoms of five different concentrations (8%, 10%, 12%, 14% and 16% w/w) were prepared. Gelatin

powder (PB Leiner, 250 Bloom / 8 Mesh) was mixed with distilled water at 60 ℃ until all granules were dissolved. Special care was taken while stirring the mixture to avoid the formation of air bubbles. The mixture was poured into a round mold to create a disk that was ~11 mm thick and ~33.5 mm in diameter (Fig. 2.2). The hot gelatin was cooled in a refrigerator (~ 10 ℃) for 30 minutes [119]. The solidified gel formed a solid slab that served as a tissue-mimicking sample with controlled elastic properties. During phantom experiments, the distance between the excitation position and the first measurement position was greater than 1 mm, and 1 mm between two adjacent measurement positions.

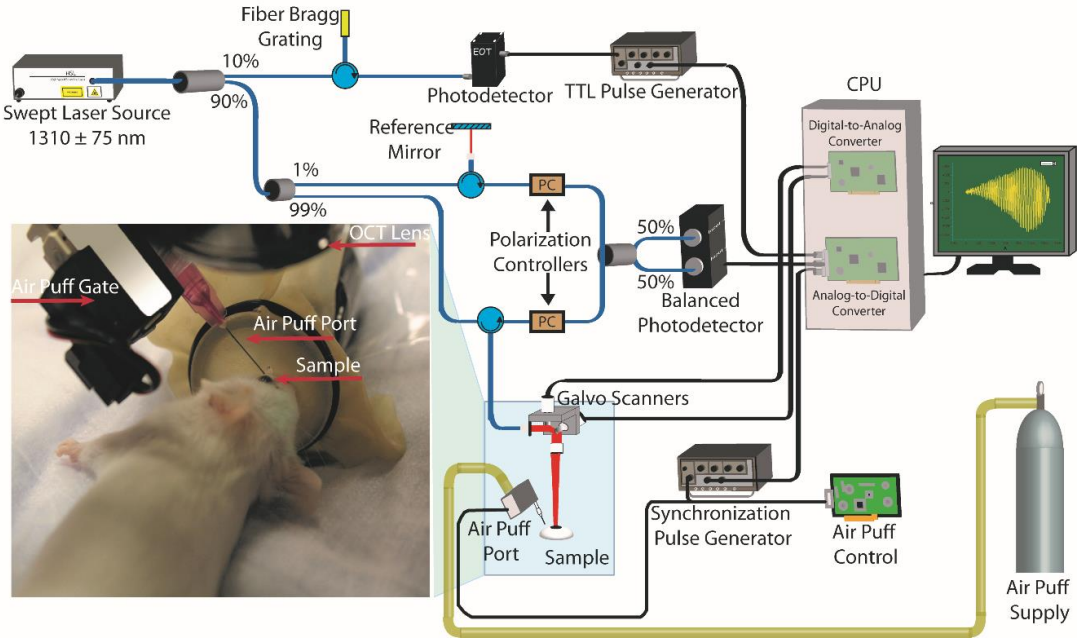

Figure 2.1. Schematic of the system setup used for *in vivo* study of the mouse cornea biomechanical properties.

A contact lens was used an analog of the cornea to evaluate the feasibility of the OCE measurement technique on a thin curved sample. The contact lens was a commercially available lens (Bausch & Lomb, Slisoft + 12.00D, 100% Silicone) that has a shape

similar to the cornea and has homogeneous optical and mechanical properties. During the experiments, the contact lens was fixed on a flat plate, and the space between the contact lens and the plate was filled with 1X Phosphate buffered saline (PBS) simulating the aqueous humor (Fig. 2.3).

A custom-made silicone model of an eye was also used to further demonstrate the feasibility of the OCE measurement technique for assessing corneal biomechanical properties (Fig. 2.4). This model had an anterior surface with a similar curvature and size as the human eye. However, it had homogeneous optical and mechanical properties.

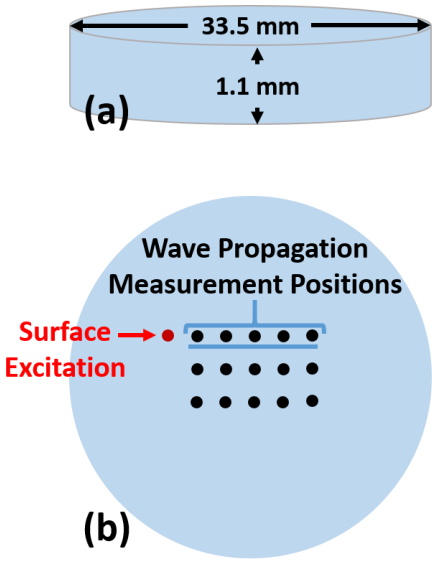

Figure 2.2. (a) Physical dimension of the agar phantoms. (b) Excitation (red) and measurement positions (black).

In vivo measurements were performed on the corneas of three anesthetized mice (15-22 months old, Fig. 2.5). The cornea was kept hydrated by the periodical application of 0.9% saline solution every 2 minutes during experiments. All the animal manipulation procedures were approved by the Animal Care and Use Committee of the University of Houston.

Surface waves were excited with an air pressure of ~10 Pa for the gelatin phantoms and silicone eye model, ~2.2 Pa for the contact lens, and ~5.9 Pa for mouse corneas *in vivo*. These pressures were chosen to ensure the amplitude of the induced wave was large enough to be detected without causing any damage to the sample. During all experiments, the distances between the tip of the air-pulse delivery system port and the sample surface were kept within 0.3 mm, and the surface waves were monitored in the sample within the anterior 11 μm of the sample surface. Our investigation has shown that the air pressure of the system output remains relatively stable with the distance change within 10 mm between the port tip and the sample surface [118]. M-mode imaging, which is holding the OCT probe beam and acquiring data over time, was performed at different transverse positions (M-B-mode scanning). The spatial distribution of the excitation position and OCE measurement positions on the samples are shown in Fig. 2.2 and Fig. 2.5. The distance between the excitation point and the first measurement point was greater than 1 mm. The distance between two adjacent recording positions was 1 mm during the gelatin phantom, contact lens, and silicone eye model studies, and 0.3 mm during *in vivo* studies.

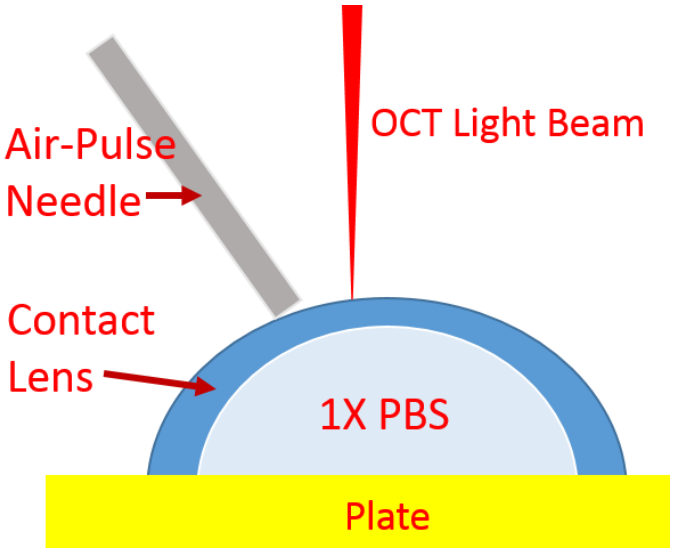

Figure 2.3. Experimental setup for contact lens experiments.

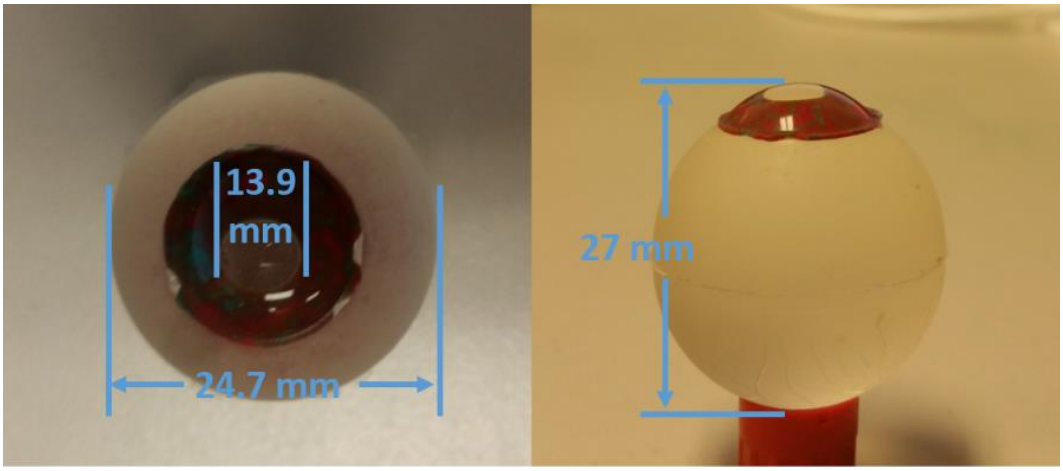

Figure 2.4. Image and physical of the silicone eye model in (a) top view and (b) side view.

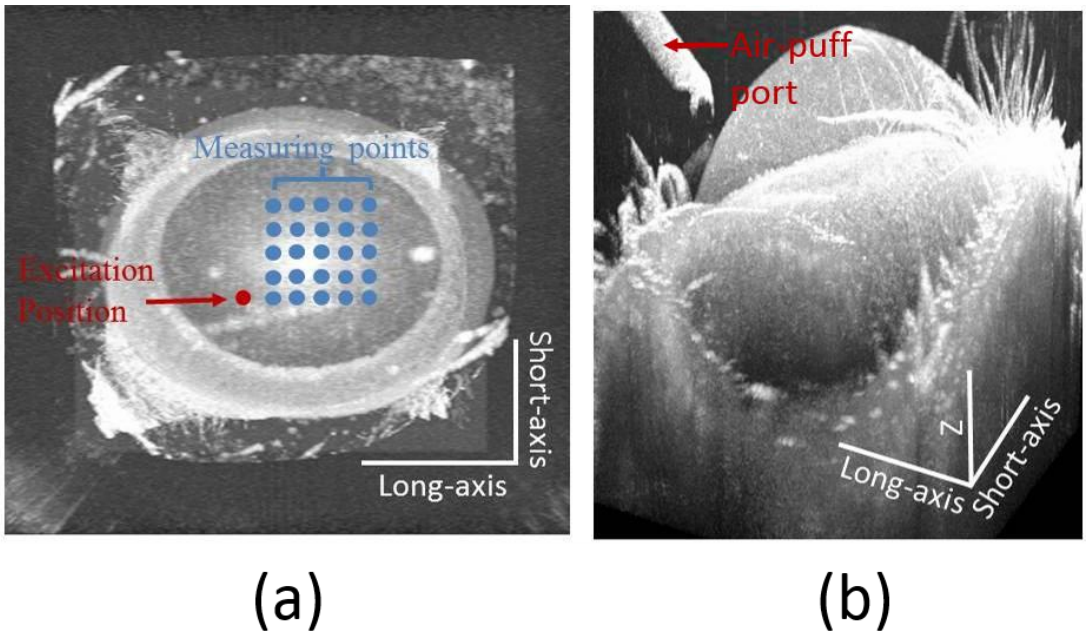

Figure 2.5. (a) Excitation and measurement locations in mouse cornea *in vivo*. (b) 3D OCT image showing relative position of the air-pulse port and the mouse cornea *in vivo*. The long-axis scale was 4.8 mm, the short-axis was 4.4 mm, and the z-axis was 2.2 mm.

2.1.3 Quantification methods

To calculate the amplitude of the surface waves, $d(t)$, from phase measurements, $\phi(t)$, the following equation was used [102]

$$d(t) = \frac{\lambda}{2\pi} \times \phi(t), \tag{2.1}$$

where λ was the central wavelength of the OCT system.

The velocity of the elastic wave c was calculated as

$$c = \frac{d}{t}, \tag{2.2}$$

where d was the distance between the measurement points, and t was the time delay of the elastic wave between two measurement positions. The displacement peak was used to calculate the time delay. The time delay was defined as the difference between the

time of the onset of air pulse and the time of surface wave arrival measured at the main peak. The calculations were based on each pair of adjacent points. Therefore, the velocity was calculated as 1 mm (0.3 mm in mouse cornea *in vivo* study) divided by the elastic wave propagation time delay difference between two adjacent points.

Assuming that the phantoms were isotropic homogeneous elastic materials, the Young's modulus, *E*, of the phantoms can be calculated based on the wave velocity *c* as follows [120]

$$E = 2\rho(1+\nu)\cdot[\frac{c\cdot(1+\nu)}{0.87+1.12\nu}]^2, \quad (2.3)$$

where ρ was the mass density and ν was the Poisson's ratio of the medium. Although this equation was derived for a half-space structure, it was utilized for a first-order approximation of Young's modulus of the gelatin phantoms based on the group velocity of the surface waves measured in the experiment.

For the studies on contact lens, silicone eye model, and *in vivo* mouse cornea, the time delay was calculated relative to the position that was the nearest to the estimated excitation point and 2D rendered maps of time delay were generated.

2.2 Results and discussion

2.2.1 Gelatin Phantom

Figure 2.6 shows typical amplitudes of the surface waves propagating in the 14% gelatin phantom recorded at various measurement locations. The data clearly demonstrate that the amplitude decreases and the wave propagation time delay increases at measurement positions further from the excitation. While the spatial-temporal profile of the air pulse was characterized as a Gaussian pulse, it was not normal to the specimen surface due to the size of the OCT scan lens. It is possible that the angular separation of

the air pulse and the measurement axis (approximately 30 degrees in this experiment) may influence the shape and force of the stimulus, thereby producing additional frequencies (the small amplitude vibration before the large deformation).

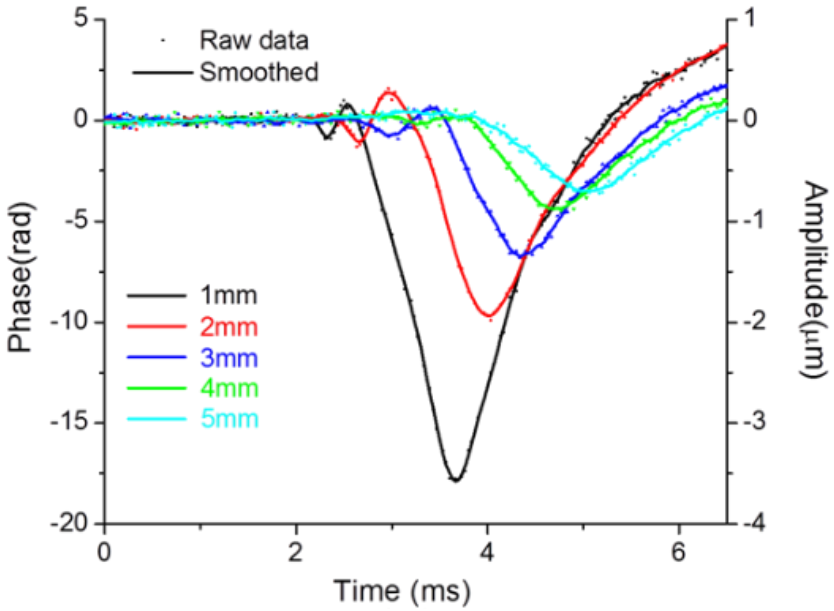

Figure 2.6. Responses recorded at various measurement points in 14% gelatin phantom.

Figure 2.7 shows the velocity of the surface waves measured in gelatin phantoms of different concentrations. The data indicates that the wave propagation group velocity increased with increasing concentration of gelatin, corresponding to a positive correlation between sample stiffness and gelatin concentration, which was consistent with previous work [102]. A typical delay map of 12% gelatin phantom is shown as Fig. 2.8, which also indicates that the wave propagation time delay increased for further OCE measurement positions.

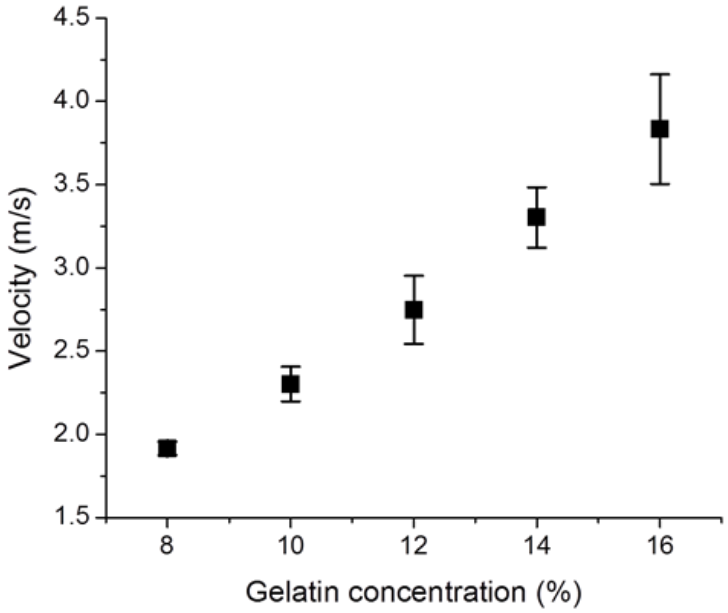

Figure 2.7. The wave propagation group velocity as a function of gelatin concentration (n = 9 for each concentration).

The Young's moduli of the gelatin phantoms are presented in Fig. 2.9. For quantification, the density (ρ) of gelatin phantoms was assumed to be 1000 kg/m^3 and a Poisson's ratio (v) of 0.5 was used to obtain Young's modulus (E) from equation (2.3) [121]. The estimated Young's moduli of 8%, 10%, 12%, 14% and 16% gelatin phantoms were 12.2±0.6 kPa, 17.5±1.6 kPa, 25.1±3.8 kPa, 36.1±4.0 kPa, and 48.8±8.2 kPa, respectively. Additionally, a uniaxial mechanical testing system (In-Spec 2200, Instron, Inc., USA) was used to measure the Young's moduli of gelatin phantoms of the same concentrations (Fig. 2.9). It can be easily seen that the estimated Young's moduli obtained from the wave velocity using OCT are reasonably close to those measured by the uniaxial testing system. The small differences may be attributed to the fact that the surface wave equation does not take account of the finite thickness of the phantom [122].

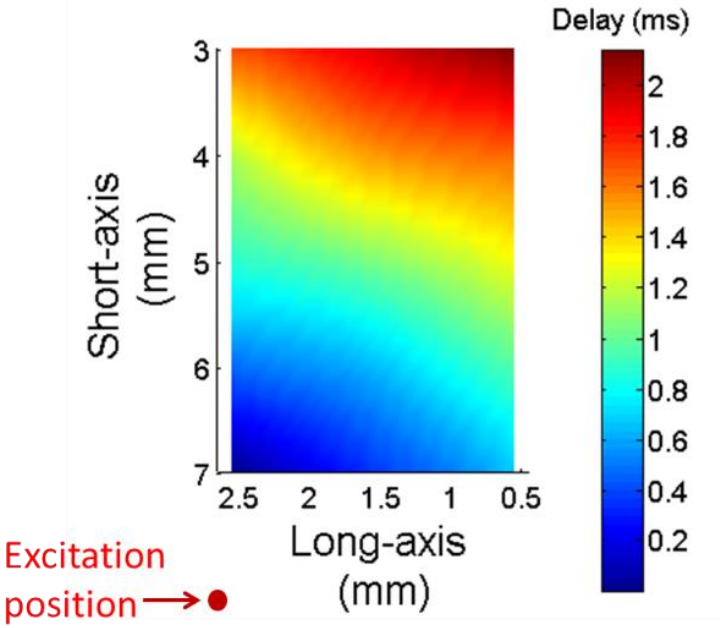

Figure 2.8. Typical delay map measured in 12% gelatin phantom.

2.2.2 Contact lens

The experiment with contact lens was performed with 0.9% saline solution placed between the contact lens and the supporting plate. Fig. 2.10 shows 2D rendered map of time delay of the elastic waves in the contact lens. The result shows that the delay increases with greater distance in the contact lens and then decreases for OCE measurement positions beyond the apex.

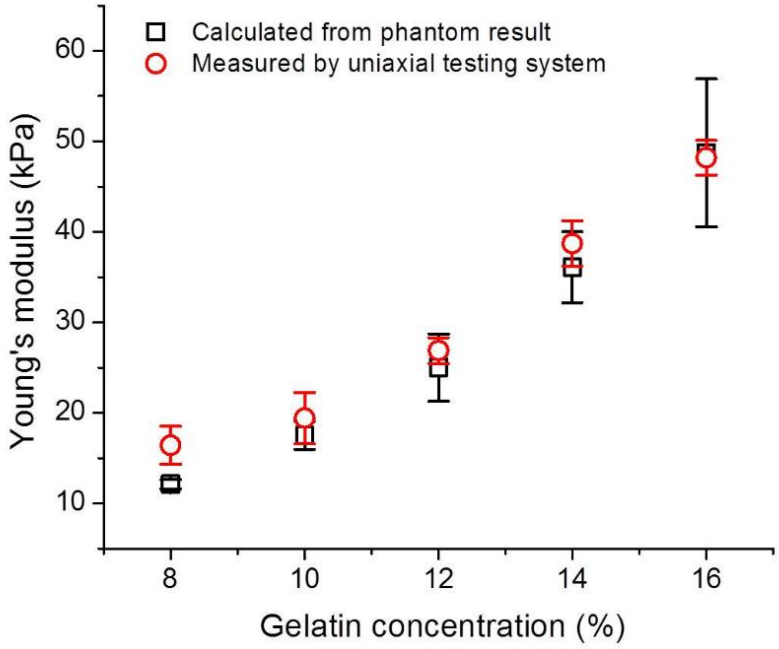

Figure 2.9. Young's moduli of gelatin phantoms calculated from the air-pulse induced elastic wave group velocity and as measured by the uniaxial mechanical testing system.

There are several possible explanations for the observed difference in the delay distribution in phantoms and in the contact lens. One possibility is that the presence of the liquid on the lens posterior surface and the geometry of the lens produce a difference in how the energy propagates within the medium. For instance, the pressure pulse generates P-waves, or compression waves that propagate much faster in the saline solution with low attenuation than the elastic waves in the cornea or lens material. As a result, these waves could produce additional sources of mechanical excitation in the lens after reflection from the hard surface. Therefore, the complex time delay distribution in the contact lens could be explained by the interaction of the different types of the waves. It is clear, however, that the presence of the liquid on the lens posterior surface

complicates the wave pattern similar to what we observed in *in vivo* studies (see Fig. 2.11).

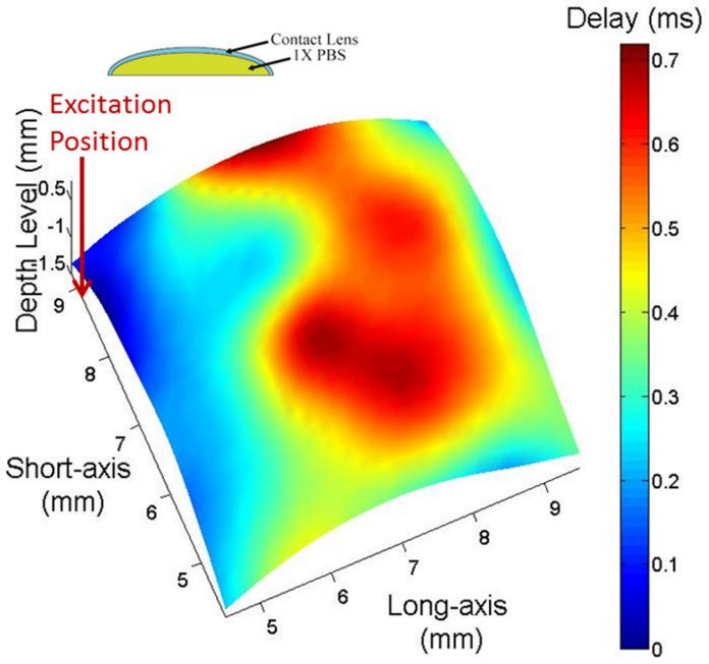

Figure 2.10. 2D rendered graph showing the time delay distribution on the surface of contact lens with 0.9% saline below the lens.

2.2.3 Silicone eye model and in vivo study of 18-month-old mouse cornea

Figures 2.11(a) and 2.11(b) show the OCT structural images and 2D rendered maps for the time delay of the elastic waves measured in the silicone eye model and the mouse cornea *in vivo*, respectively. In Fig. 2.11(a), the time delay of the elastic wave increases as distance increases across the thick and homogeneous silicon layer, which is different from what is observed in the real mouse eye. In Fig. 2.11(b), similar results as Fig. 2.10 can be observed: the time delay of elastic waves increases with the increasing distance before reaching the corneal apex, but decreases with greater distance after crossing the apex.

The distribution of time delay before the elastic waves reach the apex can be used to quantify the wave velocity. For the 18-month-old mouse cornea, the velocity of elastic wave was calculated as 0.92 m/s to 7.42 m/s at different lateral positions due to heterogeneity of the tissue, which are potentially useful for the estimation of cornea elasticity. Additional work is required to develop a quantitative model to estimate corneal elasticity and to obtain corneal elastography, because corneal tissue is inhomogeneous in both structure and composition. Equation 2.3, was developed for isotropic homogenous materials, may not be proper to be used for the tissues like the cornea, which are comprised of multiple layers and have curved surfaces.

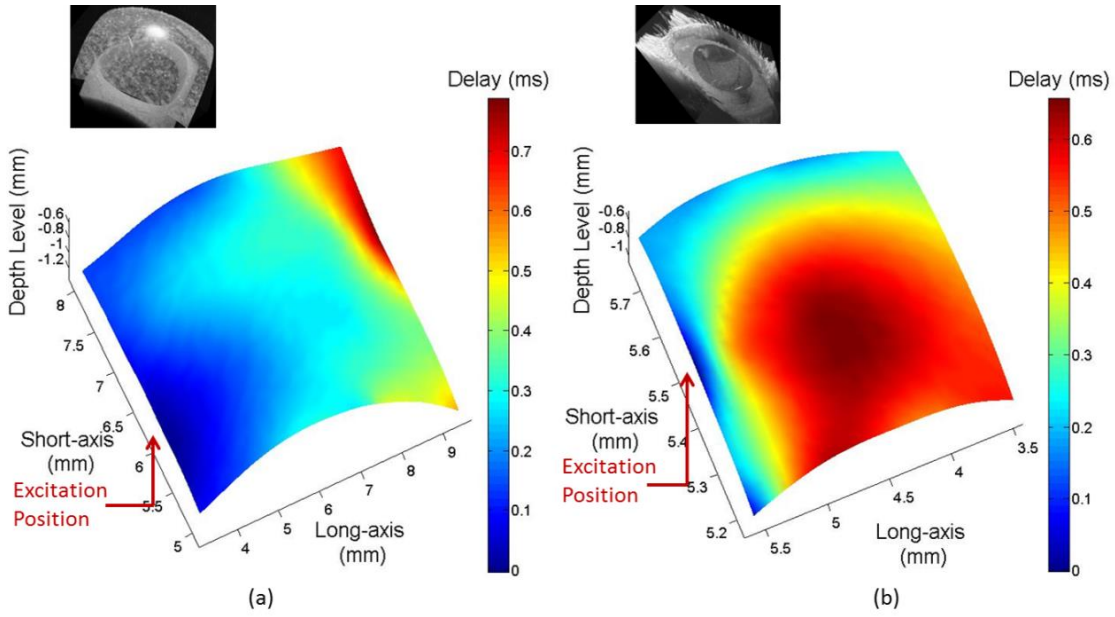

Figure 2.11. The measured time delay of elastic waves on (a) silicone phantom eye model and (b) 18-month-old mouse cornea *in vivo*.

This method does not involve tools that disrupt tissue or physically contact the eye. The displacement caused by air-pulse excitation on cornea in these experiments is on the order of micrometers, which is much smaller than the indentation produced by the air

puff used in clinical measurement of intraocular pressure (tonometry). Therefore, this approach is less invasive than current clinical procedures and suitable for delicate tissues or other sensitive materials. The high sensitivity of the PhS-SSOCT system enables accurate detection of the displacement of the cornea. These advantages allow the dynamic assessment of elastic waves propagating in ocular tissues and make it possible to estimate their biomechanical properties *in vivo*.

However, there were some major limitations of this methods. The distance between two measurement positions was 1mm for non-biological tissue and 0.3 mm for mouse cornea, which governs the spatial resolution of the quantified biomechanical property of samples. Meanwhile, the total data acquisition time for one sample was between 30 mins to 1 hour, depended on the total positions to be measured. The lack of ability to provide the localized elasticity information limited this method from mapping the elasticity of sample with high resolution, and the relatively long data acquisition time limited this method from clinical applications.

2.3 Conclusion

In this chapter, I have demonstrated that PhS-SSOCT can be used to monitor and assess elastic waves that were induced by a focused air-pulse in tissue-mimicking phantoms, contact lenses, a silicone eye model, and the mouse cornea *in vivo*. For the phantoms, Young's modulus can be estimated based on the surface wave velocity. For the ocular models and tissue samples evaluated here, 2D rendered maps of elastic wave propagation time delays were plotted. This was the first study demonstrating the possibility of completely noninvasive excitation and detection of surface waves *in vivo* using optical coherence elastography. With further development, this noncontact optical

method can be used to study the stiffness of delicate tissues such as the cornea and sclera of the eye, and the 2D rendered time delay maps could be translated to an elasticity map.

CHAPTER 3 – Air-pulse optical coherence elastography for assessment of the biomechanical property in mouse cornea of different ages *in vivo*

In this chapter, we demonstrate the use of PhS-SSOCE to assess the relaxation rate of an air-pulse induced deformation in tissue-mimicking gelatin phantoms of various concentrations and mouse corneas of different ages *in vivo*. The air-pulse and the optical beam were co-focused, which enables this method to assess localized biomechanical properties. The results show that the relaxation rate can be quantified and is different for phantoms of varying gelatin concentrations and mouse corneas of different ages. The results indicate that gelatin phantoms with higher concentration as well as older mouse corneas have faster relaxation rates indicating stiffer material. This noncontact measurement technique utilizes low displacement amplitudes (μm scale) and, therefore, can be potentially used to study the localized biomechanical properties of ocular and other sensitive tissues.

3.1 Introduction

There is appreciable, but indirect evidence to suggest that the biomechanical properties of the cornea vary with age. For example, younger corneas have greater risk of both iatrogenic ectasia and keratoconus [123, 124], and the incidence of keratoconus decreases with age [125]. Research has shown that the cornea stiffens over age based on the increase of Young's modulus [126], ocular rigidity coefficient [127, 128], and cohesive tensile strength [129]. However, all these parameters were measured either *ex vivo* or required injection of a balanced salt solution through the limbus into the anterior chamber, which is invasive. Thus, a method that can rapidly assess the biomechanical

properties of cornea noninvasively would provide a more accurate measurement of the age-related changes in corneal stiffness.

In this chapter, the dependence of the relaxation rate of deformation created by a focused air-pulse in tissue-mimicking gelatin phantoms of various concentrations and mouse corneas of different ages *in vivo* using phase-stabilized swept source optical coherence elastography (PhS-SSOCE) was investigated. This parameter was highly depended on tissue elasticity and can potentially be used to quantify biomechanical properties of the cornea and other tissues.

3.2 Materials and Method

In order to simulate soft tissues of controlled stiffness, gelatin phantoms of varying concentrations (8, 12, and 16% w/v) were prepared. Description of the phantom preparation procedure was described in the previous chapter. The geometry of the tissue-mimicking is shown in Fig. 3.1(a).

In vivo experiments were performed on the corneas of healthy mice of different ages (3 - 12 months old). All animal manipulation procedures were approved by the Animal Care and Use Committee of the University of Houston.

A low amplitude (≤ 10 μm) surface deformation was induced by a home-built air-pulse delivery system. The details of this system can be found in our previous publication, as well as chapter 2.1.1 [118]. A channel for signal output from the control unit of the air-pulse delivery system enabled synchronization with the PhS-SSOCT system. The localized air-pulse excitation was precisely positioned with a 2D motorized linear stage (UTS100CC, Newport Corp, USA) in conjunction with a manually controlled vertical stage.

The PhS-SSOCE imaging system was combined with the air-pulse system to detect the surface deformation in the sample. Details of the system have been described in Chapter 2.

During OCE measurements, the air-pulse and the OCT sample beam were co-focused and the distance between the tip of the air-pulse port and the surface was approximately 300. Previous work has shown that the air pressure of the system output remains relatively stable up to 10 mm between the port tip and the sample surface [118]. M-mode imaging at different positions was utilized for OCE measurement. The measurement positions were chosen randomly near the middle region of the phantom and randomly chosen near the apex during *in vivo* experiments. The air pressure on the sample surface was between 1.5 Pa to 2.4 Pa during the gelatin phantom measurements and 2.4 Pa during the *in vivo* experiments to ensure an unwrappable surface deformation and no damage to the sample.

To estimate the relaxation rate of the air-pulse induced deformation, the phase data was first converted to displacement by equation 2.1 [90]. The displacement profiles were then fitted by an exponential function: $y(t) = ae^{-bt}$, where b was the relaxation rate to be determined by fitting. The measurement was repeated for 5 randomly selected positions near the apex of the cornea.

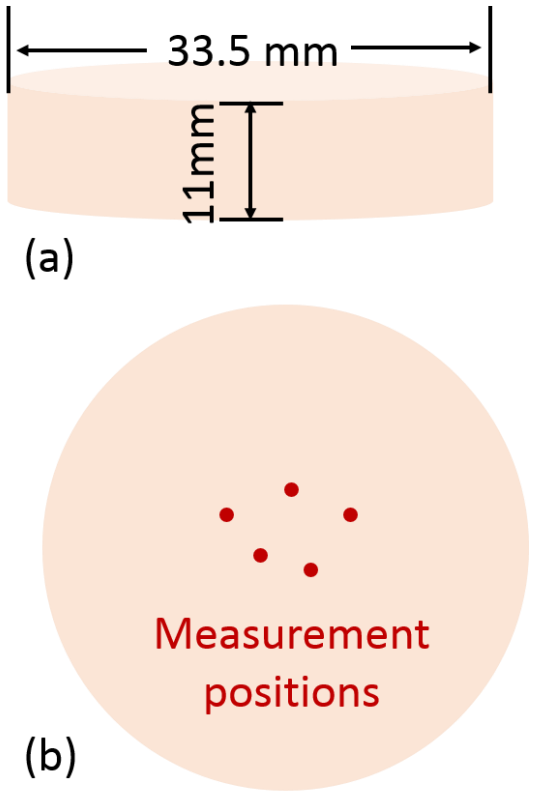

Figure 3.1 (a) Dimensions of the gelatin phantoms. (b) Five measurement positions near the center of phantom were randomly selected.

3.3 Results

Fig. 3.2 shows the displacement amplitude measured in 16% gelatin phantom for various air-pulse excitation pressures. While changing the excitation pressure to 1.5 Pa, 1.95 Pa, and 2.4 Pa, the relaxation rate was measured to be 2.80 s^{-1}, 2.74 s^{-1}, and 2.74 s^{-1}, respectively. This result indicated that the displacement amplitude increased with increasing excitation pressure, but relaxation rate remained relatively unchanged.

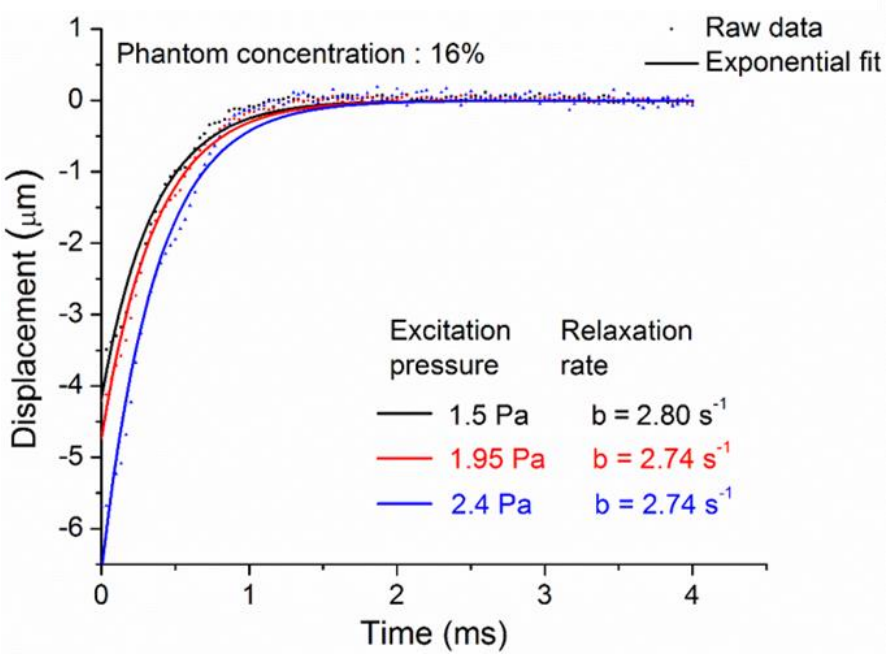

Figure 3.2. Relaxation rate of 16% gelatin phantom with various air-pulse excitation pressures.

Fig. 3.3 shows results from 8%, 12%, and 16% gelatin phantom with 1.5 Pa air-pulse excitation, the relaxation rates were measured to be 1.42 s^{-1}, 2.11 s^{-1}, and 2.80 s^{-1}, respectively. The data show that displacement amplitude decreased and relaxation rate increased with increasing gelatin concentration.

Fig. 3.4 shows the relaxation rate measure from three different concentrations of gelatin phantoms. It clearly indicates that the relaxation rate is faster in higher concentration gelatin phantom, which indicates that the relaxation rate is faster in stiffer material.

In vivo experiments were performed on corneas of mice of five different ages. A representative signal from a 12-month-old mouse cornea *in vivo* is presented in Fig. 3.5.

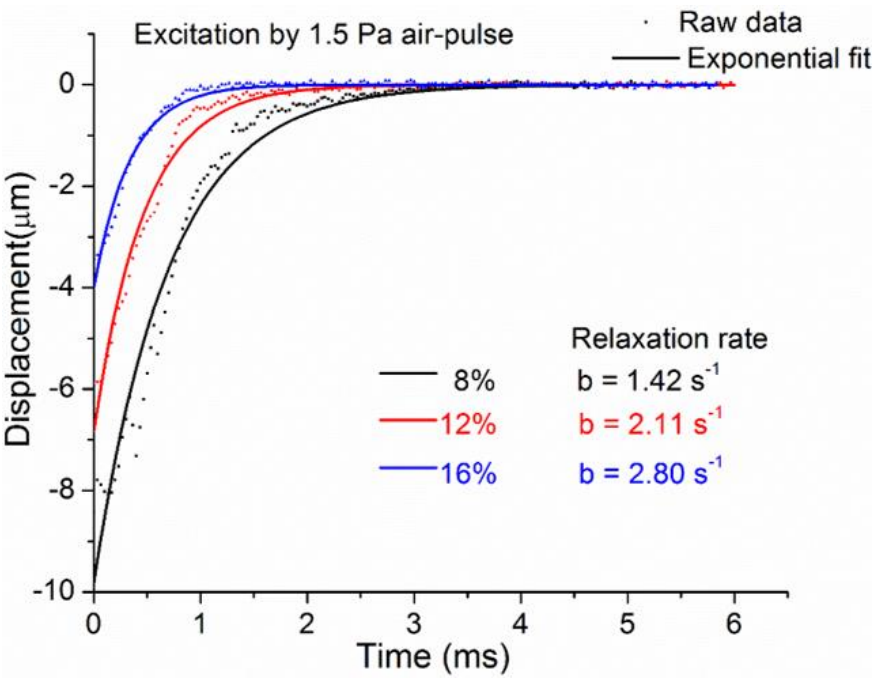

Figure 3.3. Relaxation rate of 8%, 12%, and 16% gelatin phantom with 1.5 Pa air-pulse excitation

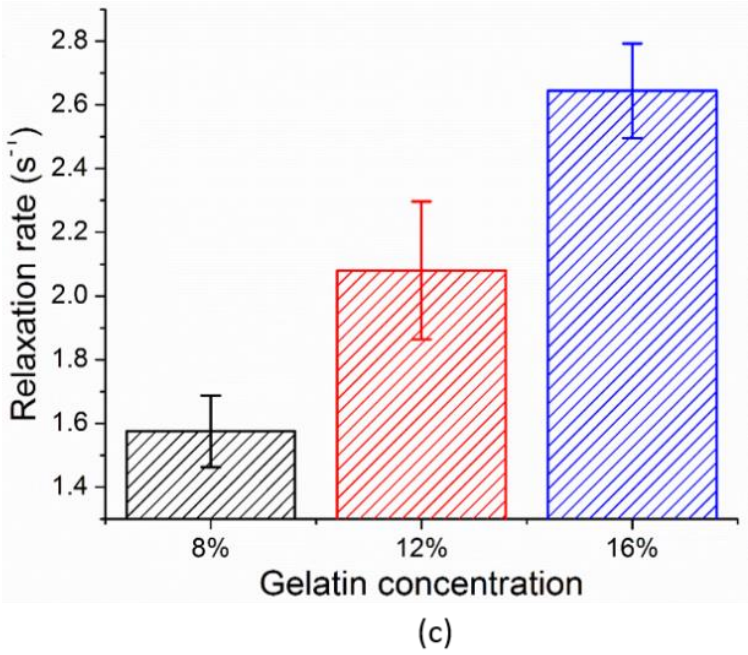

Figure 3.4. Relaxation rate of gelatin phantoms of various concentrations. Three samples were measured for every concentration with five different positions in every sample.

Figure. 3.6 shows the relaxation rate measured on mouse corneas of ages of 3 months, 4 months, 6 months, 8 months, and 12 months, which were $0.81 \pm 0.22\ s^{-1}$, $0.87 \pm 0.18\ s^{-1}$, $1.14 \pm 0.26\ s^{-1}$, $1.21 \pm 0.23\ s^{-1}$, and $1.58 \pm 0.25\ s^{-1}$, respectively. The results clearly show that the relaxation rate was faster in older mouse corneas.

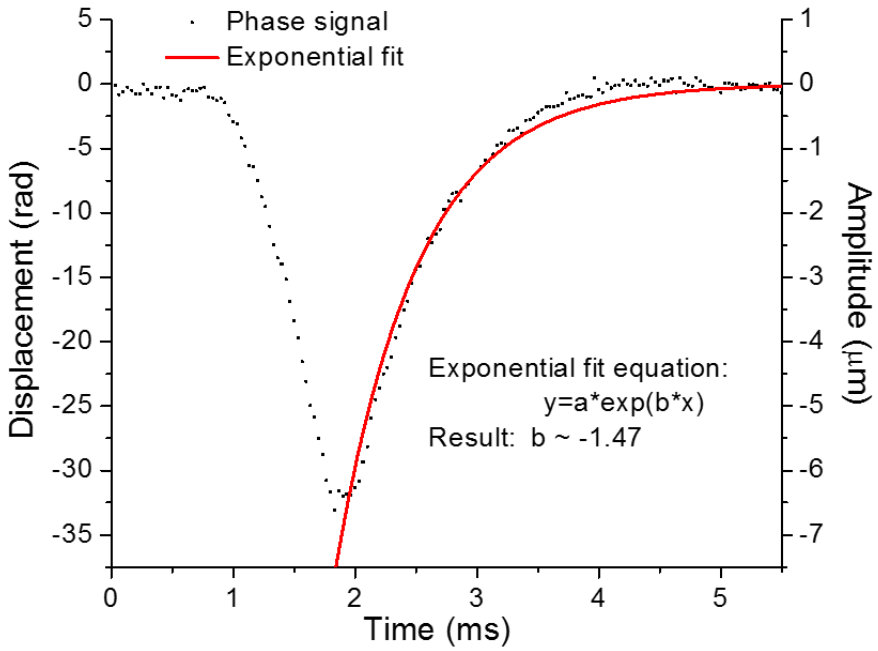

Figure 3.5. Sample signal from 12-month-old mouse *in vivo*.

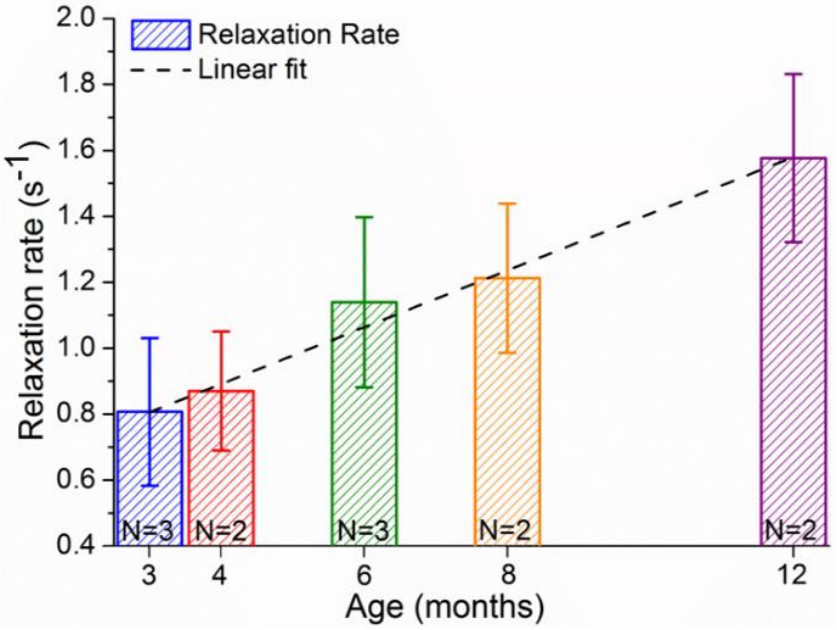

Figure 3.6. Relaxation rates of the mouse corneas of different ages *in vivo*.

3.4 Discussions

During the gelatin phantom experiments, the distance between the air-pulse port and the surface of the phantom and the incident angle relative to the surface normal were easily controlled. Fig. 3.2 clearly shows that the stimulation pressure did not change the relaxation rate in the same sample. Fig. 3.3 indicates the relaxation rates were higher in stiffer gelatin phantoms (higher gelatin concentration).

During the *in vivo* experiments, the distance and the incident angle were not as consistent as in the phantom measurements due to the breathing/heart rate-associated body motion. This may result in increased variation for the relaxation rate measurement. From Fig. 3.6, it can be seen that the relaxation rates of all measurements, regardless of the mouse age, have a higher standard deviation compared with the measurement in

gelatin phantoms, shown in Fig. 3.4. However, these *in vivo* results clearly show that the relaxation rate of the mouse cornea increases with age.

Similar methods have been described by Dorronsoro et al. [130] and Alonso-Caneiro et al. [131]. However, these methods require a significantly larger corneal deformation amplitude because they utilize the OCT structural image, not phase information. This might result in a nonlinear component of the measured corneal biomechanical properties. The method presented here utilized the optical phase information to assess the tissue deformation with superior displacement sensitivity (nanometer level), which greatly reduces the required corneal displacement (micrometer level). In comparison with elastic wave based methods, this approach requires information only from the point of excitation, and hence provides advantages in terms of simplicity, time, and localization.

As we have demonstrated previously, relaxation rate depends on both the elastic and viscous properties of the tissue [132]. The influence of viscosity was not considered here, and additional studies are needed to investigate the influence of viscosity on the relaxation rate. In general, viscosity should decrease relaxation rate and the amplitude of displacement. Because the duration of the air-pulse was shorter than 1 ms, the pulse caused a dynamic response from the tissue, and this response could significantly affect the relaxation rate observed in the experiment. For translating the observed relaxation rate into quantitative mechanical properties of tissue, such as elastic and viscous moduli, a more sophisticated viscoelastic model is required.

3.5 Conclusion

These results demonstrate the use of phase stabilized swept source OCE (PhS-SSOCE) to characterize the relaxation rate of surface displacement in tissue mimicking

phantoms and mouse corneas of various ages *in vivo*. By quantifying the relaxation rate of the displacements, the results show that PhS-SSOCE was capable of distinguishing various concentrations of tissue mimicking gelatin phantoms and ages of mouse corneas. Because both the stimulation and imaging modalities were noncontact, this method is potentially useful for the study of the biomechanical properties of ocular tissues in a clinical setting. Meanwhile, the relaxation rate was measured locally, and this method is potentially capable of mapping the biomechanical properties of a sample. However, converting the relaxation rate to quantitative biomechanical parameters is still a challenge.

CHAPTER 4 – Elasticity localization after partial riboflavin/UV-A corneal collagen cross-linking in the rabbit using optical coherence elastography

UV-induced corneal collagen cross-linking (CXL) is a promising treatment for keratoconus that stiffens the cornea and prevents further degeneration. Optimal CXL treatments would be customized by considering pre-existing corneal biomechanical properties and would consider the effects of CXL, but this requires the capability to noninvasively measure corneal biomechanical properties. In this chapter, we demonstrate that PhS-SSOCE can spatially resolve transverse variations in corneal stiffness. Similar to the previous chapter, low amplitude (≤ 10 μm) deformations in the samples were induced by the focused air-pulse and were detected the by PhS-SSOCT system. As discussed in the previous chapter, converting the relaxation rate into Young's modulus is still a challenge. Thus, the damped natural frequency (DNF) was assessed because it has a linear relationship with the square root of Young's modulus. A 2D grid of measurements was taken and the DNF of the various transverse locations of a heterogeneous phantom revealed the stiffness heterogeneity. After validation on the phantoms, similar OCE measurements were made on partially CXL *in situ* rabbit corneas. The results showed that this technique was able to clearly distinguish the virgin and CXL regions of the cornea, where CXL increased the DNF of the cornea ~168%. Due to the noncontact nature and minimal excitation force, this technique may be potentially useful for assessing corneal biomechanical properties *in vivo*.

4.1 Introduction

Riboflavin/UV-A CXL is an emerging clinical treatment for keratoconus that is intended to increase corneal stiffness and thereby defer further degeneration [133, 134].

The current clinical CXL protocol is uniform despite individual disease presentation or severity since the mechanism by which CXL stiffens corneal tissue is not yet fully understood. However, an optimal treatment would consider pre-existing biomechanical properties and would incorporate the effects of the CXL treatment itself.

The ORA and CorVis are commercially available clinical devices that can measure the differences in the biomechanical properties between healthy and keratoconic corneas [135-137]. However, there is conflicting evidence on whether they can detect stiffness changes in the cornea after CXL [138-141].

While the local mechanical anisotropy and microstructure of the cornea have been studied previously, there have been limited investigations that have quantified the spatial elasticity heterogeneity of the cornea, particularly after CXL [96, 107, 142-148]. All of the previous techniques are either destructive or contact-based, restricting their use for *in vivo* investigations. A noncontact technique that can obtain the local biomechanical properties of the cornea would overcome these limitations and provide a deeper understanding of the dynamics of local corneal biomechanical properties, which in turn could provide a basis for customized therapies, such as CXL [149].

In this work, we have utilized micro air-pulse induced deformations to spatially characterize the biomechanical properties of partially CXL corneas. The low amplitude (micrometer-scale) displacements were detected by a home-built phase-stabilized swept source optical coherence tomography (PhS-SSOCT) system, and the relaxation process of the local deformations was modeled by a simple kinematic model. The DNF, which is well correlated with Young's modulus, was quantified utilizing the kinematic model and was mapped to reveal the localized stiffness of the corneas [150, 151].

4.2 Materials and Method

4.2.1 Experimental materials and system setup

The details of the OCT system can be found in chapter 2 and our previous publication [91]. The experimental setup is shown in Fig. 4.1.

Preliminary experiments were conducted on tissue-mimicking agar phantoms to determine the feasibility of air-pulse OCE to spatially map the biomechanical properties of the cornea. Homogeneous agar phantoms of various concentrations (1% and 2% w/w) were made by standard methods and cast in regular culture dishes with diameter of 50 mm and height of 11 mm. OCE measurements (n=21 for each position) were made every 1 mm over a 2x2 mm region on the homogeneous phantoms as shown in Fig. 4.2(a). To demonstrate the spatial resolving ability of air-pulse OCE, heterogeneous phantoms were constructed as illustrated in Fig. 4.2(b). Here, a 2D grid of OCE measurements (n=21 at each position) was taken every 1.125 mm over a 9x9 mm region. To relate the DNF of the relaxation process in the phantoms to elasticity, uniaxial mechanical compression testing (Model 5943, Instron Corp., MA) was performed on homogenous phantoms of each concentration (n=4 for each concentration). Briefly, the phantoms were compressed at 2 mm/min after a pre-load of 0.04 N was applied. The test was stopped when the strain reached 0.2. The Young's modulus was then calculated from the slope of the measured stress-strain curve at strain=0.1 [122].

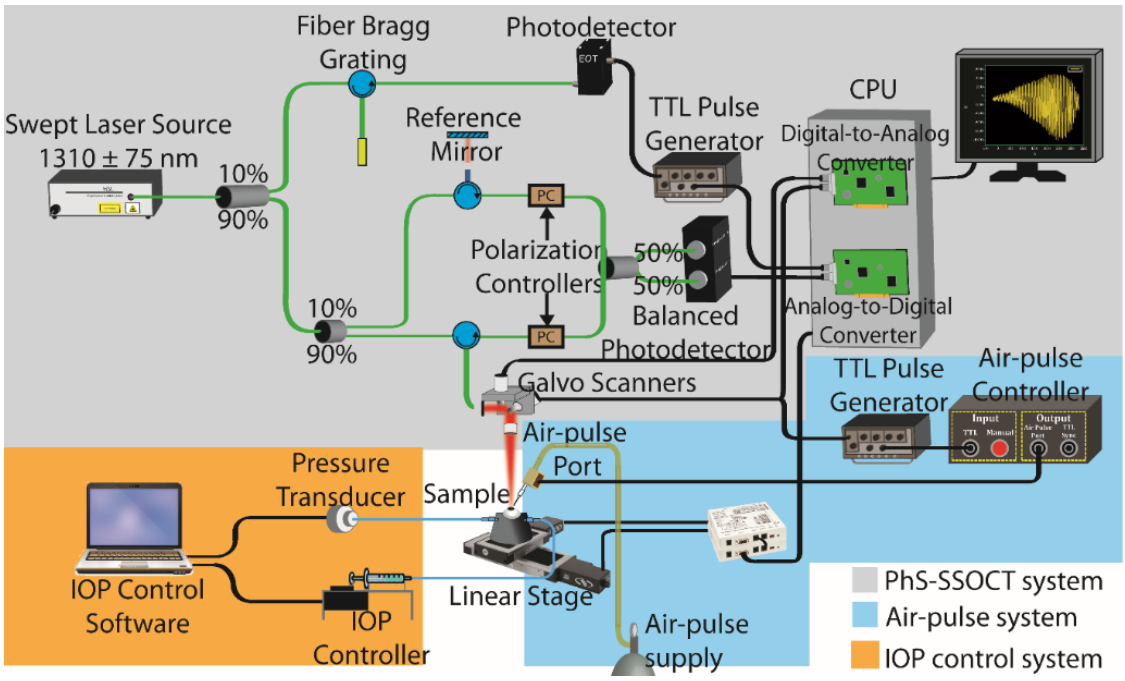

Figure 4.1 Schematic of experimental setup.

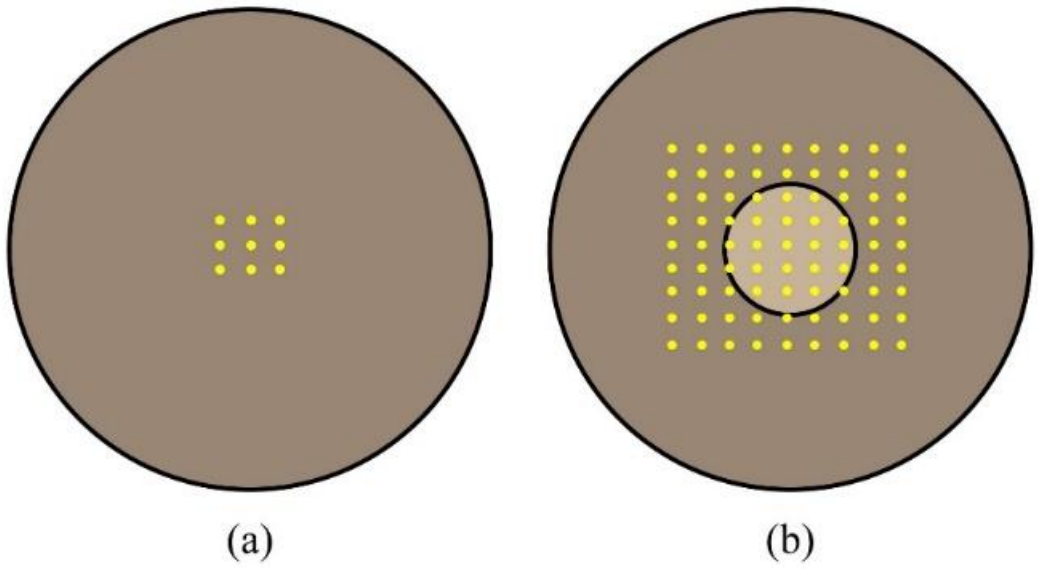

Figure 4.2.OCE measurement methods for the (a) homogeneous phantoms, and (b) heterogeneous phantom. The darker region in (b) was 2% agar (w/w) and the lighter region was 1% agar (w/w). The yellow dots indicated the measurement positions.

CXL was induced on all but a central 2 mm diameter circle of fresh mature rabbit corneas (n=4, Pel-Freez Biologicals, AR) to induce a spatial variation of stiffness as depicted in Fig. 4.3. An additional sample was used for control measurements where OCE measurements were taken before and after traditional CXL. Apart from the foil in the partially CXL samples, the CXL procedure mimicked the standard clinical CXL protocol in both cases [133]. The epithelium was removed with a blunt surgical instrument. A 0.1% riboflavin in 20% Dextran solution was applied every 5 minutes for 30 minutes followed by 30 minutes of UV irradiation (365 nm, 3 mW/cm2, 10 mm spot diameter). During irradiation, the riboflavin solution was instilled every 5 minutes as well. As the IOP can have a profound influence on the measured elasticity of the cornea [152], the IOP was artificially controlled at 15 mmHg using a previously published IOP control system [153].

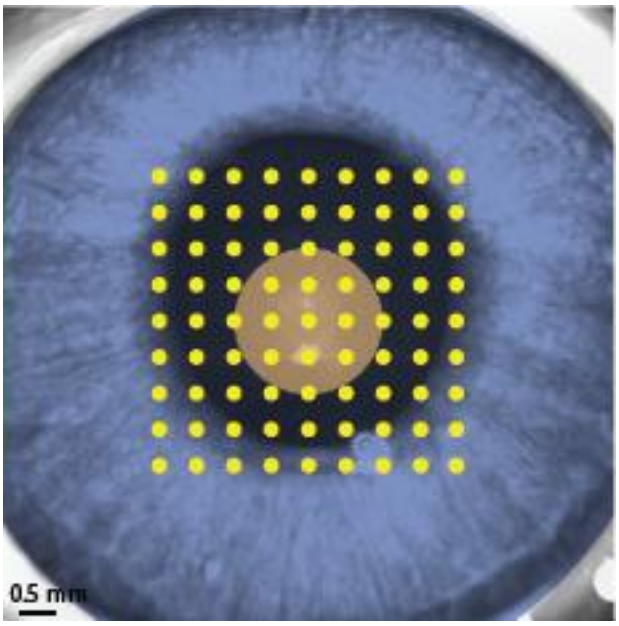

Figure 4.3. OCE measurement methods for the corneas. Central brown circle indicates the masked (untreated) area. Yellow points indicate measurement locations. The remaining area of the cornea was CXL treated.

The micrometer-scale displacements were induced by a home-built micro air-pulse delivery system, which has been described in Chapter 2 [118]. Multiple M-mode images (n=21) were acquired every 0.5 mm (1 mm for the control agar phantom samples) over a 4x4 mm grid centered at the corneal apex. The output air-pulse pressure applied to the cornea surface was ~2 Pa. The raw unwrapped temporal phase profiles from the corneal surface were converted to displacement, $y(t)$, by equation 2.1 [102].

4.2.2 Quantification methods

The relaxation process of the displacement was modeled by the following simple kinematic differential equation [136, 151]

$$m\frac{d^2y(t)}{dt^2} + c\frac{dy(t)}{dt} + ky(t) = 0, \tag{4.1}$$

where m was the equivalent mass, c was the viscosity coefficient, and k was the equivalent spring mass. Two parameters were introduced to simplify the solution and subsequent analysis:$\xi = c/2\sqrt{mk}$ was the damping ratio and $\omega = \sqrt{k/m}$ was the DNF of the system. Substituting these two parameters into (4.2) yields

$$\frac{d^2y(t)}{dt^2} + 2\xi\omega\frac{dy(t)}{dt} + \omega^2y(t) = 0. \tag{4.2}$$

The analytical solution of equation 4.2 depends on the value of ξ:

1. $y(t) = A(1 + bt)e^{-\omega t}$, when $\xi = 1$;
2. $y(t) = e^{-\xi\omega t}[Acos\left(t\omega\sqrt{1-\xi^2}\right) + bsin(t\omega\sqrt{1-\xi^2})]$, when $0 < \xi < 1$;
3. $y(t) = e^{-\xi\omega t}(Ae^{t\omega\sqrt{\xi^2-1}} + Be^{-t\omega\sqrt{\xi^2-1}})$, when $\xi > 1$.

Here, A and B were the parameters to be determined by fitting. From the exponent forms of the solutions to equation 4.2, ω can also be described as the displacement recovery process relaxation rate and was obtained by least-squares variance-weighted (robust)

fitting to the appropriate solution to equation 4.2 with the curve-fitting toolbox in Matlab. The DNF is linearly related to square root of Young's modulus and thus, can be used to characterize stiffness [150, 151].

4.3 Results

4.3.1 Tissue-mimicking agar phantoms

In the agar phantom samples, ξ was found to be less than 1 during fitting. Therefore, the relaxation process was fitted to the second solution of equation 4.2. Fig. 4.4 shows the DNF maps for the (a) homogeneous 1%, (b) homogeneous 2%, and Fig. 4.5 shows the DNF map of the heterogeneous phantom simulating the spatially selective CXL procedure. The mean DNFs for the homogeneous 1% and 2% phantoms were 1.16 ± 0.04 and 2.99 ± 0.07 kHz, respectively, with n=9 OCE measurement positions for both concentrations. In the heterogeneous phantom, the mean DNFs for the 1% and 2% regions were 1.16 ± 0.05 and 3.02 ± 0.06 kHz with n=24 and 57 OCE measurement positions, respectively. To test whether the corresponding concentrations from the phantoms types were similar, a Mann-Whitney test was performed because all the data sub-sets did not pass Shapiro-Wilk tests for normality. The results showed that DNFs of the 1% and 2% concentrations were not significantly different between the homogeneous and heterogeneous phantoms (P=0.73 and 0.3 for the 1% and 2% concentrations, respectively). Fig. 4.6 plots the square root of Young's modulus as obtained by uniaxial mechanical compression testing and the DNFs of the phantoms. The average Young's moduli of the homogeneous 1% and 2% phantoms were 9.8 ± 1.7 kPa and 46.5 ± 2.7 kPa as measured by mechanical testing [122].

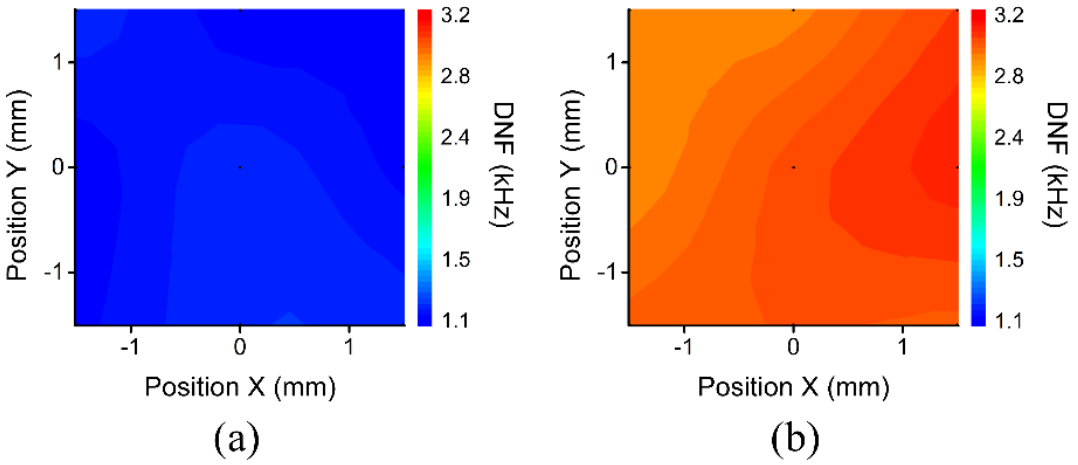

Figure 4.4. DNF maps in the homogeneous agar phantoms where the black dots represent the OCE measurement positions and the DNF scale is the same for direct comparison. DNF maps of the (a) homogeneous 1%, and (b) homogeneous 2%.

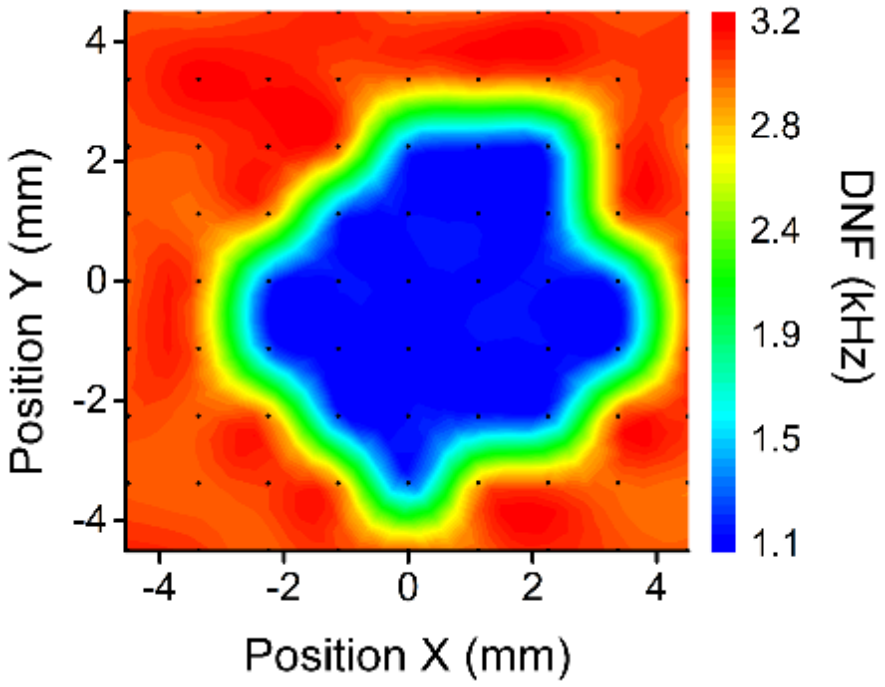

Figure 4.5. DNF map in the heterogeneous agar phantoms where the black dots represent the OCE measurement positions and the DNF scale is the same as figure 4.4 for direct comparison.

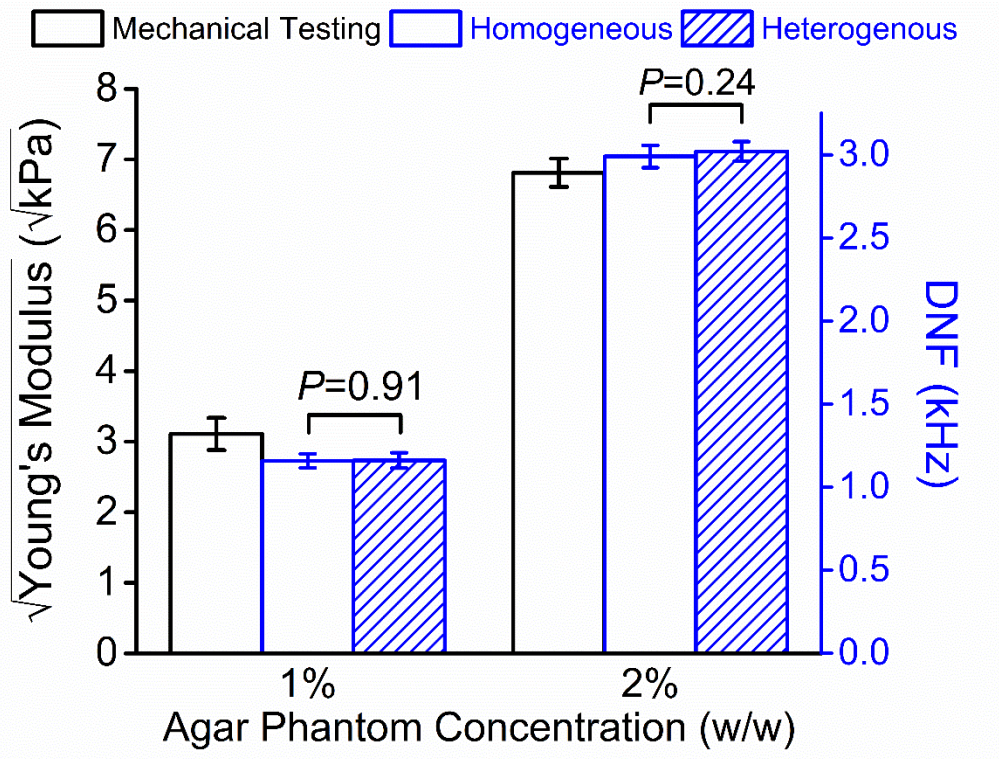

Figure 4.6. A non-paired T test to compare of the square root of Young's modulus as measured by uniaxial mechanical testing to the DNF of the same concentration of homogeneous phantoms, and the corresponding heterogeneous phantom components.

4.3.2 Corneal samples

During fitting for the corneal samples, ξ was found to be very close to 1 ($0.99 \leq \xi \leq 1$). Therefore, ξ was set to 1, and the first solution to equation 4.2 was utilized to obtain the DNF. Fig. 4.7 shows DNF maps for the control cornea (a) before and (b) after traditional CXL, and Fig. 4.8 shows the DNF map of a typical partially CXL cornea. The DNF scales are the same to provide direct comparison. The average DNF of the control sample was 1.22 ±0.01 kHz before CXL, which increased by ~132% to 1.61 ±0.09 kHz after CXL, indicating an increase in stiffness. In the partially CXL sample, the

surrounding CXL region was also stiffer than the central virgin region with average DNFs of 1.93 ±0.11 and 1.12 ±0.05 kHz, respectively.

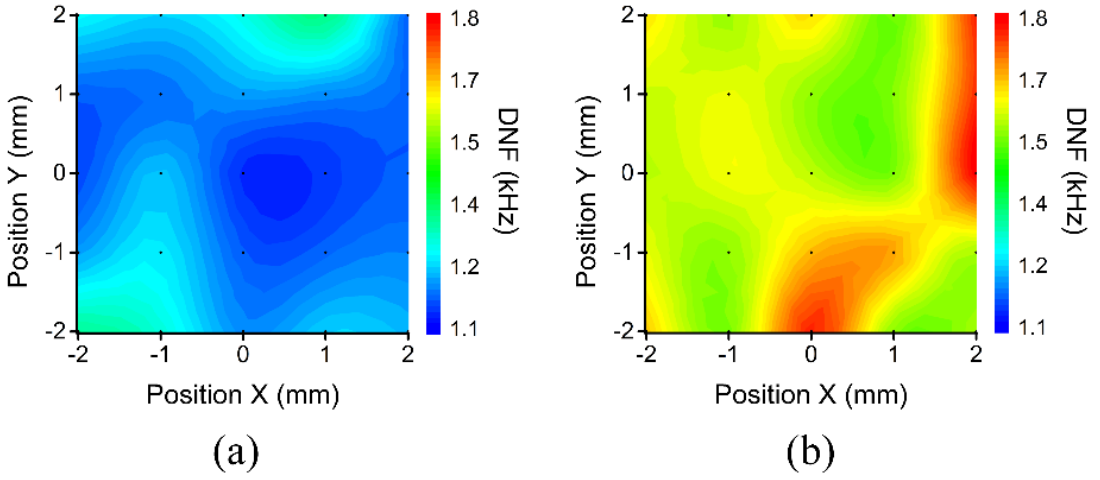

Figure 4.7. DNF maps of the rabbit corneal samples. Maps of the (a) control before CXL, (b) control after CXL. The black dots are OCE measurement positions and the DNF scales are the same for direct comparison.

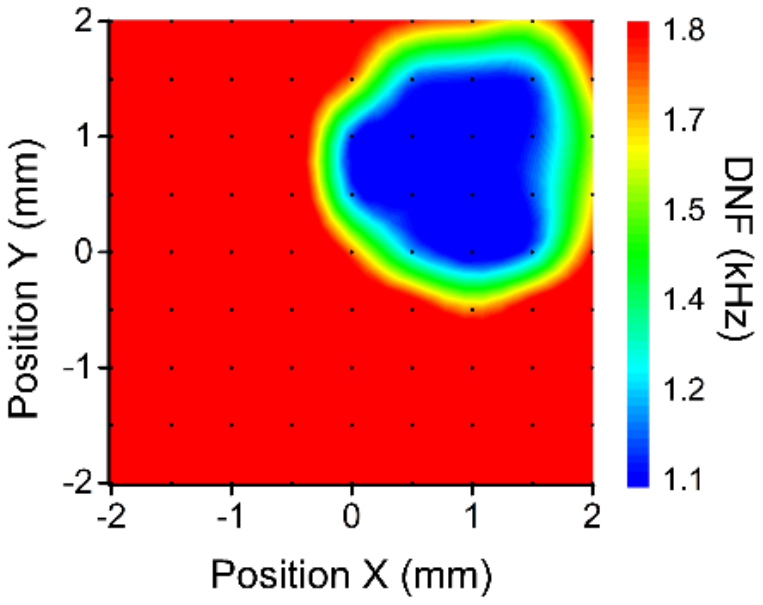

Figure 4.8.DNF map of a typical partially CXL rabbit cornea. The black dots are OCE measurement positions and the DNF scales are the same as Fig. 4.7 for direct comparison.

Fig 4.9 provides an overview of the DNFs of the corneas (control sample, samples 1-4, all partially CXL samples, and all samples). To determine if the change of the DNFs before and after CXL was significant, a paired t test was performed on the control samples, and non-paired t tests were performed between the virgin and CXL region of each partially CXL cornea. The P values of all tests were << 0.05, which indicated that there was very significant difference in elasticity between two regions. The number of samples in each sub-set of data is labeled in Fig. 4.9.

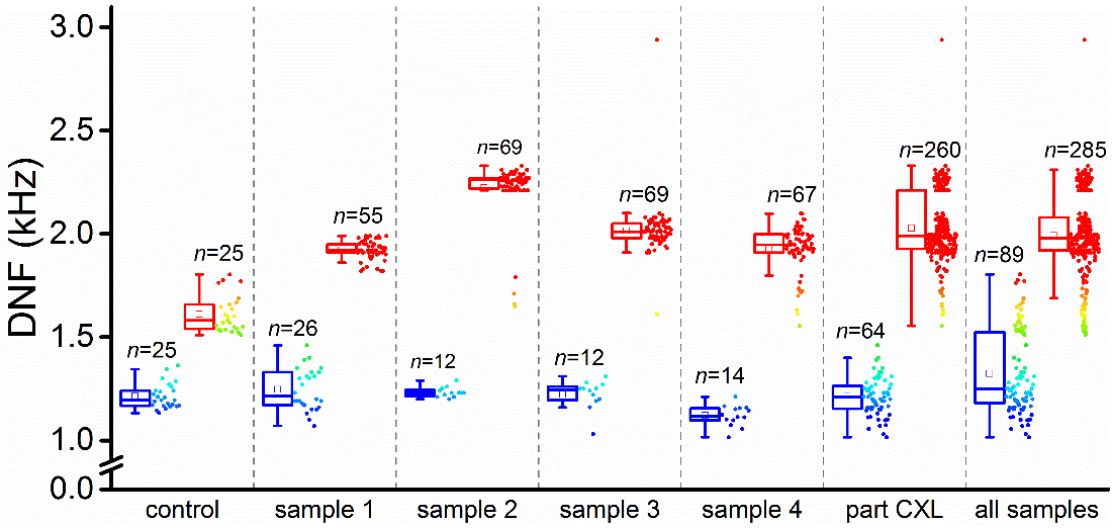

Figure 4.9. DNFs of the corneal samples where the blue and red boxes correspond to the virgin and CXL data sets from the corresponding samples. The central inscribed box is the mean, the central line is the median, and the boundaries are the 25% and 75%.

4.4 Discussion

In this work, we have demonstrated the capability of air-pulse OCE to resolve transverse elasticity differences in spatially heterogeneous tissue-mimicking agar phantoms and partially CXL *in situ* rabbit corneas in the whole eye-globe configuration at an artificially controlled IOP of 15 mmHg. A simple kinematic model was utilized to characterize the air-pulse induced displacement relaxation process and obtain the DNF,

which correlates strongly with the square root of Young's modulus [150, 151]. After demonstrating the feasibility of this method on spatially heterogeneous agar phantoms, this model was then applied to the cornea. The results showed that CXL significantly increased the DNF of all samples ($P \ll 0.05$ for all 5 samples) with an average increase in the DNF of ~160%. While the DNF is related to the Young's modulus in the phantoms, this relationship cannot be directly extrapolated to the cornea in these experiments. The boundary conditions and geometry of the cornea influence the measured elasticity, as we have previously shown utilizing OCE and finite element modeling [154]. In addition, it is well understood that the biomechanical properties of the cornea and the effects of CXL are not homogeneous depth-wise, but the kinematic model used in this work cannot provide the depth-resolved biomechanical properties of the cornea. This will require a more rigorous mechanical model, which we are currently adapting for air-pulse based OCE measurements [41, 115, 155-159].

During the OCE measurements, the sample was manually translated to the various grid positions in a "snake" pattern to reduce the acquisition time as compared to raster scanning. Currently, the total acquisition time of tens of minutes is unfeasible for live measurements. Integration of a 3D computer-controlled motorized linear stage with the OCE acquisition software would enable automated OCE measurements that would dramatically reduce the acquisition time, minimize the risk of errors, and increase the spatial accuracy and repeatability. Such a system has been developed and its feasibility is being tested for live experiments. Our group has recently demonstrated a noncontact OCE technique that can obtain the overall elasticity of the cornea in milliseconds with a single excitation [160]. However, this technique utilized a transversely propagating

elastic wave to quantify the stiffness of the cornea, and thus must be adapted to solely analyze the relaxation process to improve transverse elasticity localization.

While the measurements from the ORA or CorVis can provide the viscoelasticity of the cornea after numerical simulations, their ability to spatially resolve the heterogeneous biomechanical properties of the cornea may be limited due to the relatively large amplitude and large area (mm scale) of the deformation [161]. Other contact-based OCE techniques have been developed and showed promise for obtaining the spatially resolved biomechanical properties of the cornea [96, 107]. However, there has not yet been a report of a quantitative measurement of stiffness with this method. USE has been utilized to evaluate the transverse heterogeneity of CXL, but quantification of the results was focused on the depth-wise heterogeneity of the corneal stiffness after CXL even though there was a clear indication of transverse elasticity heterogeneity [155].

The average ratio of the DNFs between the CXL and virgin regions of the partially-CXL corneas was ~1.68. However, the ratio between the mean DNFs of the positive and negative controls was ~1.32. Even within the partially CXL samples, there was a very significant ($P \ll 0.05$) variation in the DNFs of corneal samples before and after CXL. However, the ratio was still greater in the partially CXL samples than in the control samples. The ocular samples were from mature rabbits (> 6 months) but not of a known age. Mechanical testing has shown that the cornea stiffens with age and therefore, there may be an age dependency of the effects of CXL [162]. Assessing the age-related effects of CXL is an avenue of our future work as we have utilized air-pulse OCE to reveal the age-induced stiffening of the mouse cornea *in vivo* [114]. Moreover, previous CXL investigations have shown a large degree of inter-sample variance in the changes in

biomechanical properties of the cornea after CXL, indicating that changes in the biomechanical properties of the cornea after CXL may be case-specific [163-165]. From Figs. 4.6 (b) and 4.7 it can be seen that the traditional CXL procedure is not spatially homogeneous for a given sample as well and that the stiffness of the virgin cornea is not homogeneous as well. These findings, in addition to the large degree of inter-sample variance, further demonstrate the need for a noninvasive technique capable of accurately and rapidly evaluating the spatial distribution of corneal biomechanical properties and quantitatively evaluating the effects of CXL.

Changes in the corneal stiffness after CXL have shown a wide variance, ranging from ~100% as assessed by Brillouin microscopy to greater than ~300% as quantified by mechanical testing and atomic force microscopy [156, 157, 164]. In addition, the range of the Young's modulus of the rabbit cornea in the literature spans a few orders of magnitude (~1 kPa using AFM to ~11 MPa using mechanical extensiometry) because the measurement technique, testing conditions (e.g. *in situ*, *ex vivo*, or *in vivo*), and IOP all have a profound influence on the measured stiffness [166, 167]. Hence, no mechanical testing was conducted on the corneal samples as with the phantoms because it is still a challenge to properly replicate *in vivo* or *in situ* conditions during mechanical testing. Similarly, our previous work has shown a difference of a few orders of magnitude in the elasticity of the cornea between OCE and mechanical testing [153].

4.5 Conclusion

In this chapter, I have shown that air-pulse OCE is capable of spatially resolving heterogeneous biomechanical properties of the *in situ* rabbit cornea in the whole eye-

globe configuration after spatially selective CXL by analyzing the relaxation process of a micro air-pulse induced displacement. By quantifying the DNF of the low amplitude deformation relaxation process, the transversely spatially varying stiffness of the cornea was revealed. Due to the noncontact nature and minimal excitation force, this technique may be useful for determining the biomechanical properties of the cornea *in vivo*. However, the relatively long acquisition time limits its application in the clinic without further development to drastically reduce the acquisition times.

CHAPTER 5 – Characterizing the biomechanical properties of cornea before and after UV-induced collagen cross-liking at different intraocular pressures by optical coherence elastography

As discussed previously, the method introduced in Chapter 2 is fairly slow (30 min to 1 hour for the measurement of one sample). In this chapter, an alternative is described and used to characterize the biomechanical properties of cornea. In this method, the previously described PhS-SSOCE system and a newly-developed elasticity reconstruction model were used to investigate the effects of UV-induced CXL on the elasticity of porcine corneas at various IOPs. The elasticity of the corneas was assessed before and after CXL using two methods: the group velocity of the elastic wave and temporal analysis of the relaxation process of an air-pulse induced displacement. Validation experiments were performed on agar phantoms of various concentrations, and the results show that both methods were reasonably accurate at assessing the elasticity of the phantoms. The Young's moduli of corneas before CXL treatment were from 7 kPa to 36 kPa as quantified using an elastic wave model and 6 kPa to 25 kPa as obtained from reconstruction of the relaxation process. The CXL treatment significantly increased the Young's moduli of the corneas from 40 kPa to 70 kPa and 20 kPa to 110 kPa as quantified using the elastic wave velocity and relaxation process methods, respectively.

5.1 Materials and Method

Seven cylindrical agar phantoms (Difco Nutrient Agar, Becton, Dickinson and Company, MD, USA) with diameter of 30 mm and height of 10 mm and various concentrations were prepared for validation of the elasticity reconstruction method. Fresh porcine eyes of similar age (n=4) were obtained from Sioux-Preme Packing Co. (Sioux

City, IA, USA) and shipped overnight in a chilled container. Upon arrival, the eyes were brought to room temperature and the corneal epithelium was removed with a blunt surgical instrument. The whole eye globes were placed in a custom eye globe holder and cannulated with two needles for artificial IOP control utilizing a previously published system [153]. After the OCE experiments were completed on the untreated corneas, traditional CXL was performed as described in Chapter 4 [133]. The OCE measurements were performed at IOPs of 15, 20, 25, and 30 mmHg, as controlled by the closed-loop artificial IOP control.

A home-built focused air-pulse delivery system induced a small amplitude (μm scale) displacement, which then propagated as an elastic wave through the cornea as described in Chapter 2 [118]. The elastic wave was imaged by the previously described PhS-SSOCT system.

To remove the manual translation, need for synchronization during post-processing, to improve the transverse spatial resolution, and reduce the total acquisition, a new automated method of imaging the air-pulse induced elastic wave propagation was developed. A longitudinal scan of 501 successive M-mode images was acquired over ~6 mm with the apex of the cornea at the middle of the acquisition area to capture the elastic wave propagation. The trigger signal of each M-mode image was used for synchronization with the air-pulse controller, resulting in each M-mode image effectively recording the elastic wave [116, 168]. The distance between the air-pulse port and the surface of the cornea was kept at ~200 μm with an incidence angle of ~30º. Although the OCT system can only detect displacements in the vertical direction, the angle of incidence has no significant effect on the measured speed as the elastic wave propagated

primarily orthogonal to the optical axis. The pressure of the applied focused air-pulse on the corneal surface was fixed at ~4 Pa for both untreated and CXL corneas to ensure a detectable induced elastic wave without damaging the delicate corneal tissue. While measuring the temporal characteristic of the elastic waves, the air-pulse and the OCT probing beam were co-focused at the apex of the cornea as described in previous chapters. For these measurements, the applied pressure of the air-pulse was ~2 Pa on the untreated corneas, and ~4 Pa on the CXL corneas. M-mode imaging at the apex of the cornea was utilized to image the deformation and relaxation processes of the air-pulsed induced local deformation.

The Young's modulus, *E*, was quantified by the shear wave equation, which has been used to quantify the stiffness of samples in various applications [5, 55, 104]

$$E = 3\rho {c_g}^2, \tag{5.1}$$

here, ρ was the density of the cornea and c_g was the group velocity of the OCE measured elastic wave. We should note here that c_g should be the shear wave velocity, which was not identical to the OCE measured elastic wave group velocity even though it has been used to quantify Young's modulus with the shear wave equation [5, 104].

After correcting the phase data for surface motion and the refractive index mismatch between air and the sample [169], the temporal profile of the air-pulse induced displacement, $d(t)$, was calculated from the corrected phase profiles, $\phi(t)$ by equation 2.1 [102]. The relaxation process of the temporal displacement profile was fitted by the exponential function in Section 3.2. The b value for a given displacement profile was discarded if R^2 was less than 0.98 due to phase unwrapping errors or other artifacts, which resulted in improper fitting of the relaxation process.

A model-based elasticity reconstruction approach was developed to quantify the Young's modulus from the vertical displacement profile of a surface point of the cornea in response to the short duration air-pulse [159]. In this method, the tissue was modeled as a homogenous and nearly incompressible viscoelastic (Kelvin-Voigt body) layered structure. The mechanical parameters such as Young's modulus (E), shear viscosity modulus (η), and density (ρ) were set to be constant in a layer. Under external loading applied in the vertical direction on the surface, such as an air-pulse, an analytical solution of the vertical displacement at angular frequency ω in the frequency domain can be derived in cylindrical coordinates (r, θ, z) as

$$U_z(r,z) = \int_0^{+\infty} \left[\alpha(A_1 e^{-\alpha z} + A_2 e^{\alpha z}) + k\left(B_1 e^{-\beta z} + B_2 e^{\beta z}\right)\right] J_0(kr) k dk, \quad (5.2)$$

with

$$\alpha^2 = k^2 - \frac{\omega^2}{c_1^2},\ \beta^2 = k^2 - \frac{\omega^2}{c_2^2},\ c_1 = \sqrt{\frac{\lambda+2\mu}{\rho}},\ c_2 = \sqrt{\frac{\mu}{\rho}},$$

here, J_0 and J_1 are the 0 and 1 order Bessel functions, respectively, k is the wave number, and λ and μ were the Lam é constants, with $\lambda = Ev/((1+v)(1-2v))$ and $\mu = E/(2(1+v))$. The dynamic modulus, E, included the Young's modulus and the shear viscosity components, and v is the Possion ratio. The unknown constants A_1, A_2, B_1, and B_2 were defined using four boundary conditions at the layer boundaries. The boundary conditions utilized in our calculations were: a fixed boundary condition for the displacements on the bottom of the layer; no shear force on the top surface, and an external load with ~30 ^{o}incidence angle was applied at the top surface at the co-focal point of the stimulation and measurement position. Using the analytical solution for the vertical displacement

described by equation 5.3, reconstruction of Young's modulus and shear viscosity were obtained with a gradient-based iterative approach by minimizing the error function

$$\varepsilon = \|U^{exp} - U^{theory}(E, \eta)\|, \tag{5.3}$$

where ε was defined as the difference between the measured, U^{exp}, and theoretically calculated, U^{theory}, displacements at the excitation point [170].

The reconstruction model was first evaluated on agar phantoms (Difco Nutrient Agar, Becton Dickinson, MD, USA) of various concentrations and subsequent stiffness. Uniaxial mechanical compression testing (Instron 5943, MA, USA) was performed on the same agar phantoms immediately after all OCE measurements. During calculation, the densities of agar phantom and rabbit cornea were set as 1000 kg/m^3 and 1062 kg/m^3, respectively [171, 172]. To minimize the error function (Eq. 5.4), a gradient-based iterative procedure was implemented. In order to remove influence of the potential variability of the excitation pressure on the surface of the samples, the vertical temporal displacement profiles were normalized. Thus, only the spectral characteristics of the displacement were taken into account, ignoring the amplitude of the displacement.

5.2 Results

Table 5.1 shows the Young's moduli of all 7 agar phantoms estimated by the reconstruction model and equation 5.1 using the OCE experimental data and as measured by the uniaxial mechanical compression test. The concentrations were random and unknown so that any bias would be minimized. The error was defined as the absolute value of the difference between the estimated Young's modulus and the measured Young's modulus divided by the measured Young's modulus. The range of the error was

0.3% to 12%, with an average error of 6.9%, which indicated that the accuracy of the reconstruction model was acceptable.

Table 5.1. Young's moduli obtained by the elasticity reconstruction model utilizing the temporal vertical displacement profiles (estimated) and from uniaxial mechanical compression testing (measured).

Phantom #	Young's Modulus (kPa)		Error (%)
	Estimated	Measured	
1	12.5	12.6	0.8
2	15	13.9	7.9
3	37.5	42.6	12
4	40	36.1	10.8
5	37.5	35.4	5.9
6	60	59.8	0.3
7	62.5	69.8	10.5

In addition to elastographic measurements, the central cornea thickness (CCT) was calculated from the OCT structural image to quantify a morphological parameter of the corneas before and after CXL as a function of IOP. To ensure proper measurement, the OCT images were rescaled to physical dimensions with the refractive index of the cornea as 1.376 [173]. Fig. 5.1(a) shows that the thicknesses of untreated (UT) and CXL corneas decreased as the IOP increased. In Fig. 5.1(b), the thicknesses were normalized by the maximum for the UT and CXL sub-groups. Here it can be seen that the change in thickness as a function of IOP is greater in the UT corneas as compared to the CXL corneas, as expected for a softer material.

Fig. 5.2 displays three typical temporal displacement profiles of the elastic wave at different OCE measurement positions from a porcine cornea at various distances from the stimulation position. The time delay of the elastic wave to propagate to each OCE measurement position was obtained by cross-correlating the normalized temporal displacement profiles at each OCE measurement position with the normalized temporal displacement profile at the excitation position. This procedure was repeated for each imaged in-depth layer of the cornea. The elastic wave velocity was calculated by least squares linear fitting of the elastic wave propagation delays at each OCE measurement position and the distances of the respective positions from the excitation. This procedure was repeated for each imaged depth of the cornea, and the average of all depths was utilized as the elastic wave group velocity for a given sample. As the elastic wave was assumed to follow the contour of the cornea, the curvature was taken into account when determining the elastic wave propagation distance to ensure accuracy of the velocity calculation.

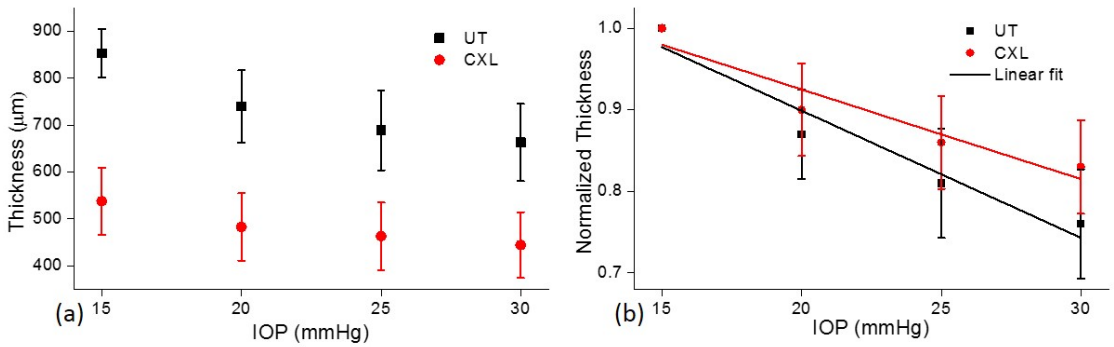

Figure 5.1. (a) Averaged CCT of UT and CXL corneas (n=4) at different IOPs. (b) Normalized central corneal thickness and linear fit of UT and CXL corneas at different IOPs.

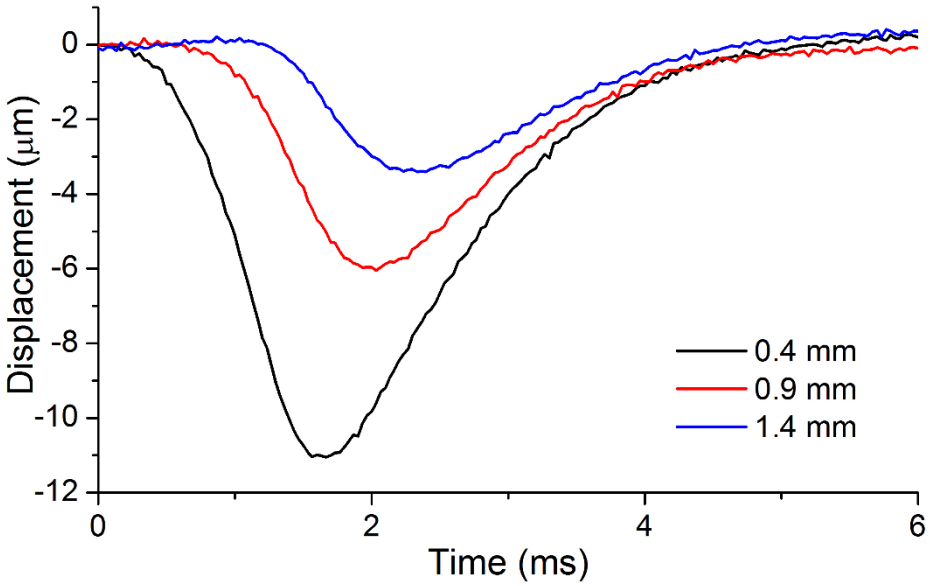

Figure 5.2. Three typical temporal displacement profiles on the cornea from OCE measurement positions at the indicated distances from the air-pulse excitation point. The elastic wave propagation and amplitude attenuation can be seen from the profiles.

Fig. 5.3(a) shows that the elastic wave group velocities were greater after the CXL treatment at the same IOP. It can also be seen that the elastic wave group velocity was positively correlated with IOP in the UT and CXL corneas. The Young's moduli of corneas estimated using equation 5.1 are shown in Fig. 5.3(b). The standard deviation (STD) of some data sets were too small to be shown clearly, such as the group velocity of the CXL eyes at 20 mmHg IOP (n=4, STD = 0.014). It can clearly be seen that the corneas were significantly stiffer after the CXL treatment, which corroborates with previous work [65, 133, 153, 157, 164, 174, 175]. Furthermore, the Young's moduli of all of the corneas increased with IOP, which has also been shown in the literature [174].

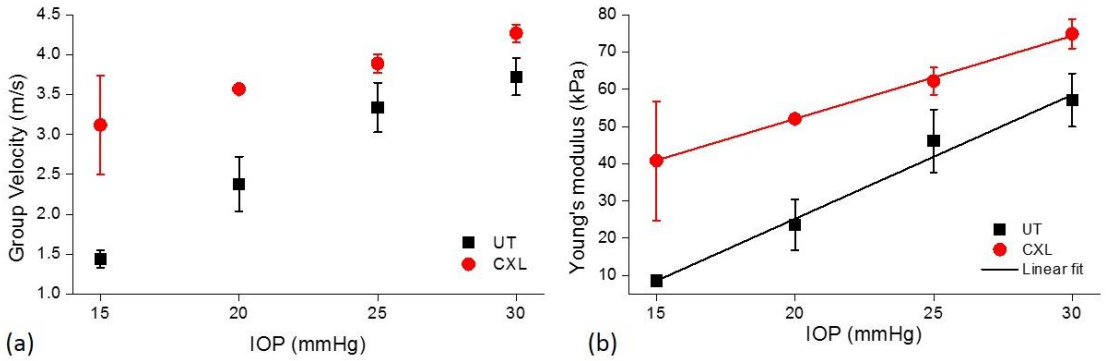

Figure 5.3. (a) Elastic wave group velocity of untreated and cross-linked porcine corneas (n=4) as a function of IOP. (b) Young's moduli of corneas estimated by the shear wave equation 5.1 using the OCE measured elastic wave group velocity.

Fig. 5.4 displays typical relaxation process vertical temporal displacement profiles of a focused air-pulse induced displacement at the corneal apex from the same sample before and after CXL treatment at an IOP of 25 mmHg. The relaxation process was found to be well fitted the previously described exponential equation in Section 3.2 as R^2 was greater than 0.99. The relaxation rate was higher in the cornea after the CXL, which corresponded to a stiffer material.

Figure 5.5(a) shows that the relaxation rates in CXL corneas were greater than in UT corneas at the same IOP. Figure 5.5(b) displays the Young's moduli of the UT and CXL corneas as a function of IOP estimated by the vertical displacement elasticity reconstruction model as described in equations 5.2 and 5.3.

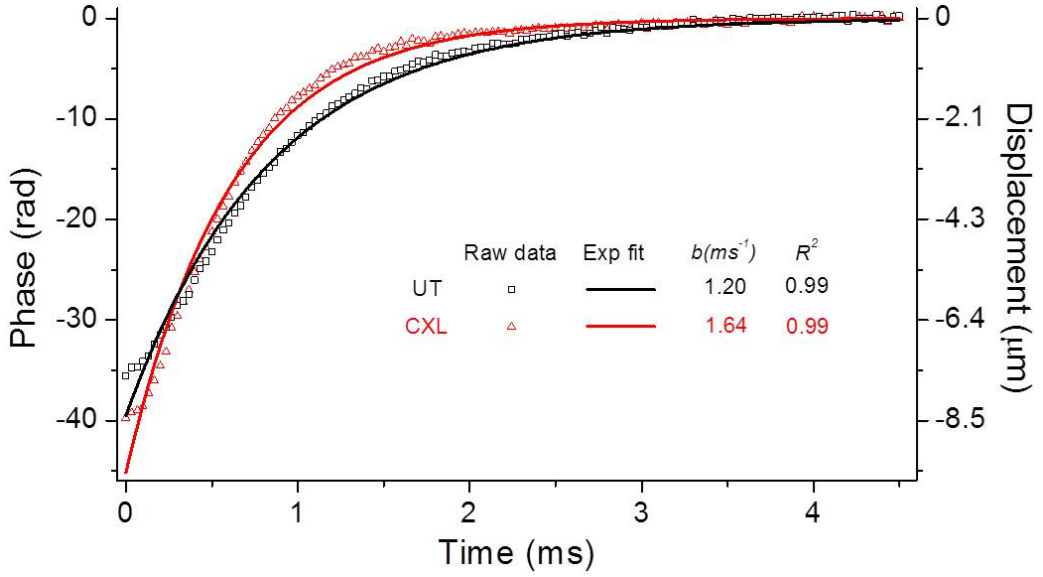

Figure 5.4. Typical relaxation process vertical temporal displacement profiles from a focused air-pulse induced deformation at the corneal apex from the same cornea before and after CXL treatment at an IOP of 25 mmHg.

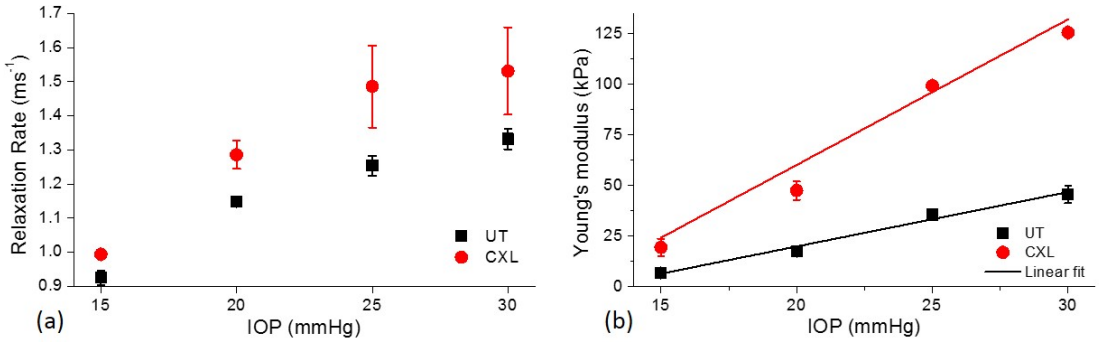

Figure 5.5. (a) Relaxation rate of the UT and CXL corneas (n=4) as a function of IOP. (b) Young's moduli of the corneas obtained by the vertical displacement elasticity reconstruction method.

5.3 Discussion

Structural imaging of the cornea with OCT demonstrated that the CCT of the corneas decreased after CXL, which was consistent with the literature [176-178]. On average, the corneas became ~34% thinner after CXL. Specifically, the corneal thicknesses decreased by 37±1%, 35±2%, 33±1%, and 33±2% after CXL at the IOPs of 15, 20, 25, and 30

mmHg, respectively. The negative correlation of corneal thickness with IOP from 15 to 30 mmHg has also been shown previously in normal canine eyes [45]. Intuitively, it is reasonable to expect that the increased IOP will compress the cornea and reduce the thickness. After normalizing the thicknesses of the UT and CXL eyes at each IOP by the initial thicknesses at an IOP of 15 mmHg, the slopes of the linear fit were -0.016 $mmHg^{-1}$ and -0.011 $mmHg^{-1}$ before and after CXL, respectively. This indicated that after CXL, the rate at which the CCT decreased was less as compared to before CXL. This can be explained by the "J" shape of the cornea stress-strain curve [164]. With a greater Young's modulus after CXL, additional stress induced a smaller strain, which corresponded to a smaller change in thickness.

The Young's moduli of the corneas estimated by the shear wave equation 5.1 and surface displacement reconstruction model increased linearly as a function of IOP in both UT and CXL corneas as shown in Fig. 5.3(b) and 5.5(b), respectively. The observed linear increase in Young's modulus is similar to previous results where the elasticity of porcine corneas obtained by inflation test increased linearly as function of IOP from 5 to 75 mmHg [179].

The viscosity values for the UT and CXL corneas from the vertical displacement reconstruction model were not compared in the results. Our preliminary study shows a random distribution of viscosity in the range of 0 to 0.25 Pa•s, with no obvious correlation between the UT and CXL corneas. One of the potential sources of the random distribution of viscosities may be due to the linear Kelvin-Voigt viscoelastic model that was not adequate to describe the true complex viscoelasticity of corneal tissue. Future investigations will focus on determining the effects of the CXL treatment on the viscosity

of the cornea. Since the value of viscosity was extremely small compared with the elasticity, it would have limited effect on the reconstructed profile in the reconstruction model. Future work will involve investigating the accuracy of the viscosity reconstruction and optimizing the model for effects of very small viscosities.

Previous chapters have shown that a higher relaxation rate corresponds to stiffer tissues [114]. However, the Young's modulus was not quantified. In this chapter a model was implemented to translate the relaxation process vertical displacement profile to a quantitative assessment of elasticity in the cornea. It also can be noted that the Young's moduli estimated from the two different elasticity reconstruction methods adopted in this work were different. This may be due the restrictions and assumptions of each method. The shear wave equation 5.1 relies on the assumption that the OCE measured elastic wave is identical to a shear wave. However, it has been reported that the observed elastic wave in cornea is not identical to a shear wave [180, 181]. Furthermore, the elastic wave propagation dynamics were determined by the corneal material properties, shape, excitation method, and boundary conditions. Nevertheless, the shear wave equation has been used to estimate the material elasticity because of its simplicity and subsequent rapid estimation of Young's modulus [180]. Nevertheless, the group velocity of the observed elastic wave is of the same order as the shear wave velocity and thus, the shear wave equation may be able to provide a rapid first-order quantitative assessment of elasticity. In this study, the velocity of the elastic wave was calculated over a few millimeters, varying from ~2 mm to ~6 mm depending on the sample. Therefore, the elasticity assessed by the shear wave equation 5.1 may be the overall elasticity of this region. In addition, the corneal biomechanical properties have been widely reported to

be anisotropic, so the direction of excitation and elastic wave propagation imaging may also affect the quantified Young's modulus [143, 182-184]. Although the velocity of the elastic wave was calculated as a function of depth as well, the large wavelength (~5 mm) of the elastic wave limits depth resolution. Other methods such as spectral and dispersion analysis can provide depth resolved elasticity with micrometer scale spatial resolution [115, 185] and will be implemented in future studies.

The vertical displacement elasticity reconstruction model assumed an infinite flat thin plate sample geometry [170, 186]. The model was strictly derived from the Navier-Cauchy equation, which is the governing equation for an isotropic material with a small displacement assumption. The small displacement assumption was satisfied as the air-pulse induced displacement was a few orders of magnitude less than the thickness of the cornea. However, the cornea has a curvature, which did not strictly satisfy the infinite flat plate geometry restriction, which may be a source of inaccuracy when reconstructing elasticity via this method. Nevertheless, the model was able to successfully demonstrate the changes in the elasticity of corneas before and after CXL as a function of IOP. Furthermore, due to the small focal spot size of the air-pulse and high spatial resolution of OCT, this method has the potential to create a 2D elasticity map of the cornea with high spatial resolution in contrast to the DNF described in the previous chapter.

5.4 Conclusion

In this chapter, an OCE technique which significantly reduces the data acquisition time for cornea elasticity quantification was introduced. Compared to the method introduced in Chapter 2, the data acquisition time was reduced from ~30 mins to less than 1 min. The elasticity of porcine corneas was quantified before and after UV-induced

CXL at various IOPs by combining noncontact OCE with two different elasticity reconstruction methods. A focused air-pulse was used to induce a localized deformation in the corneas, which then propagated as an elastic wave. The group velocity of the elastic wave and relaxation process of an air-pulse induced displacement at the corneal apex were quantified and utilized for elasticity reconstruction. As expected, the stiffness of the corneas increased after CXL and as the IOP was increased. This noncontact OCE method was capable of measuring low amplitude (μm scale) tissue deformations and assessing corneal stiffness, which is potentially useful for studying the biomechanical properties of sensitive ocular tissues *in vivo*.

CHAPTER 6 – Differentiating untreated and cross-linked porcine corneas of the same measured stiffness with optical coherence elastography

Structurally degenerative diseases such as keratoconus can significantly alter the stiffness of the cornea, directly affecting the quality of vision. UV-induced CXL effectively increases corneal stiffness and is utilized clinically to treat keratoconus. However, the measured corneal stiffness is also influenced by IOP. Therefore, experimentally measured changes in corneal stiffness may be attributable to the effects of CXL, changes in IOP, or both. In this work I present a noninvasive measurement method using PhS-SSOCE to distinguish between CXL and IOP effects on corneal stiffness. This method compared the displacement amplitude attenuation of a focused air-pulse induced elastic wave. The damping speed of the displacement amplitudes along the wave propagation path was compared for different materials with the same measured elasticity. This method was initially tested on gelatin and agar phantoms of the same stiffness for validation. After validation on the phantoms, UT and CXL treated porcine corneas of the same measured stiffness, but at different IOPs, were also evaluated by this technique. The results suggested that this noninvasive method may have the potential to detect the early stages of ocular diseases such as keratoconus or evaluating the effects of CXL by factoring in the effects of IOP on the measured corneal stiffness.

6.1 Introduction

As discussed previously, keratoconus can pathologically decrease the stiffness of the cornea, leading to a loss in the quality of vision [113]. UV-induced CXL is an emerging treatment for keratoconus, which increases corneal stiffness [133]. In addition to structural changes within the corneal tissue caused by CXL, IOP also has an effect on

the measured stiffness of the cornea [187]. Therefore, there is a possibility that a cornea may be structurally weakened by keratoconus, yet have a "normal" measured stiffness due to an elevated IOP. Current techniques are not able to measure the true IOP *in vivo* without consideration of the effect of measured corneal stiffness [188]. Distinguishing corneas that have the same measured stiffness but are at different IOPs is still a challenge.

In this chapter, I present a method that is capable of distinguishing corneas of the same measured stiffness but at different IOPs utilizing noncontact OCE where a focused air-pulse induced elastic waves in the sample and a PhS-SSOCT system detected the wave propagation. Validation experiments were performed on agar and gelatin phantoms of the same stiffness. This method was then applied to UT and CXL porcine corneas. Artificial IOP control was used to induce the same measured corneal stiffness in the UT and CXL corneas.

6.2 Materials and Method

A home-built PhS-SSOCE system consisted of a focused air-pulse delivery system and a phase-stabilized swept-source OCT (PhS-SSOCT) system. Details of the system can be found in Chapter 2, and a schematic of the experimental was shown in Chapter 4. The elastic wave imaging experimental setup and data acquisition procedures are the same as described in Chapter 5. The artificial IOP control system was detailed in our previous publication [153].

A validation study was initially conducted on 14.0% gelatin (w/w) and 1.1% agar (w/w) phantom samples (n = 5 for each type) with identical cylindrical dimensions of diameter D = 33 mm and height H = 11 mm. The group velocity of induced elastic wave as measured by OCE was converted to Young's modulus using equation 2.1. In this work,

the density of both gelatin and agar phantoms was chosen to be 1020 kg/m^3, and the Possion ratio was set to be 0.49 [100, 120].

The excitation amplitude was controlled to ensure accurate phase unwrapping. To compare the damping characteristics between any two normalized displacement amplitude attenuation curves of the elastic waves, a customized ratio, *r*,

$$r_{(ND_1/ND_2)} = mean(r_i) \pm std(r_i)\ with\ r_i = \frac{ND_{1i}}{ND_{2i}}, \quad (6.1)$$

was used, where ND_{1i} and ND_{2i} were the normalized displacement of the induced elastic wave at the i^{th} measurement position for samples 1 and 2, respectively. Because identical acquisition parameters were utilized, the i^{th} position corresponded to the same distance in both samples. Displacement amplitudes were normalized by dividing the elastic wave displacement amplitude at each measurement position by the displacement amplitude at the excitation position. If *r* was significantly greater than 1, the displacement in sample 2 damped faster than in sample 1. If *r* was significantly less than 1, sample 1 damped faster than sample 2. If *r* was close to 1, the damping was similar in both samples.

6.3 Results and discussion

As shown in Fig. 6.1(a), the elastic wave (EW) velocity measured by PhS-SSOCE in the gelatin samples was 3.76±0.2 m/s, which was very similar to the EW velocity in the agar samples of 3.64±0.3 m/s.

Fig. 6.1(b) shows the Young's modulus for the 14.0% gelatin and 1.1% agar phantoms obtained by equation 2.1 was 48.7±9.2 kPa and 46.6±8.2 kPa, respectively. Uniaxial mechanical compression tests (Model 5943, Instron Corp., MA) were conducted on the phantoms for elasticity validation. The measured Young's modulus was 47.6±5.3 kPa for the 14% gelatin and 44.9±6.6 kPa for the 1.1% agar phantoms as

shown in Figure 6.1(b). These results demonstrated that the 14.0% gelatin sample and 1.1% agar phantoms were of similar stiffness confirmed by both OCE measurements and uniaxial compression tests.

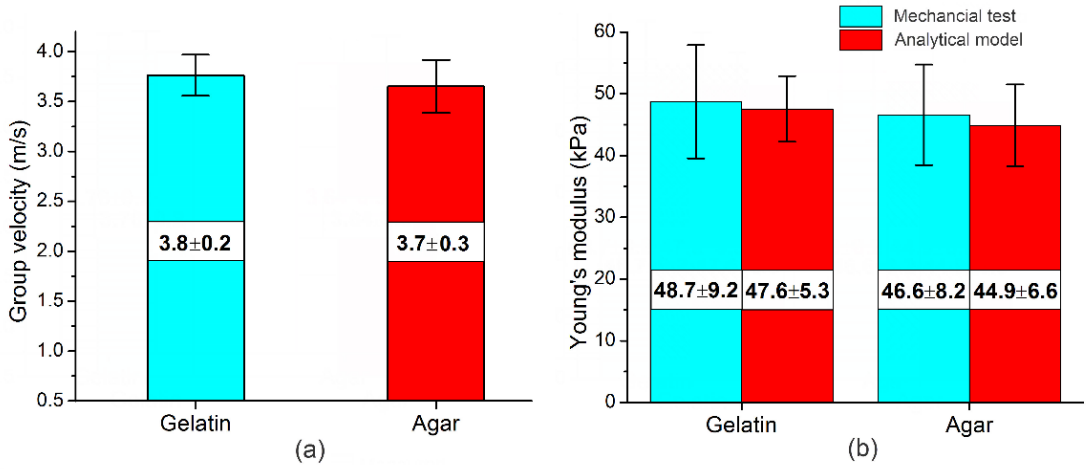

Figure 6.1. (a) EW velocities of the 14.0% gelatin (w/w) and 1.1% (w/w) agar phantom samples measured by PhS-SSOCE; (b) Comparison of estimated and measured Young's moduli of the 14.0% gelatin and 1.1% agar phantoms.

Fig. 6.2 displays the normalized displacement of induced elastic wave in (a) 14.0% gelatin phantom excited by two different pressure of air-pulse, 11 Pa and 22 Pa, and (b) gelatin and agar phantom in the same stiffness.

This ratio was first calculated for the same 14.0% gelatin phantom to examine the effects of different initial position displacements by changing the focused air-pulse pressure on the sample to 11 Pa and 22 Pa. The normalized displacement attenuation curves are shown in Fig. 6.3(a) with the ratio $r_{(22/11)} = 0.95 \pm 0.12$, which was very close to 1. As anticipated, this indicated that the initial displacement amplitude did not affect the damping speed of the elastic wave.

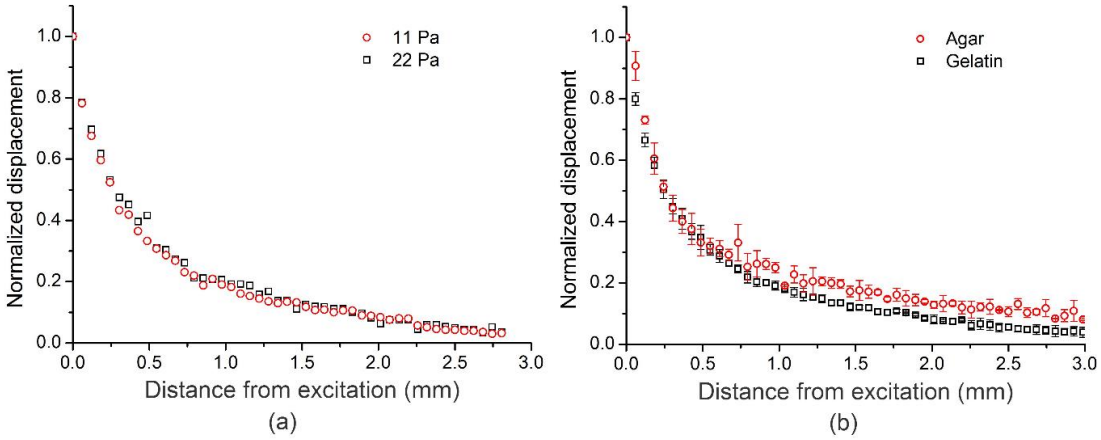

Figure 6.2. (a) Normalized elastic wave displacement amplitude attenuation curves of the same 14.0% agar phantom at two excitation pressures; (b) Comparison of the normalized elastic wave displacement amplitude attenuation curves of 14.0% gelatin and 1.1% agar phantoms.

This ratio was then calculated to compare the gelatin and agar phantoms. As shown in Figure 6.2(b), the normalized displacement in the agar phantoms was higher than in the gelatin phantoms at the same scan position. By using formula 6.1, $r_{(agar/gelatin)} = 1.56 \pm 0.47$, which demonstrated that the 14% gelatin damped faster than the 1.1% agar. This result was in agreement with previous findings that gelatin has higher viscosity than agar, which corresponds to faster damping [189]. Therefore, these comparisons showed that this method could be successfully utilized to distinguish two materials of similar stiffness.

To induce a similar measured corneal stiffness in the UT and CXL porcine corneas, the IOP of the whole eye was controlled by a custom-built controller comprising of a pressure transducer and micro-infusion pump connected in a feedback loop. The elastic wave was measured in a porcine cornea by the PhS-SSOCE system before and after UVA-Riboflavin induced CXL [153, 190]. Elastic wave measurements were taken at IOPs from 15-35 mmHg with 5 mmHg increments. The EW velocities in the UT and

CXL corneas at the various IOPs are presented in Table 6.1. It can be observed that before CXL, the EW velocity of the cornea at IOP = 30 mmHg was calculated as 3.6 ±0.4 m/s. After CXL, the EW velocity was 3.6 ±0.1 m/s at IOP = 20 mmHg. Therefore, based on the EW velocity, it might appear that the stiffness of the cornea is the same under these contrasting conditions.

Table 6.1 PhS-SSOCE measured EW velocities of an UT and CXL cornea at different IOPs.

IOP (mmHg)	UT	CXL
	EW Velocity (m/s)	EW Velocity (m/s)
15	1.5 ±0.1	2.7 ±0.1
20	2.3 ±0.1	3.6 ±0.1
25	3.0 ±0.3	4.0 ±0.1
30	3.6 ±0.4	4.2 ±0.2
35	3.7 ±0.4	4.7 ±0.5

After normalizing the elastic wave displacement amplitudes, the damping features of the elastic wave over the measurement positions were analyzed (Fig. 6.3). Based on formula 6.1, the ratio of $r_{(CXL/UT)}$ was calculated as 2.61 ±0.95, indicating that the damping speed of the cornea had significantly decreased after the CXL treatment. In addition, the normalized displacement attenuation curves were fitted by $y = ae^{bx}$ in which the parameter b was treated as the damping speed. According to the fitted results, the damping speed of the UT cornea (b_{UT} = -0.031 mm^{-1}) was almost twice the damping speed of the CXL cornea (b_{CXL} = -0.017 mm^{-1}), which confirmed that the damping speed decreased after CXL treatment. One possible reason for this result is that the CXL

treatment is a procedure that displaces water from the corneal tissue. The UT cornea contains more water, which is responsible for a higher viscosity. Therefore, the elastic wave damps faster in the UT cornea than the CXL cornea.

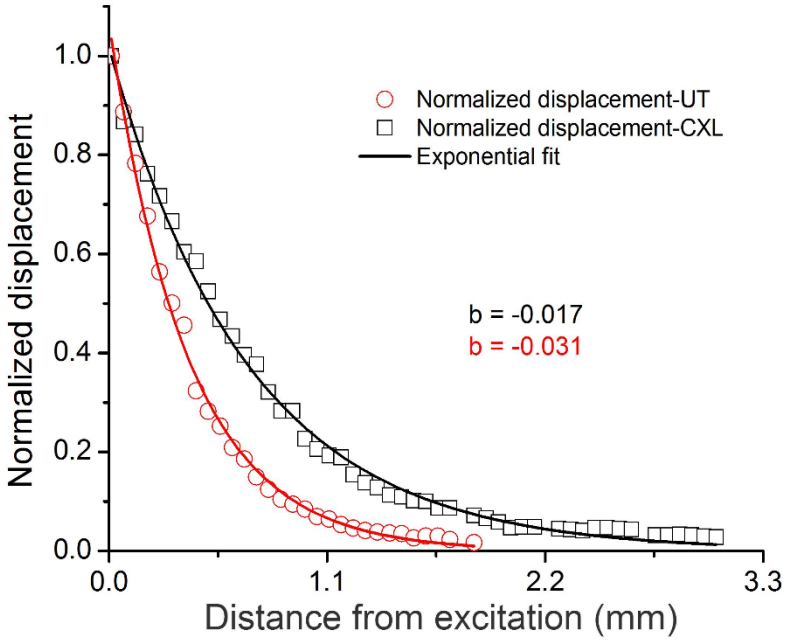

Figure 6.3 Comparison of the normalized elastic wave displacement amplitude attenuation curves and exponential fit of an UT and CXL porcine cornea at the same measured stiffness but different IOPs.

Kotecha et al. measured biomechanical parameters of UT eyes at different IOPs with the Ocular Response Analyzer (ORA, Reichert Inc., Depew, NY) and discussed how the viscosity was negatively correlated with measured corneal stiffness, indicating that the CXL cornea has lower viscosity than the normal one [135]. These results corroborate with our results. However, the ORA only provides the index of corneal hysteresis to reflect the corneal damping ability, it is unable to provide information about the cornea stiffness. Furthermore, the induced displacement in ORA is in the order of mm, which is hundreds of times larger than in the present method.

6.4 Conclusion

In this chapter, a novel method using PhS-SSOCE to distinguish UT and CXL corneas of the same measured stiffness but at different IOPs was demonstrated. This noninvasive method has potential to evaluate the biomechanical properties of the cornea *in vivo* for detecting the onset and progression of corneal degenerative diseases such as keratoconus. Future work would entail quantifying and separating the elasticity and viscosity of the cornea.

CHAPTER 7 – Evaluating the effects of Riboflavin/UV-A corneal collagen crosslinking on porcine corneal mechanical anisotropy with noncontact optical coherence elastography

Chapter 4 showed the capability of OCE to spatially map corneal elasticity, and a faster OCE technique to quantify the elasticity of cornea was introduced in Chapter 5. In this chapter, a novel noncontact OCE method which can provide a shear elastogram for evaluating the mechanical anisotropy of cornea is introduced. The mechanical anisotropic properties of the cornea can be an important indicator for determining the onset and severity of different diseases and may be able to provide critical information for assessing the efficacy of various therapeutic interventions, such as CXL and LASIK surgeries. However, the changes in the mechanical anisotropy of the cornea due to diseases or the aforementioned therapies is not known. Therefore there is an unmet need for a noninvasive technique that can determine the mechanical anisotropy of the cornea. Here I demonstrate the development and application of such a technique for evaluating the elastic anisotropy of the cornea and its hysteresis while cycling IOP. Moreover, the technique was applied to CXL corneas to evaluate its effects on the mechanical anisotropy and hysteresis as well. Elastic waves were induced in fresh *in situ* porcine corneas in the whole eye-globe configuration as described in previous chapters. A PhS-SSOCE system imaged the elastic wave propagation at stepped meridional angles, and the OCE measurements were repeated as the IOP was cycled. A new sliding window algorithm was implemented to obtain the spatially varying elastic wave velocity, which was utilized to generate a map of the elastic wave velocity. The results show that the

elastic anisotropy at the apex of the cornea becomes more pronounced at higher IOPs, and that there are distinct meridional angles of higher and lower stiffness.

7.1 Introduction

The anisotropic characteristics of corneal elastic properties can provide valuable information for determining the onset and severity of many diseases. For example, the collagen fibril orientation in corneas with keratoconus is distinctly different than in healthy corneal tissue [191]. The application of X-ray scattering [192], electron microscopy [193], visible light confocal microscopy [194], second harmonic generation (SHG) imaging [195], and polarization sensitive optical coherence tomography [196] (PS-OCT) has greatly improved our understanding of the lamellar microstructure of the cornea. For instance, X-ray diffraction has been used to quantify the orientation and spatial distribution of the collagen fibrils in the cornea and showed that keratoconus significantly affects this arrangement [191]. While X-ray diffraction and electron microscopy have provided a wealth of information about collagen fibril organization in the cornea due to their very high spatial resolutions, they require fixed samples and are fundamentally infeasible for *in vivo* applications. On the other hand, visible light confocal microscopy can be used to detect some ocular diseases *in vivo* [194]. Due to the transparency of corneal collagen at visible wavelengths, visible light confocal microscopy could not directly study the collagen in the cornea. Instead, morphological changes at the cellular level were correlated with alterations to the collagen fibrils. SHG imaging has been able to elucidate the lamellar microstructure in rat corneas *in vivo* [197]. However, this method required flattening of the cornea, which may have altered the collagen structure and orientation. Recently, PS-OCT has been utilized to measure the

birefringence of the cornea [196]. Further investigation with this technique has determined that the corneal birefringence correlated with the dominant collagen fiber orientation in the human cornea [198]. As OCT has proven to be a valuable tool in ophthalmology [199], PS-OCT may be a clinically viable option for rapidly assessing the changes in the corneal lamellae orientation in corneal diseases such as keratoconus. While promising, all of the above mentioned optical imaging techniques measure the optical effects of collagen fibril orientation in the cornea. Intuitively, one can expect that the anisotropic organization of the collagen fibers would lead to variations in the biomechanical properties of cornea as well. In addition to the inherent collagen structure, IOP can also influence the biomechanical properties of the cornea [62, 65, 152]. While the overall stiffness of the cornea shows a measurable hysteresis while cycling IOP [101], the elastic anisotropic hysteresis has not yet been investigated.

The mechanical anisotropy of the cornea has previously been studied by inflation tests combined with the finite element modeling [200], mechanical testing on excised strips of corneal tissue at orthogonal angles [143], and computational modeling utilizing X-ray scattering data [144]. These techniques have provided valuable insight into the elastic anisotropy of the cornea, but they are currently impractical for *in vivo* use. Recently, supersonic shear wave imaging (SSI) has been demonstrated as a method for measuring the elastic anisotropy of the cornea at various IOPs *in vivo*, but required general anesthesia and immersion of the cornea in water [142].

Riboflavin/UV-A induced CXL (UV-CXL) is an emerging clinically available technique for treating keratoconus by stiffening the cornea and increasing its resistance to further degeneration [133]. While it is understood that UV-CXL alters corneal

collagen fibril organization, subsequently altering corneal mechanical properties [164], there have been no direct investigations on the changes in the elastic anisotropy of the cornea caused by UV-CXL. Furthermore, the current clinical UV-CXL protocol is uniform despite individual disease presentation or severity. However, an optimal treatment would consider pre-existing biomechanical properties and would incorporate the effects of the CXL treatment itself. Thus, a method with the capability to noninvasively provide a pre-existing biomechanical properties map of cornea is highly desired in clinical, which also can be used to track the outcome after UV-CXL treatment.

In this chapter, we describe a noncontact method of assessing the elastic anisotropy of the cornea utilizing noncontact PhS-SSOCE. The OCE measurements as described in Chapter xx were repeated on the porcine samples, which were rotated at stepped meridional angles. The group velocity of the elastic wave was spatially mapped to investigate the elastic anisotropy of the cornea. The IOP was cycled to reveal the IOP-dependent mechanical anisotropy and hysteresis of the cornea. Furthermore, the effects of UV-CXL on the mechanical anisotropy of the cornea were investigated by crosslinking fellow eyes.

7.2 Materials and methods

7.2.1 Experimental setup

Details of the PhS-SSOCE system can be found in Chapter 2. The experimental setup is shown in Fig. 7.1.

The fresh juvenile (4 to 6 months) porcine eyes (Sioux-Preme Pork Products, n=6, 3 pairs of fellow eyes) were obtained and kept fresh at 4˚C in a refrigerator. All experiments were conducted immediately upon receipt of the samples, which was within

24 hours of enucleation. Two pairs of virgin fellow eyes were measured. For the third pair of fellow eyes, the OCE measurements were taken on one virgin eye, while the fellow eye was CXL treated. The CXL procedure is described in detail in Chapter xx. Artificial IOP control, which is detailed in Chapter xx, was used to cycle the IOP.

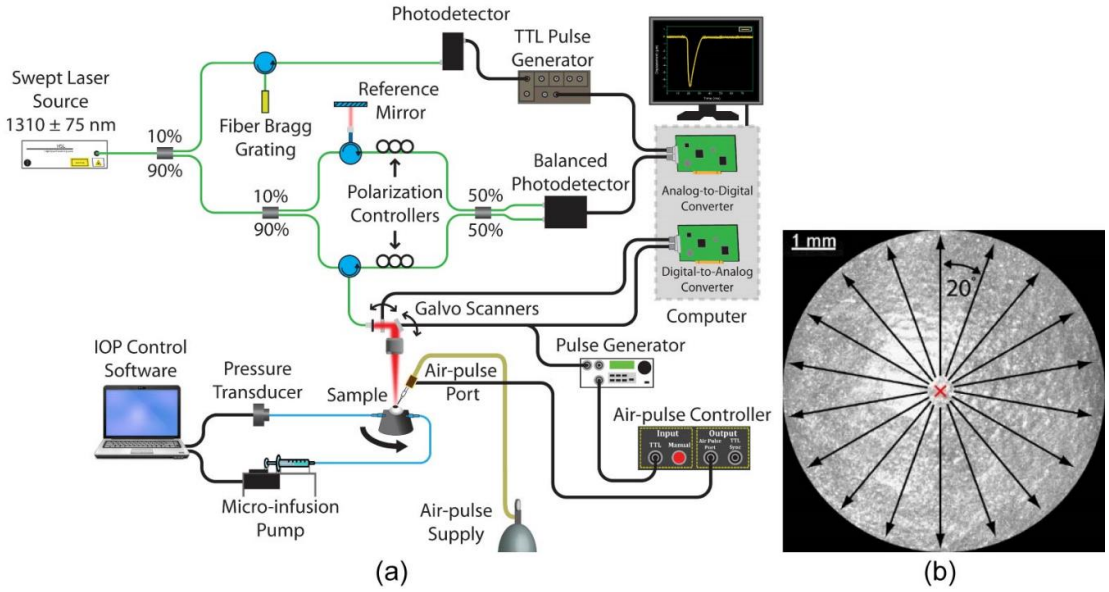

Figure 7.1. (a) OCE experimental setup. (b) En-face view of a 3D OCT image of a porcine cornea. The red "X" indicates the excitation position and the arrows are elastic wave propagation directions that were imaged by the PhS-SSOCE system.

The elastic waves were imaged by 251 successive M-mode images spanning ~7 mm across the corneas with the apex at the middle of the scan position. After the OCE measurements from one meridian were acquired, the eye globes were rotated by 20 °, and the OCE measurement was repeated at the new meridional angle. Because the elastic waves were induced at the apex, which was also at the center of the OCE scan region, two meridional angles were acquired at once. Thus, the samples were rotated only 9 times for 180 °in order to obtain a full rotation. An illustration of the acquisition methodology is shown in Fig. 7.1(b). The OCE measurements were repeated at IOPs increasing from

15 to 30 mmHg at increments of 5 mmHg. To investigate the elastic anisotropic hysteresis, the IOP was then decreased from 30 to 15 mmHg, also in 5 mmHg steps. To ensure that the corneas were properly hydrated, the corneas were instilled with 0.9% PBS every 4 minutes during the OCE measurements. The central corneal thickness (CCT) was monitored to ensure that any effects of dehydration on the corneal elasticity were minimized. Before all OCE measurements, the eyes were pre-conditioned by cycling the IOP between 15 and 30 mmHg twice.

7.2.2 Group Velocity Calculations

The raw unwrapped vertical temporal phase profiles from the surface of the cornea, $\varphi_{surface}(t)$, were converted to displacement, $d_{surface}(t)$, using equation 2.1 [91], and the raw unwrapped vertical temporal phase profiles inside the cornea, $\varphi_{inside}(t)$, were corrected due to the motion of the corneal surface and the refractive index mismatch between air and the corneas and converted to displacement, $d_{inside}(t)$, by [169]

$$d_{inside}(t) = \frac{\lambda_0}{4\pi n_{cornea}}\left[\varphi_{inside}(t) + \frac{(n_{cornea}-n_{air})}{n_{air}}\varphi_{surface}(t)\right], \qquad (7.1)$$

where n_{cornea} = 1.376, and λ_0 was the central wavelength of the PhS-SSOCT system.

The conventional group velocity of the induced elastic wave was calculated based on our previously introduced method [116]. Then, a sliding window of ~750 μm was utilized to obtain a spatial map of the elastic wave group velocity. The normalized temporal displacement profiles for a given imaged in-depth layer were cross-correlated with the displacement profile at the first position of that given window. The cross-correlation analysis yielded the elastic wave propagation delays, which were then linearly fitted to the corresponding propagation distances to calculate the velocity for that given in-depth layer and for that given velocity calculation window. When calculating the elastic wave

propagation distances, the curvature of the corneas, as determined from the structural OCT image, was taken into consideration to ensure accuracy of the calculations. The velocity calculated for a window was spatially mapped as the velocity for the central pixel of the window, and the window was then shifted by one pixel and the procedure was repeated. The procedure was reiterated for each in-depth layer of the cornea and averaged depth-wise. This resulted in a 2D elastic wave group velocity map illustrating the depth-wise averaged spatial distribution of the elastic wave velocities.

7.2.3 Anisotropy Calculations

The modified planar anisotropy coefficient for every measured angle r_θ was calculated to quantify the changes in the elastic anisotropy [201]

$$r_\theta = \frac{(v_\theta + v_{\theta+90^\circ} - 2v_{\theta+45^\circ})}{2}, \tag{7.2}$$

where v_θ was the velocity at that given angle, $v_{\theta+90^\circ}$ was the velocity 90 °clockwise from the given angle, and $v_{\theta+45^\circ}$ was the velocity 45 °clockwise from the given angle. Because angular measurements were taken every 20 °, the values for $v_{\theta+90^\circ}$ and $v_{\theta+45^\circ}$ were linearly interpolated from the OCE measurements. A larger magnitude of r_θ corresponds to a greater degree of elastic anisotropy.

7.3 Results

The results from one pair of virgin eyes is presented, followed by the same results from the pair of eyes where the OCE measurements were taken on a virgin eye and the CXL fellow eye. In both studies, group velocity was measured, and presented in two drawings: angle-wise velocity, and spatially mapped velocity.

The angle-wise conventional group velocity of a virgin cornea was plotted in Fig. 7.2, the vertical axis (0 °/180 °) corresponds to the superior/inferior axis, and the horizontal

axis (90 °/270 °) was the nasal/temporal axis of the eye. The results clearly show that the elastic wave propagated faster at ~40 °/220 ° as compared to other directions for all IOPs. The results also indicate that the overall velocity correlated positively with the IOP. The mean velocity for all meridional angles and both samples is plotted in Fig. 7.3. The mean velocities were calculated to be 1.72 ± 0.85, 2.63 ± 0.92, 3.89 ± 1.16, and 4.93 ± 1.35 m/s at IOPs of 15, 20, 25, and 30 mmHg while increasing IOP, respectively. The mean velocities while decreasing IOP were 4.48 ± 1.25, 3.50 ± 0.95, and 2.27 ± 1.04 m/s at IOPs of 25, 20, and 15, respectively.

The spatially-mapped elastic wave velocity calculated by the sliding window algorithm as a function of IOP in a pair of fellow eyes (both virgin) is shown in Fig. 7.4, which corresponds to the samples shown in Fig. 7.2.

The group velocity calculated by the conventional method (not the sliding window technique) was utilized to calculate the modified planar anisotropy coefficient, as shown in Fig. 7.5.

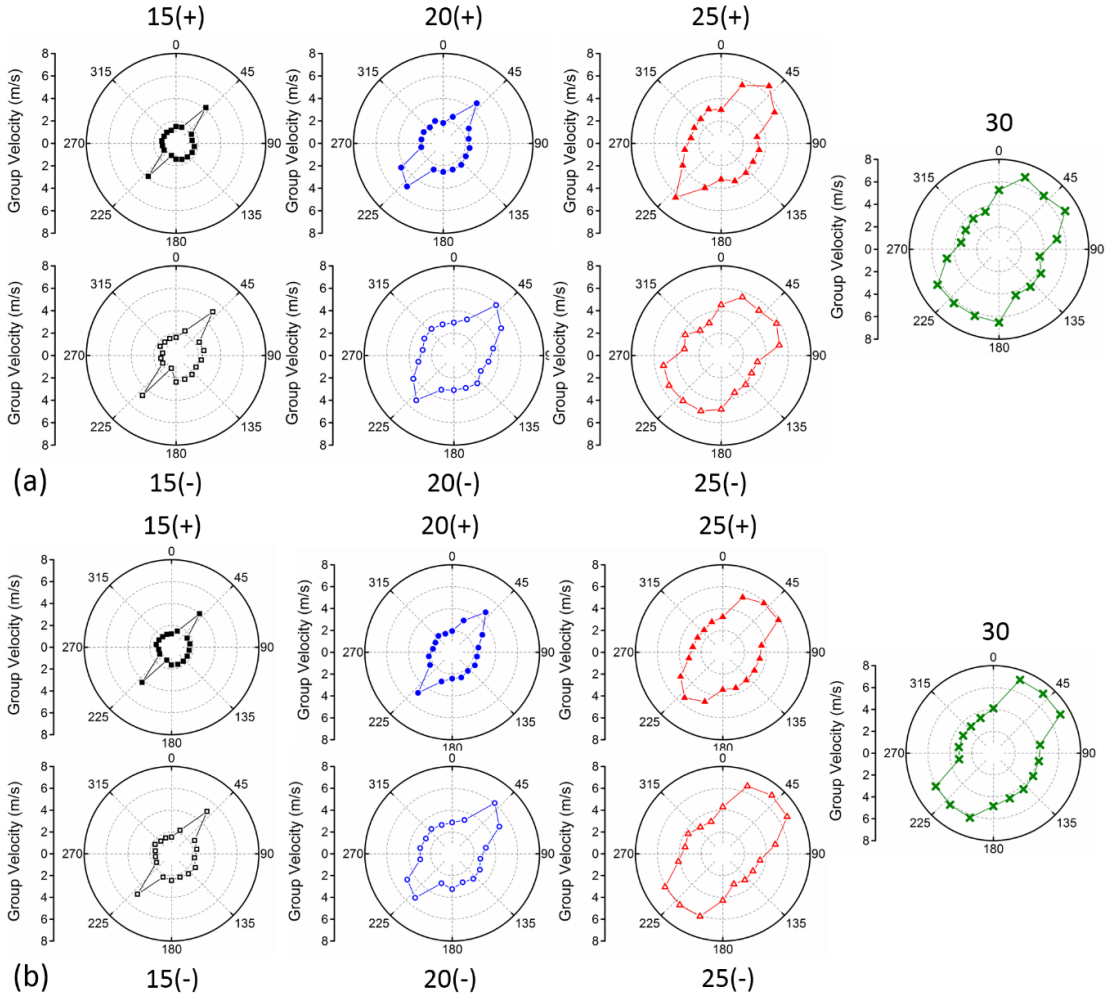

Figure 7.2. Group velocity polar maps of the air-pulse induced elastic wave for a pair of virgin porcine corneas ((a) and (b)) at different IOPs. 15, 20, 25, and 30 indicate the IOP in mmHg, and "+" indicates increasing IOP, and "-" indicates decreasing IOP.

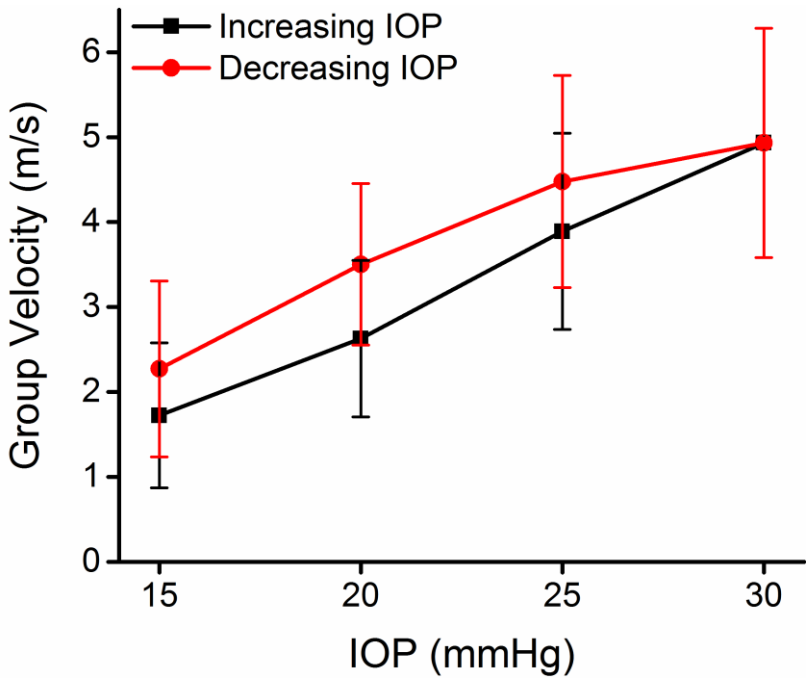

Figure 7.3. Mean velocity of all meridional angles and 4 virgin samples (2 pairs of fellow eyes) at different IOPs.

The standard deviation (StDev) of r_θ of all meridional angles for a given IOP was also calculated to study the overall anisotropy as well as the elastic hysteresis of the cornea while cycling IOP. The results are plotted in Fig. 7.6, which show that the anisotropy of the cornea is minimal at 15 mmHg IOP, became greater as IOP increased, and then reduced as the IOP was decreased. The results also clearly show that at the same IOP, the StDev of r_θ is greater while reducing IOP than increasing IOP, demonstrating that there is a hysteresis to the mechanical anisotropy of the cornea while cycling IOP.

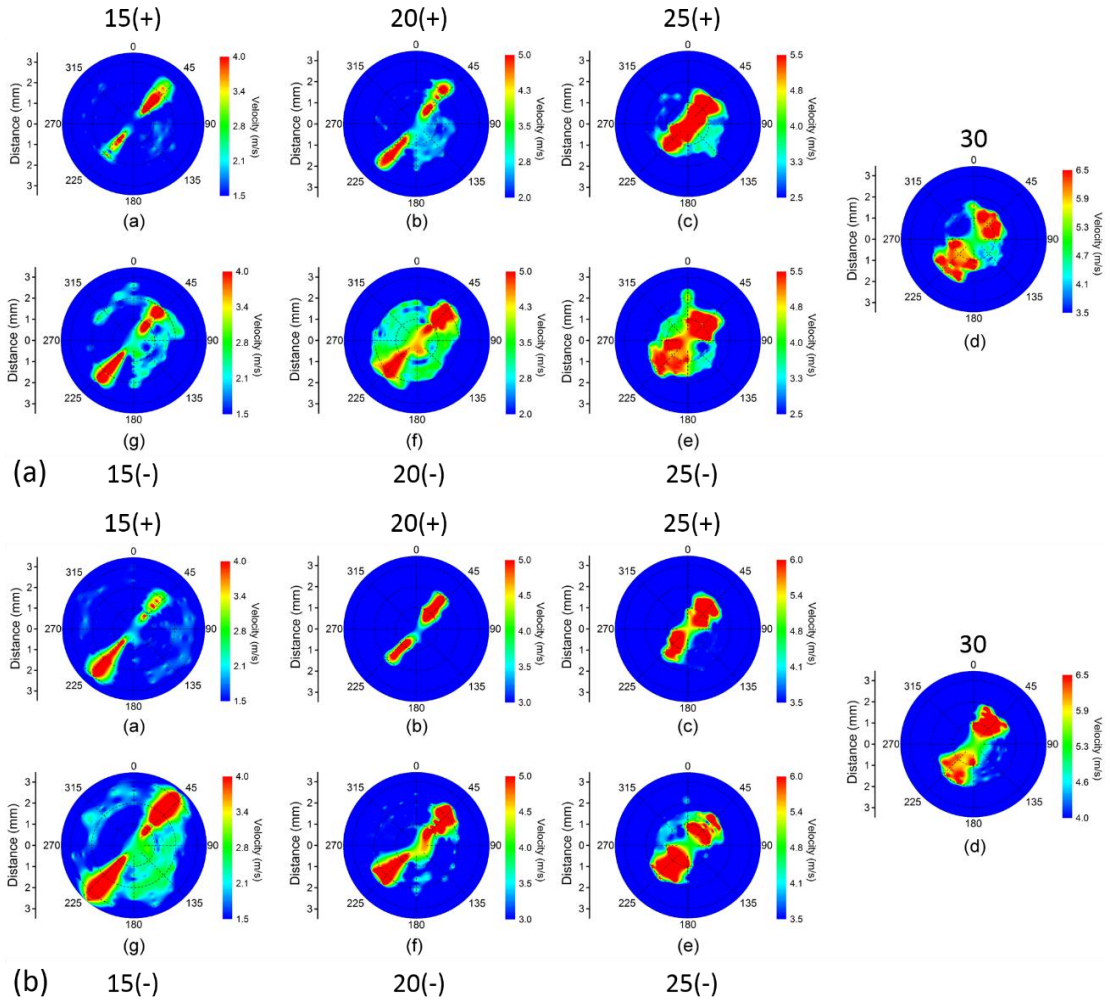

Figure 7.4. Spatial map of the group velocity of the air-pulse induced elastic wave for a pair of virgin porcine corneas ((a) and (b)) at different IOPs. 15, 20, 25, and 30 indicates the IOP in mmHg, and "+" indicates increasing IOP, and "-" indicates decreasing IOP.

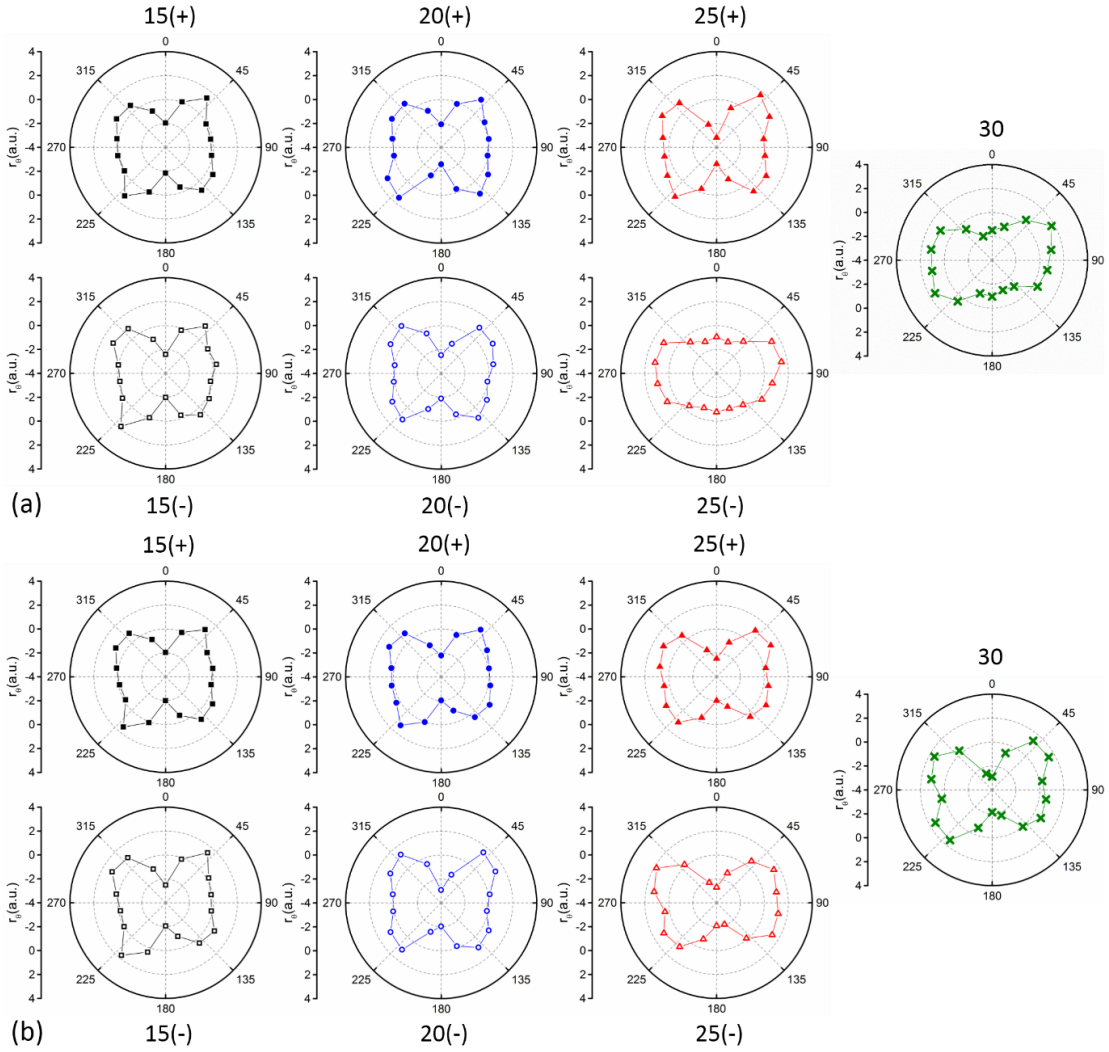

Figure 7.5. The r_θ values for each meridional angle in the cornea for a pair of virgin porcine corneas ((a) and (b)) at different IOPs. 15, 20, 25, and 30 indicates the IOP in mmHg, and "+" indicates increasing IOP, and "-" indicates decreasing IOP.

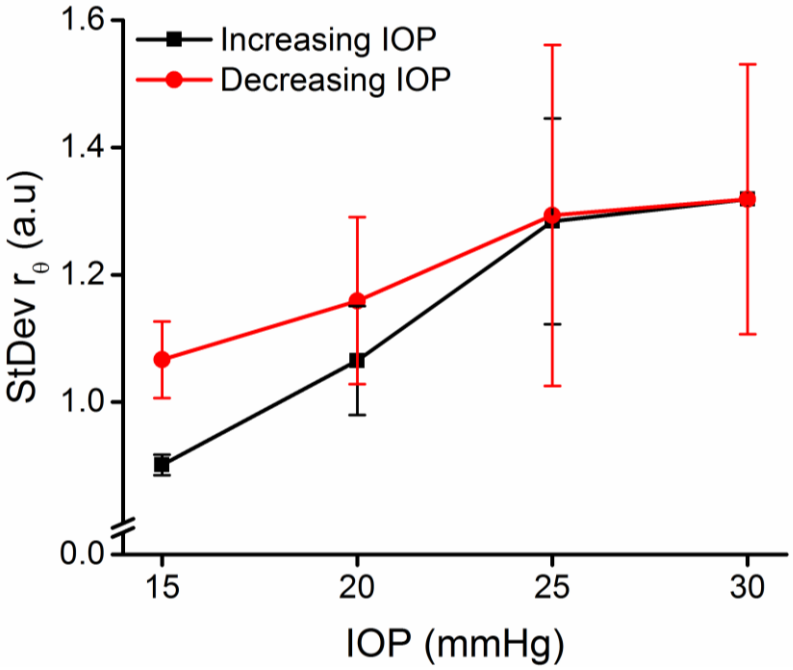

Figure 7.6. Standard deviation of r_θ for a given IOP for all meridional angles and all 4 samples (2 pairs of fellow virgin eyes) while IOP was cycled.

The same analysis was performed on the third pair of corneas, in which one cornea was untreated while the fellow cornea was CXL. The meridional angle-wise conventional group velocity is plotted in Fig. 7.7, Similar to Fig. 7.2, the vertical axis (0°/180°) corresponded to the superior/inferior axis, and the horizontal axis (90°/270°) was the nasal/temporal axis of the eye. Similar to the paired virgin samples, ~40°/220° is faster than other directions for all IOPs in both virgin and CXL corneas. The results also indicate that the velocity increased after CXL, indicating that CXL stiffened the cornea. Moreover, the velocity correlated with IOP in both the virgin and CXL samples. The sample-wise mean velocities of the two corneas are plotted in Fig. 7.8. The mean velocities of all the meridional angles of the virgin cornea were calculated as 2.45±0.28, 4.75±1.77, 5.08±1.94, and 5.85±2.54 m/s at IOPs of 15, 20, 25, and 30 mmHg while

increasing IOP, respectively. The elastic wave velocity of all meridional angles while decreasing IOP was 5.33±1.83, 5.36±2.08, and 3.13±0.89 m/s at IOPs of 25, 20, and 15mmHg, respectively. The mean velocities of all the meridional angles of the CXL cornea were 3.46±0.74, 6.24±1.77, 6.65±2.01, and 10.04±2.73 at IOPs of 15, 20, 25, and 30 mmHg while increasing IOP, respectively. The elastic wave velocity of all meridional angles of the CXL cornea while decreasing IOP were 6.29±1.62, 6.24±1.28, and 4.37 ± 0.56 m/s at the IOP of 25, 20, and 15 mmHg while decreasing IOP, respectively.

The spatially-mapped elastic wave velocity calculated by sliding window algorithm as a function of IOP is shown in Fig. 7.9(a) virgin cornea, and 7.9(b) CXL cornea.

The standard deviation (StDev) of r_θ of all angles while IOP was cycled was also calculated to study the overall anisotropy of this pair of corneas, as well as the elastic hysteresis. The results are plotted in Fig. 7.10. Similar to Fig. 6, which shows that the anisotropy of both of the virgin cornea (Fig. 10(a)) and the CXL cornea (Fig. 7.10(b)) is minimal at 15 mmHg IOP, but became greater as the IOP was increased, and then decreased as IOP decreased.

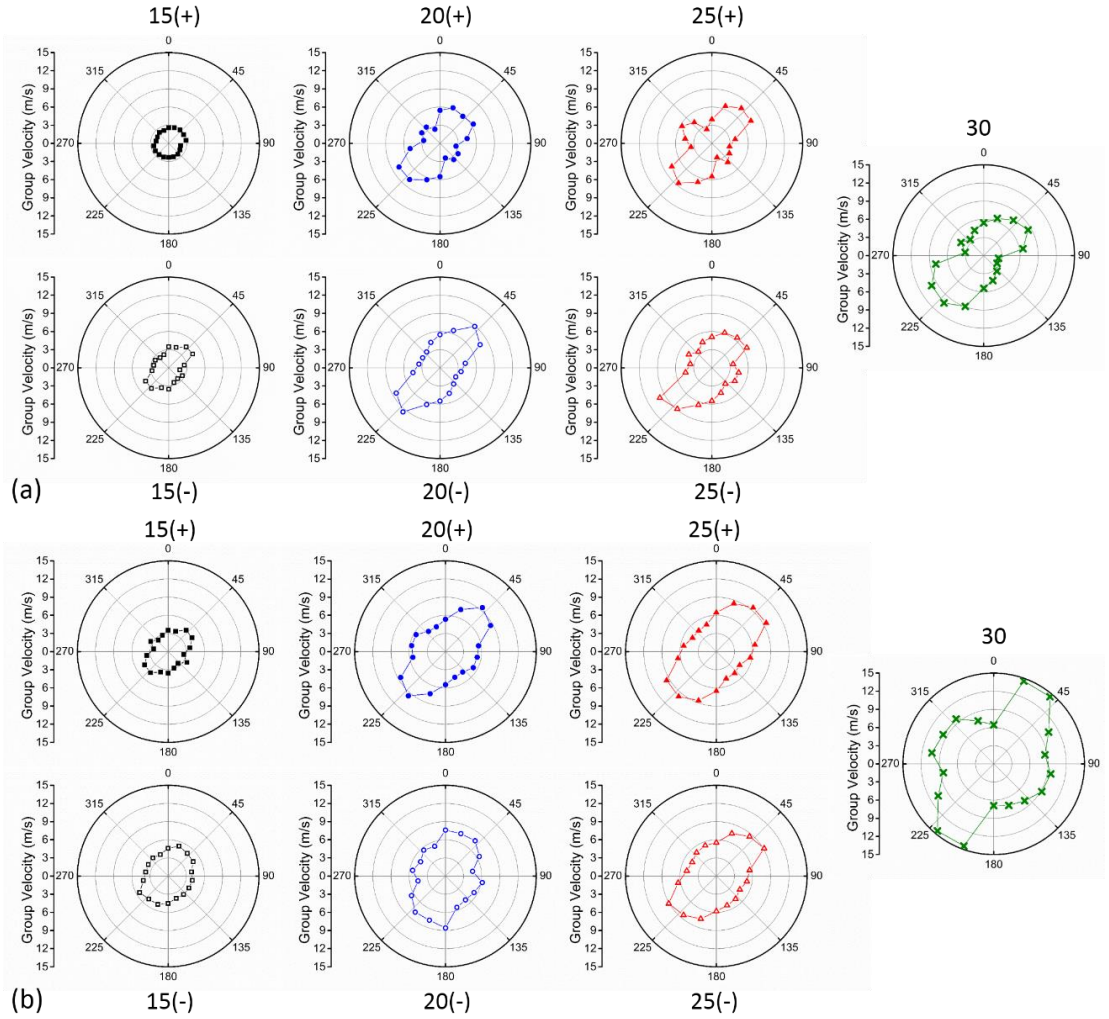

Figure 7.7. Group velocity polar maps of the air-pulse induced elastic wave for a pair of porcine corneas ((a): Virgin and (b): CXL) at different IOPs. 15, 20, 25, and 30 indicates IOP in mmHg, and "+" indicates increasing IOP, and "-" indicates decreasing IOP.

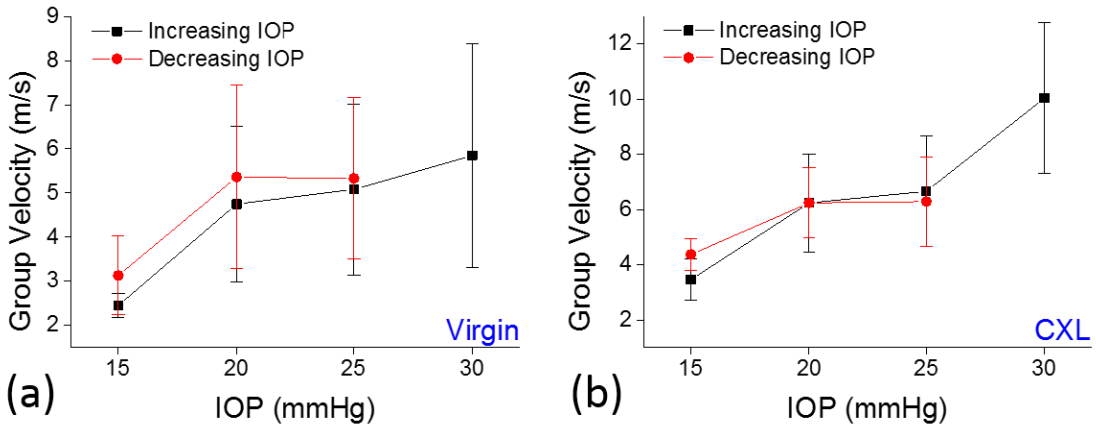

Figure 7.8. Mean velocity of a sample of all meridional angles at a given IOP of paired corneas where one eye was (a) Virgin and the fellow eye was (b) CXL.

7.4 Discussion

We have introduced a noncontact method of OCE to investigate the mechanical anisotropy of the cornea by imaging focused air-pulse induced elastic wave propagation at incremental meridional angles. Furthermore, the IOP-dependent biomechanical anisotropy and elastic anisotropy hysteresis were investigated while the IOP was cycled. Our results show that in both the virgin and CXL corneas, the elastic anisotropy of the cornea becomes more pronounced as the IOP was increased and that there is a measureable mechanical anisotropic hysteresis. An elastogram of the anisotropy of biomechanical properties of cornea has been provided, which may provide crucial information for accurate diagnosis of ocular diseases in early stages, customization of CXL treatment, and tracking the outcome of treatments on cornea.

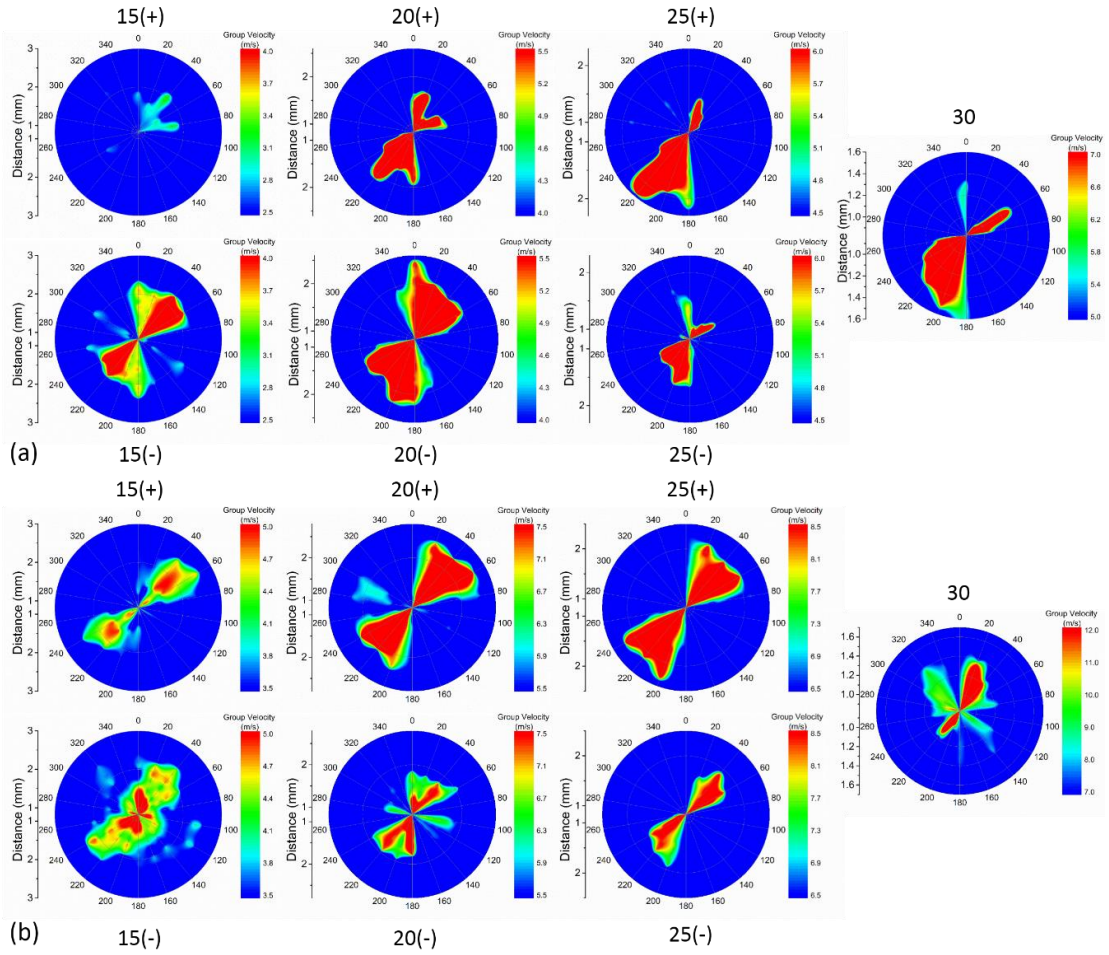

Figure 7.9. Spatial map of the group velocity as calculated by the sliding window algorithm of the air-pulse induced elastic wave for a pair of porcine corneas ((a): Virgin and (b): CXL) at different IOPs. 15, 20, 25, and 30 indicates the IOP in mmHg.

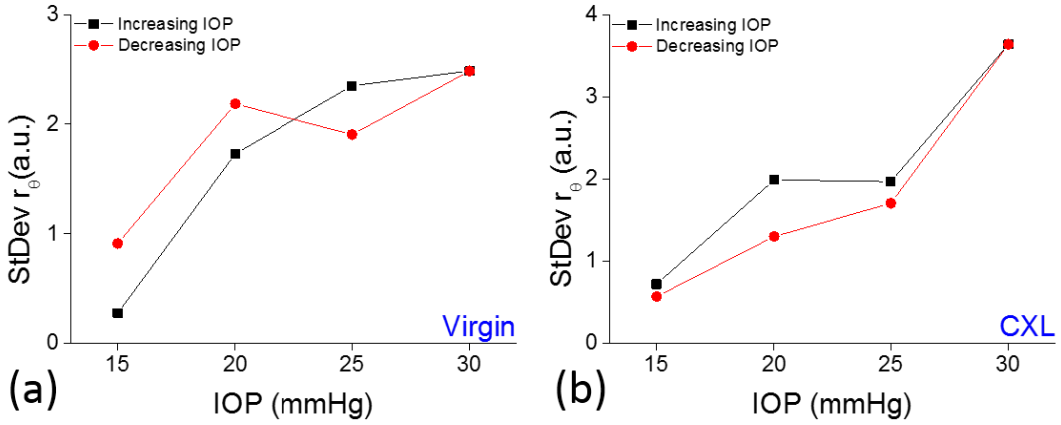

Figure 7.10. Standard deviation of r_θ as quantified for all meridional angles while IOP was cycled ((a), Virgin cornea, and (b) CXL cornea).

For further clinical application of this method, the acquisition time will need to be significantly reduced. Here, each M-mode image was ~100 ms in duration and 251 M-mode images were acquired for each pair of radial angles, even though the data acquisition speed is more than ten times shorter than the technique described in Chapter 4, this method still may be unfeasible for clinical application. However, we have recently demonstrated the possibility for assessment of the elasticity of a porcine cornea at various IOPs using PhS-OCE at speed of ~1.5 million A-scans per second [160]. Due to the significantly faster A-scan rate, a different scanning paradigm was utilized where successive B-scans were imaged (B-M-mode) as opposed to consecutive M-mode images (M-B-mode) as in this work. The elastic wave was directly imaged utilizing B-M-mode imaging, resulting in a total acquisition time of ~30 ms for a single line scan. Because of the reduced data size and subsequent processing time, an elasticity estimate was given in minutes. Moreover, only a single air-pulse was required, whereas in this work, each OCE measurement position had to be synchronized with an air-pulse

stimulation. In addition, the ANSI Z136.1 corneal laser exposure limit was not exceeded, whereas M-B-mode imaging utilized in this study far exceeded the limit. Further development of even faster sources and parallel scanning and acquisition [202] have pushed OCT A-scan rates beyond 28 MHz [79]. When coupled with graphics processing unit accelerated OCE [203], these techniques may be able to provide near real-time 3D assessments of the elastic anisotropy of the cornea. Furthermore, the distance between the air gate and the cornea will need to be increased. Development of a more tightly focused air-pulse stimulation technique is underway to increase the distance between the cornea and the air gate to reduce the risk of damage due to motion.

In this study, the local mechanical anisotropy of the cornea became more apparent at higher IOPs, which has also been recently shown by SSI [142]. Higher IOPs correspond to a larger stress and thus, differences in elasticity became more pronounced. Mechanical testing on corneal strips excised at orthogonal angles showed minimal difference in the corresponding stress-strain curves [184]. However, after increasing the strain rate, the difference between the strip specimens widened, which may indicate that the rate, in addition to the magnitude of the stress, may play an important factor in how the collagen fibers align and react during loading. The non-linear stress-strain curve of the cornea may also explain the greater inhomogeneity at higher IOPs.

The planar anisotropy coefficient, r_θ, was modified to obtain the relative elastic anisotropy of each OCE measured angle. Originally, r_θ, was developed to assess the quality of rolled steel by calculating the strain of the metal at 0 º, 45 º, and 90 º [201]. However, this only provides a single value showing the overall performance of the metal by calculating a ratio of the strains of the three measured directions. Consequently, r_θ

was calculated for each measured OCE angle to quantify the relative anisotropic stiffness for each direction rather than for the whole sample.

In this study, we have not investigated depth-resolved elastic anisotropy. The elastic wave velocities were averaged depth-wise, and therefore the stiffness obtained from the velocity reflected the elasticity over the entire thickness of the cornea. The depth-wise spatial resolution from the group velocity is limited because the wavelength of the elastic wave is on the order of millimeters. However, application of spectral analysis of the elastic wave propagation (as a function of frequency) can reveal the depth-resolved micro-scale elasticity distribution in the cornea [115], which may be able to elucidate the depth-dependent changes in the elastic anisotropy of the cornea.

Only the elastic anisotropy was investigated in this work, which is not fully indicative of the biomechanical properties of the cornea. We have recently developed a modified Rayleigh Lamb Frequency Equation (RLFE) that can provide the elasticity as well as viscosity of the cornea by incorporating the dispersion of the elastic wave and appropriate boundary conditions [204]. Future work will involve application of this method to determine the viscoelastic anisotropy of the cornea. Furthermore, only the elastic anisotropy close to the apex of the cornea was assessed. It has been shown that the collagen fibril orientation is distinctly different at the periphery of the cornea as compared to the apex [145]. Future investigations will assess the elastic anisotropy of the cornea near the limbus.

Previous OCE investigations have shown a measurable mechanical hysteresis in the cornea while cycling IOP [101], which corroborates with our work. However, we have also shown that there is a mechanical anisotropic hysteresis, which may mean that the

corneal fibril arrangement is semi-permanently altered by elevated IOPs. These results warrant future work to understand the degree of re-arrangement and whether techniques such as IOP pre-conditioning can affect the mechanical anisotropic hysteresis.

7.5 Conclusion

This work has presented a noncontact method of evaluating the elastic anisotropy of the cornea at various IOPs. The results show that the anisotropy is minimal at low IOPs but becomes readily apparent once the IOP is elevated to 20 mmHg and higher. For example, the StDev of r_θ increased from 0.60 at 15 mmHg IOP to 1.25 at 30 mmHg IOP for virgin corneas, and from 0.72 at 15 mmHg IOP to 3.64 at 30 mmHg IOP for CXL cornea. Meanwhile, 2D elastograms of the cornea at various conditions (IOPs and CXL) were also provided. Because of the noncontact nature and small excitation force required, PhS-SSOCE may be potentially useful for clinically mapping the elasticity of cornea, and/or evaluating the anisotropy of the cornea, which may aid in the quantitative assessment of ocular diseases, customization of CXL treatment, and evaluating the effects of various therapeutic interventions.

CHAPTER 8 – Assessing mechanical properties of tissue phantoms with non-contact optical coherence elastography and Michelson interferometric vibrometry

In previous chapters, we have demonstrated that OCE is capable to assess the biomechanical properties of cornea. However, there is a major limitation for wider adoption of OCE, which is the cost. Thus, a low cost system may be able to provide sufficient information for accurate elastographic assessment. In this chapter, I compare two methods of optical elastography for quantifying Young's modulus of tissue-mimicking agar phantoms of various concentrations: laser Michelson interferometric vibrometer (LMIV) and phase-stabilized swept source optical coherence elastography (PhS-SSOCE). The elasticity of the phantoms was estimated from the velocity of air-pulse induced elastic waves as measured by the two techniques. The results show that both techniques were able to accurately assess the elasticity of the samples as compared to uniaxial mechanical compression testing. While the LMIV is significantly more cost-effective, it cannot directly provide the absolute elastic wave temporal profile, nor can it offer in-depth information, which the PhS-SSOCE system can.

8.1 Introduction

OCE is clearly capable of assessing the biomechanical properties of tissues completely non-destructively [97, 205]. However, OCT setups, particularly phase-sensitive systems, can be complex and expensive. Simpler and more cost-effective techniques such as Michelson interferometer-based laser vibrometery could potentially also provide measurements for calculating the velocity of the air-pulse induced elastic wave [206]. Laser vibrometry has been successfully used in various applications due to its high sensitivity, simplicity, and relatively low cost, which has enabled detection of

very small vibrations on the order of the source wavelength. Laser vibrometry was first applied in different engineering fields, such as modal analysis, vibration and noise testing, characterizing loudspeakers, and assessing piezoceramic transducers [207]. Recently, laser vibrometry has gained traction in biomedical and bioengineering applications, such as auditory research [208, 209], dentistry [210, 211], cardiology [212-214], as well as elastography and rheology [215-220].

In this chapter, a PhS-SSOCE system and laser Michelson interferometric vibrometer (LMIV), both developed in our lab, were utilized to measure the velocity of a focused air-pulse induced elastic waves propagating in tissue-mimicking agar phantoms of various concentrations. The Young's modulus was then quantified from the wave velocity and was compared to the stiffness as measured by uniaxial mechanical compression testing. The results show that the velocities as measured by both systems were very similar, and the estimated Young's modulus was consistent with mechanical testing.

8.2 Materials and Method

A home-built focused air-pulse delivery system induced elastic waves in tissue-mimicking agar phantoms of various concentrations (1%, 1.5%, 2%, w/w, n=3 for each concentration) [118] The elastic waves were then detected by the LMIV and PhS-SSOCE systems, separately. The air-pulse delivery system was synchronized with the OCE and LMIV systems.

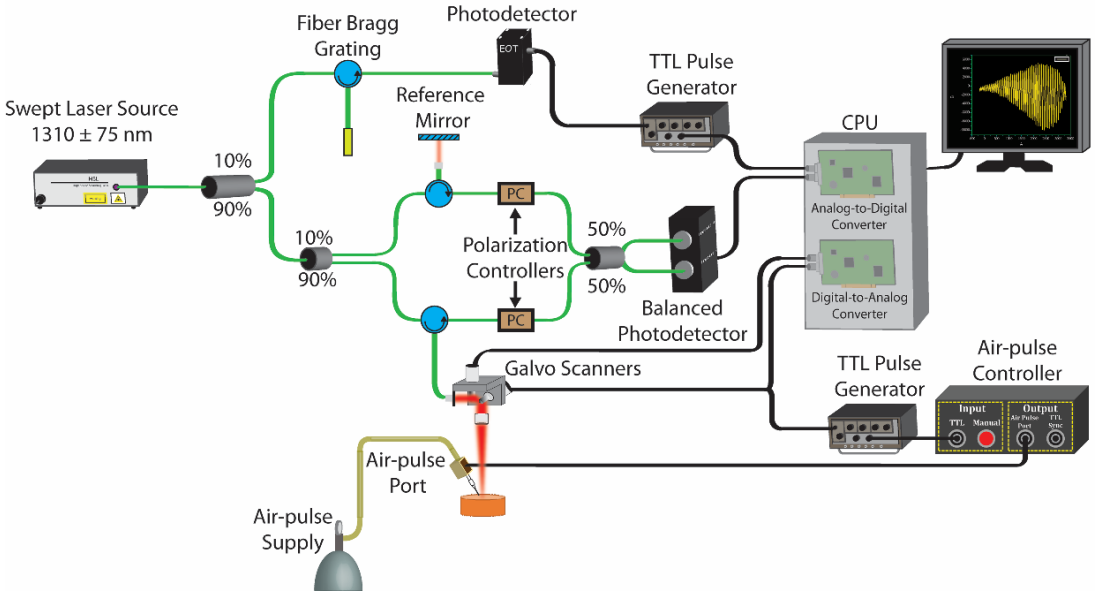

Figure 8.1. Schematic of PhS-SSOCE experimental setup.

The details of the PhS-SSOCE system has been described in chapter 2. A schematic of the experimental setup is displayed in Fig. 8.1. Further details about the PhS-SSOCT system can be found in our previous work [91, 113]. The experimental acquisition and data processing methods are detailed in our previous work [116]. Simply, successive M-mode images were acquired in a line, and the M-mode frame trigger was synchronized with the air-pulse so that effectively, the same elastic wave was imaged.

LMIV schematic is depicted in Fig. 8.2. The LMIV employed a Helium-Neon (HeNe) laser with wavelength of 633 nm and output power of 1.5 mW (model 31005, Research Electro-Optics, Inc., Boulder, CO). The output of the HeNe laser was expanded and collimated to 90% of the objective lens aperture to maximize photon collection. The light beam was then split into sample and reference arms using a 50:50 non-polarizing cube beam splitter. In the sample arm, the beam was transmitted through a 10X microscope

objective and focused on the sample surface. In the reference arm, the beam was directed to a matching 10X microscope objective and focused onto the surface of a silver mirror. After the reflected light beam passed through the beam splitter, the interference signal was detected by a silicon photodetector (model DET100A, Thorlabs, Inc., USA). The temporal intensity output from the photodetector was captured by a digital oscilloscope (model DS4014, Rigol Inc., USA). The air-pulse stimulation and the data acquisition were synchronized by a TTL signal, which was provided by a digital pulse generator (model 575, BNC Inc., USA). The system was assembled on a 3-inch thick optical breadboard and supported with four sorbothane isolation pads to maximize system stability and minimize environmental noise. During the LMIV measurements, all data was acquired with the same acquisition window and oscilloscope sampling settings. Six co-linear measurements positions were recorded on each sample, and the distance between two adjacent positions was 1 mm. The time t for the wave to propagate from a reference measurement position to each location was obtained by cross-correlation analysis. The elastic wave velocity, c, was then obtained by the inverse slope of the linear fit of the propagation distances, Δd, to the elastic wave propagation delays, Δt [221].

Since the tissue-mimicking agar phantoms can be treated as an isotropic homogeneous elastic material, the Young's modulus [222], E, was estimated using equation 2.3 [113, 120, 122], and the density of phantom was taken as 1.02 k/gm^3, and Poisson ratio was set as 0.49 [100, 120]. For all experiments, the output pressure of the air-pulse was $\leqslant$ 10 Pa. Uniaxial mechanical compression testing (model 5943, Instron Inc., MA, USA) was performed on the same samples after OCE and LMIV measurement [122].

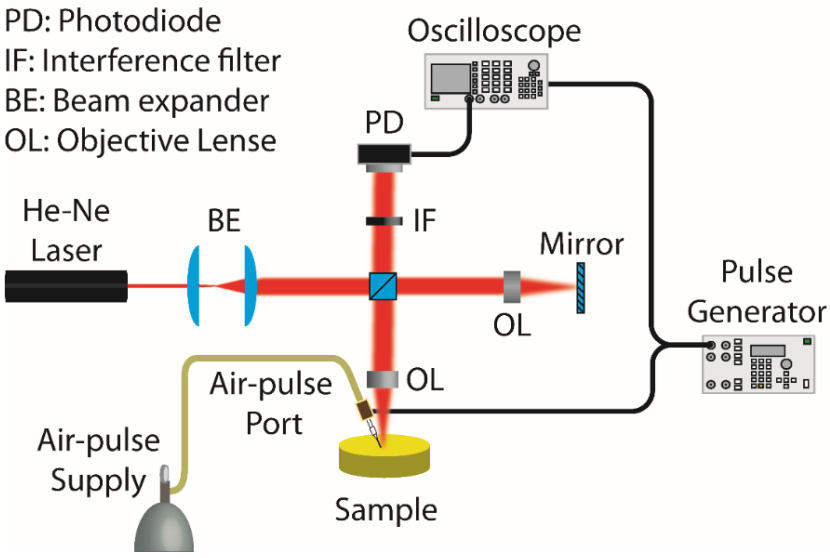

Figure 8.2 Schematic of LMIV experimental setup

8.3 Results

Fig. 8.3 shows typical 1% agar phantom surface response signal to air-pulse at various positions during OCE (Fig. 8.3(a)) and LMIV (Fig. 8.3(b)) measurement. During OCE measurements, 501 M-mode measurements were acquired over 6.9 mm. Fig. 8.3(a) shows typical surface responses to the air-pulse stimulation at OCE measurement positions which were 0.1 mm apart, and the first acquisition position was 1 mm away from the excitation position. During LMIV experiments, the first measurement position was also 1 mm away from the stimulation position, but successive measurement positions were 1 mm apart as depicted in Fig. 8.3(b).

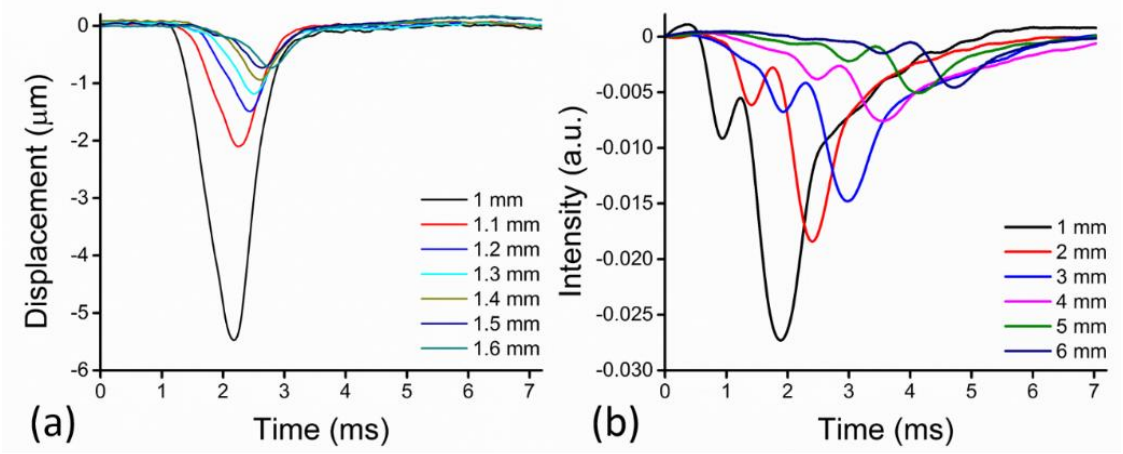

Figure 8.3. Sample surface responses of a 1% agar phantom recorded during (a) OCE and (b) LMIV experiment at the indicated distances from the air-pulse excitation.

Figure 8.4 shows the elastic wave propagation velocity as measured by both systems. The group velocity as measured by OCE was 1.72 ±0.25 m/s, 3.41 ±0.49 m/s, and 5.11 ±0.26 m/s in the 1%, 1.5%, and 2% agar phantoms, respectively. The velocities measured by the LMIV from the same agar samples were 1.75 ±0.03 m/s, 3.66 ±0.26 m/s, and 5.13 ±0.28 m/s, respectively. Statistical testing by a paired t-test showed no significant difference between the two systems (P = 0.90, 0.25, and 0.89 for the 1%, 1.5%, and 2% phantoms, respectively – all over 5%).

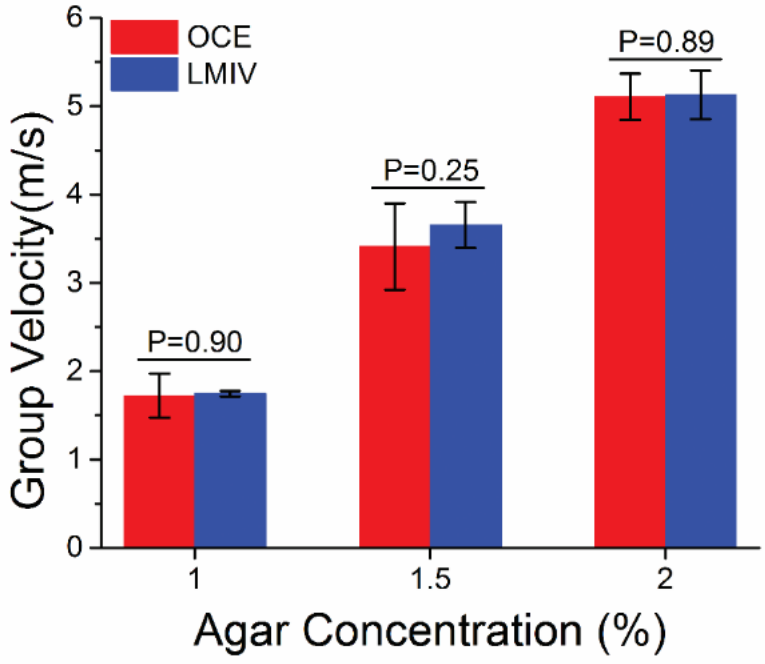

Figure 8.4. Elastic wave propagation velocity measured by OCE and LMIV. Statistical testing was performed by a paired t-test to demonstrate that the velocity measurements made by both systems were not different. The respective P-values are labeled.

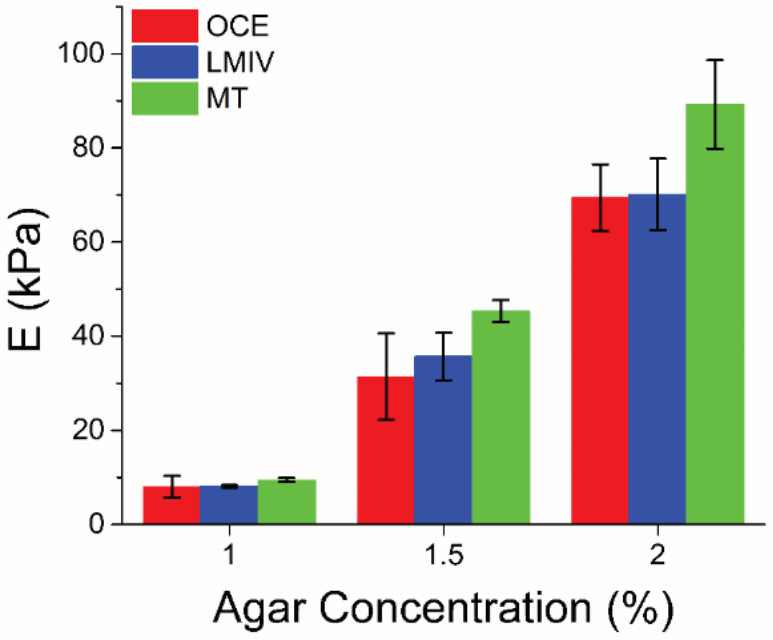

Figure 8.5. Young's modulus (E) estimated by the OCE system, LMIV, and as measured by mechanical testing (MT).

Figure 5 shows the Young's modulus (E) of the samples estimated based on the OCE and LMIV measurements using equation 2.1 and as measured by "gold standard" mechanical testing system. The Young's moduli of the 1%, 1.5%, and 2% agar phantoms as estimated by OCE were 8.01 ± 2.3 kPa, 31.39 ± 9.19 kPa, and 69.45 ± 7.07 kPa, respectively. The elasticities as quantified by the LMIV were 8.12 ± 0.28 kPa, 35.69 ± 5.07 kPa, and 70.14 ± 7.57 kPa for the 1%, 1.5%, and 2% phantoms, respectively. The stiffness of the same samples was also measured by mechanical testing (MT), which resulted in a stiffness of 9.46 ± 0.43 kPa, 45.34 ± 2.32 kPa, and 89.25 ± 9.4 kPa for the 1%, 1.5%, and 2% samples, respectively.

8.4 Discussion

The shape of the displacement as measured by the LMIV (Fig. 8.3(b)) was somewhat similar to the displacements detected by the OCE system in this work (Fig. 8.3(a)) and previous work [113, 122]. The differences in the shape of the temporal profiles can be attributed to the different ways of each technique to measure the displacement of the sample. OCE measures the optical path difference between sample and reference arm, and the LMIV measures the intensity of light reflected from the sample surface. More specifically, the elastic wave may undulate similar to a wave in water, and the resulting change in sample surface geometry relative to incident beam may explain the kink during the inward process. Furthermore, OCE can easily provide absolute displacement, which can be used in other OCE techniques, such as compressional OCE for stress/strain analysis [223].

Statistical testing via a paired t-test showed that there was no significant difference between the velocities measured by both systems, with P = 0.90, 0.25, and 0.89 for the

1%, 1.5%, and 2% phantoms, respectively (Fig. 8.4). However, the LMIV can only measure the wave propagation at the surface of the sample since internal scattering is dominated by the specular reflection from the surface. In contrast, OCE can provide depth-resolved elasticity measurements [115]. To further demonstrate the depth-resolved elasticity characterization by OCE, a sandwich-type agar phantom was constructed with a 2% agar layer between two layers of 1% agar (Fig. 8.6). Because the air-pulse induced elastic wave wavelength is large, spectral analysis was utilized to provide depth-resolved elasticity assessment [115], and all three layers were differentiated successfully. Figure 8.6 shows the phase velocity of the air-pulse induced elastic wave at 180 Hz. The boundary layers are marked by the dashed red line.

The Young's moduli estimated from the group velocities were smaller than as measured by mechanical testing. However, this is in agreement with our very recent investigation and can be explained by assumptions about sample geometry in Eq. 8.1 and the non-linearity of the agar stress-strain curve [122].

The LMIV can provide very rapid detection of elasticity since the data acquisition and post-processing are minimal. During OCE study, 501 successive M-mode images were acquired at 100 ms per M-mode image, resulting in an acquisition time of approximately half a minute. However, due to the large data size, the post-processing time can be on the order of several minutes. Since each OCE measurement position results in a longer acquisition time and more data, there is an intrinsic trade-off between spatial resolution and acquisition and processing times. Lateral measurements in the LMIV system were made by translating the sample, whereas the galvanometer-mounted mirrors were used to make measurements at the transverse locations in the OCE system.

An automated motorized linear stage would dramatically speed up the acquisition time of the LMIV, but the speed would be limited to ensure that no damage was caused to the sample or that there was no slipping of the sample. Hence, elastographic measurements made with OCE are simpler because the probe beam is moved and not the sample. Furthermore, the LMIV requires precise alignment in order to capture the reflected photons. Moreover, OCE can provide a depth-resolved image of the sample, making alignment significantly easier.

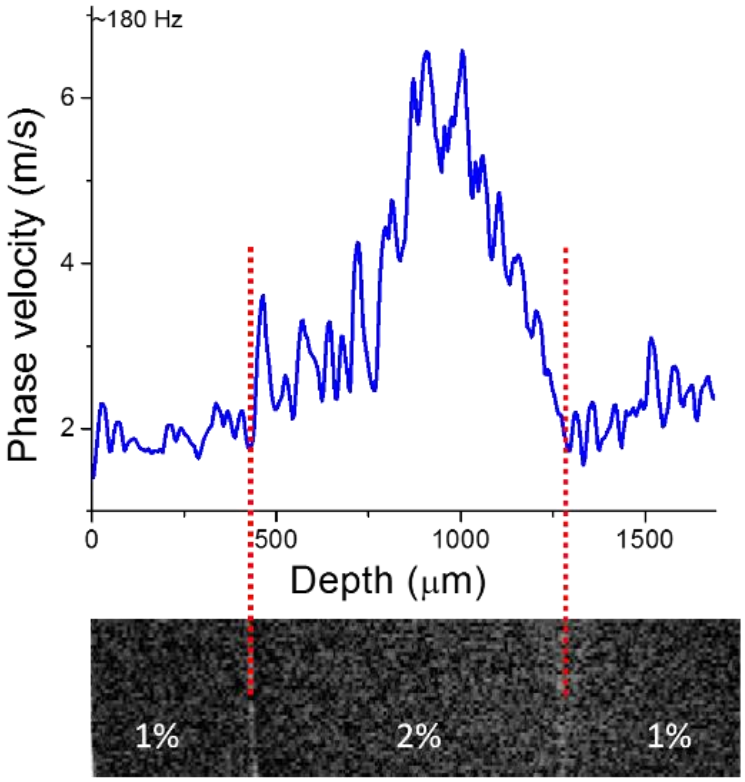

Figure 8.6. Phase velocity of the air-pulse induced elastic wave at 180 Hz in a sandwich-type agar phantom (top) with OCT image of the phantom (bottom). The layer boundaries are marked by the dashed red line.

In this study, successive M-mode images were acquired and an air-pulse excitation was synchronized with each measurement. This technique may not be feasible for *in vivo*

cornea measurement due to multiple excitations and the extended acquisition time, which may lead to excessive laser exposure. However, we have recently developed a technique that takes advantage of recent advances in OCT sources by directly imaging the propagation of an air-pulse induced elastic wave. Here, only a single excitation was necessary for a line measurement and the MPE limit for the sample (cornea) was not exceeded [160]. However, the spatial and temporal resolutions were still limited as compared to the OCE technique described in this work. Recently, GPU-accelerated compressional OCE has been demonstrated, enabling near real-time 3D elasticity assessment [203]. Combining high-performance computing would drastically reduce the processing time of the OCE post-processing and would also enable near real-time characterization of tissue biomechanical properties and is currently under development.

Another core issue for comparison of the two techniques is the cost. The approximate total costs of building the OCE and LMIV systems are listed in Table 8.1. The LMIV system is approximately one-tenth the cost of the OCE system. The LMIV system requires a simple HeNe laser, whereas the OCE system requires a broadband low coherence swept source laser. As the LMIV system is an open space system, there are no expensive fiber based components. Fiber optical components are becoming more mainstream and prices continue to decrease. However, the price disparity will still exist due to the sheer difference in complexity of the two systems.

Table 8.1. Approximate cost in $US of the OCE and LMIV systems used in this study

	OCE	LMIV
Light source	$ 20000	$ 850
Optical components	$ 4500	$ 2550
Scan	$ 2850	$ 0
Control unit	$ 6500	$ 600
Data acquisition	$ 10000	$ 150
Data Processing	$ 3000	$ 500
Total cost	$ 46850	$ 4650

8.5 Conclusion

In this chapter, we have utilized two optical techniques, laser Michelson interferometric vibrometry (LMIV) and optical coherence elastography (OCE) to assess the elasticity of tissue-mimicking agar phantoms. A focused air-pulse induced elastic waves in the samples, which were then detected by the two techniques. The stiffness of the agar phantoms as quantified from the velocity were measured by the LMIV and OCE systems was in good agreement. The LMIV system was significantly less complex and expensive as compared to the OCE system, but the LMIV system cannot provide-depth resolved elasticity assessment. Therefore, if depth-resolved elasticity or high spatial resolutions are not necessary, then LMIV may be a simple and cost-effective technique to measure the elasticity of tissues completely noninvasively.

CHAPTER 9 – Conclusion

This dissertation demonstrates a series of developments of detection methods to assess the biomechanical properties for both biological and medical applications, with a focus on the development of novel noncontact optical coherence elastographic techniques for noninvasive characterization of corneal biomechanical properties. Specifically, the work can be summarized into the following seven chapters:

1) Characterization of the biomechanical properties of tissue mimicking phantoms, an ocular phantom, and mouse cornea *in vivo*;

2) Assessment the biomechanical properties of mouse corneas of different ages *in vivo*;

3) The development of a method to spatially map the localized elasticity of the rabbit cornea *in situ* after partial CXL;

4) Rapid characterization of the biomechanical properties of *in situ* porcine corneas before and after CXL at different IOPs;

5) The development of method to differentiate UT and CXL porcine corneas of the same measured stiffness;

6) Evaluation of the effects of CXL on porcine corneal mechanical anisotropy;

7) A comparison of two optical techniques for assessing the mechanical properties of tissue phantoms: OCE and LMIV.

This dissertation represents the frontier of the emerging field of OCE from both the development of techniques and their applications. The contributions of this dissertation research lie in biomedical optics and are mainly reflected in providing low-coherence optical methods and techniques, which are capable of assessing the biomechanical properties of the cornea with information at a scale that could not be achieved with

current imaging and sensing approaches. The work presented in this dissertation can act as a foundation for the further development and the future applications of the proposed methods and techniques in basic biological studies as well as clinical or preclinical environment.

Although the techniques presented in this dissertation were based on the demand to assess the biomechanical properties of cornea, these techniques also can be used to characterize other soft tissues, such as skin, kidney, crystalline lens, cartilage, tumor, and so on.

References

1. Tuchin, V.V. and V. Tuchin, *Tissue Optics: Light Scattering Methods and Instruments for Medical Diagnosis*. Vol. 13. 2007: SPIE press Bellingham.

2. Maceo, B.M., F. Manns, D. Borja, D. Nankivil, S. Uhlhorn, E. Arrieta, A. Ho, R.C. Augusteyn, and J.M. Parel, *Contribution of the Crystalline Lens Gradient Refractive Index to the Accommodation Amplitude in Non-Human Primates: In Vitro Studies.* J Vis, 2011. 11(13): p. 23.

3. Paszek, M.J., N. Zahir, K.R. Johnson, J.N. Lakins, G.I. Rozenberg, A. Gefen, C.A. Reinhart-King, S.S. Margulies, M. Dembo, D. Boettiger, D.A. Hammer, and V.M. Weaver, *Tensional Homeostasis and the Malignant Phenotype.* Cancer Cell, 2005. 8(3): p. 241-54.

4. Athanasiou, A., A. Tardivon, M. Tanter, B. Sigal-Zafrani, J. Bercoff, T. Deffieux, J.L. Gennisson, M. Fink, and S. Neuenschwander, *Breast Lesions: Quantitative Elastography with Supersonic Shear Imaging--Preliminary Results.* Radiology, 2010. 256(1): p. 297-303.

5. Kennedy, B.F., K.M. Kennedy, and D.D. Sampson, *A Review of Optical Coherence Elastography: Fundamentals, Techniques and Prospects.* Select Top in Quant Elec, IEEE J, 2014. 20(2): p. 272-288.

6. Dulinska, I., M. Targosz, W. Strojny, M. Lekka, P. Czuba, W. Balwierz, and M. Szymonski, *Stiffness of Normal and Pathological Erythrocytes Studied by Means of Atomic Force Microscopy.* J Biochem Biophys Methods, 2006. 66(1-3): p. 1-11.

7. Mathur, A.B., A.M. Collinsworth, W.M. Reichert, W.E. Kraus, and G.A. Truskey, *Endothelial, Cardiac Muscle and Skeletal Muscle Exhibit Different Viscous*

and Elastic Properties as Determined by Atomic Force Microscopy. J Biomech, 2001. 34(12): p. 1545-53.

8. Laurent, V.M., S. Kasas, A. Yersin, T.E. Schaffer, S. Catsicas, G. Dietler, A.B. Verkhovsky, and J.J. Meister, *Gradient of Rigidity in the Lamellipodia of Migrating Cells Revealed by Atomic Force Microscopy.* Biophys J, 2005. 89(1): p. 667-75.

9. Sinkus, R., J. Lorenzen, D. Schrader, M. Lorenzen, M. Dargatz, and D. Holz, *High-Resolution Tensor Mr Elastography for Breast Tumour Detection.* Phys Med Biol, 2000. 45(6): p. 1649-64.

10. Samani, A., J. Bishop, C. Luginbuhl, and D.B. Plewes, *Measuring the Elastic Modulus of Ex Vivo Small Tissue Samples.* Phys Med Biol, 2003. 48(14): p. 2183-98.

11. Nightingale, K., S. McAleavey, and G. Trahey, *Shear-Wave Generation Using Acoustic Radiation Force: In Vivo and Ex Vivo Results.* Ultrasound Med Biol, 2003. 29(12): p. 1715-23.

12. Samani, A., J. Zubovits, and D. Plewes, *Elastic Moduli of Normal and Pathological Human Breast Tissues: An Inversion-Technique-Based Investigation of 169 Samples.* Phys Med Biol, 2007. 52(6): p. 1565-76.

13. Athanasiou, K.A., M.P. Rosenwasser, J.A. Buckwalter, T.I. Malinin, and V.C. Mow, *Interspecies Comparisons of in Situ Intrinsic Mechanical Properties of Distal Femoral Cartilage.* J Orthop Res, 1991. 9(3): p. 330-40.

14. Agache, P.G., C. Monneur, J.L. Leveque, and J. De Rigal, *Mechanical Properties and Young's Modulus of Human Skin in Vivo.* Arch Dermatol Res, 1980. 269(3): p. 221-32.

15. Rho, J.Y., R.B. Ashman, and C.H. Turner, *Young's Modulus of Trabecular and Cortical Bone Material: Ultrasonic and Microtensile Measurements.* J Biomech, 1993. 26(2): p. 111-9.

16. Gamble, G., J. Zorn, G. Sanders, S. MacMahon, and N. Sharpe, *Estimation of Arterial Stiffness, Compliance, and Distensibility from M-Mode Ultrasound Measurements of the Common Carotid Artery.* Stroke, 1994. 25(1): p. 11-6.

17. Chen, E.J., J. Novakofski, W.K. Jenkins, and W.D.O. Brien, *Young's Modulus Measurements of Soft Tissues with Application to Elasticity Imaging.* IEEE Transactions on Ultrasonics, Ferroelectrics, and Frequency Control, 1996. 43(1): p. 191-194.

18. Gennisson, J.L., T. Deffieux, E. Mace, G. Montaldo, M. Fink, and M. Tanter, *Viscoelastic and Anisotropic Mechanical Properties of in Vivo Muscle Tissue Assessed by Supersonic Shear Imaging.* Ultrasound Med Biol, 2010. 36(5): p. 789-801.

19. Hamilton, K.E. and D.C. Pye, *Young's Modulus in Normal Corneas and the Effect on Applanation Tonometry.* Optom Vis Sci, 2008. 85(6): p. 445-50.

20. Akhtar, R., M.J. Sherratt, J.K. Cruickshank, and B. Derby, *Characterizing the Elastic Properties of Tissues.* Mater Today (Kidlington), 2011. 14(3): p. 96-105.

21. Cross, S.E., Y.S. Jin, J. Rao, and J.K. Gimzewski, *Nanomechanical Analysis of Cells from Cancer Patients.* Nat Nanotechnol, 2007. 2(12): p. 780-3.

22. Kumar, S. and V.M. Weaver, *Mechanics, Malignancy, and Metastasis: The Force Journey of a Tumor Cell.* Cancer metastasis reviews, 2009. 28(1-2): p. 113-127.

23. Ortiz, D., D. Pinero, M.H. Shabayek, F. Arnalich-Montiel, and J.L. Alio, *Corneal Biomechanical Properties in Normal, Post-Laser in Situ Keratomileusis, and Keratoconic Eyes.* J Cataract Refract Surg, 2007. 33(8): p. 1371-5.

24. Andreassen, T.T., A.H. Simonsen, and H. Oxlund, *Biomechanical Properties of Keratoconus and Normal Corneas.* Exp Eye Res, 1980. 31(4): p. 435-41.

25. Chirambo, M.C. and D. Benezra, *Causes of Blindness among Students in Blind School Institutions in a Developing Country.* Br J Ophthalmol, 1976. 60(9): p. 665-8.

26. Krachmer, J.H., R.S. Feder, and M.W. Belin, *Keratoconus and Related Noninflammatory Corneal Thinning Disorders.* Surv Ophthalmol, 1984. 28(4): p. 293-322.

27. Ruberti, J.W., A.S. Roy, and C.J. Roberts, *Corneal Biomechanics and Biomaterials.* Annu Rev Biomed Eng, 2011. 13: p. 269-95.

28. Roberts, M.D., Y. Liang, I.A. Sigal, J. Grimm, J. Reynaud, A. Bellezza, C.F. Burgoyne, and J.C. Downs, *Correlation between Local Stress and Strain and Lamina Cribrosa Connective Tissue Volume Fraction in Normal Monkey Eyes.* Investigative Ophthalmology & Visual Science, 2010. 51(1): p. 295-307.

29. Roberts, C., *The Cornea Is Not a Piece of Plastic.* J Refract Surg, 2000. 16(4): p. 407-13.

30. Pepose, J.S., S.K. Feigenbaum, M.A. Qazi, J.P. Sanderson, and C.J. Roberts, *Changes in Corneal Biomechanics and Intraocular Pressure Following Lasik Using Static, Dynamic, and Noncontact Tonometry.* Am J Ophthalmol, 2007. 143(1): p. 39-47.

31. Pinero, D.P., J.L. Alio, R.I. Barraquer, R. Michael, and R. Jimenez, *Corneal Biomechanics, Refraction, and Corneal Aberrometry in Keratoconus: An Integrated Study.* Invest Ophthalmol Vis Sci, 2010. 51(4): p. 1948-55.

32. Wells, P.N., *Ultrasound Imaging.* Phys Med Biol, 2006. 51(13): p. R83-98.

33. Bushberg, J.T., *The Essential Physics of Medical Imaging.* (Lippincott Williams & Wilkins), 2002.

34. Miller, K., *Method of Testing Very Soft Biological Tissues in Compression.* J Biomech, 2005. 38(1): p. 153-8.

35. Fenster, A. and D.B. Downey, *3-D Ultrasound Imaging: A Review.* IEEE Engineering in Medicine and Biology Magazine, 1996. 15(6): p. 41-51.

36. Robert, H.W., *Confocal Optical Microscopy.* Reports on Progress in Physics, 1996.

37. Lichtman, J.W. and J.A. Conchello, *Fluorescence Microscopy.* Nat Methods, 2005. 2(12): p. 910-9.

38. Mukamel, S., *Femtosecond Optical Spectroscopy: A Direct Look at Elementary Chemical Events.* Annual Review of Physical Chemistry, 1990. 41(1): p. 647-681.

39. Boas, D.A., D.H. Brooks, E.L. Miller, C.A. DiMarzio, M. Kilmer, R.J. Gaudette, and Z. Quan, *Imaging the Body with Diffuse Optical Tomography.* IEEE Signal Processing Magazine, 2001. 18(6): p. 57-75.

40. Morgan, N.Y., S. English, W. Chen, V. Chernomordik, A. Russo, P.D. Smith, and A. Gandjbakhche, *Real Time in Vivo Non-Invasive Optical Imaging Using near-Infrared Fluorescent Quantum Dots.* Acad Radiol, 2005. 12(3): p. 313-23.

41. Hollman, K.W., S.Y. Emelianov, J.H. Neiss, G. Jotyan, G.J. Spooner, T. Juhasz, R.M. Kurtz, and M. O'Donnell, *Strain Imaging of Corneal Tissue with an Ultrasound Elasticity Microscope.* Cornea, 2002. 21(1): p. 68-73.

42. Tanter, M., D. Touboul, J.L. Gennisson, J. Bercoff, and M. Fink, *High-Resolution Quantitative Imaging of Cornea Elasticity Using Supersonic Shear Imaging.* IEEE Trans Med Imaging, 2009. 28(12): p. 1881-93.

43. Li, C., Z. Huang, and R.K. Wang, *Elastic Properties of Soft Tissue-Mimicking Phantoms Assessed by Combined Use of Laser Ultrasonics and Low Coherence Interferometry.* Opt Express, 2011. 19(11): p. 10153-63.

44. Litwiller, D.V., S.J. Lee, A. Kolipaka, Y.K. Mariappan, K.J. Glaser, J.S. Pulido, and R.L. Ehman, *Mr Elastography of the Ex Vivo Bovine Globe.* J Magn Reson Imaging, 2010. 32(1): p. 44-51.

45. Parker, K.J. and R.M. Lerner, *Sonoelasticity of Organs: Shear Waves Ring a Bell.* J Ultrasound Med, 1992. 11(8): p. 387-92.

46. Muthupillai, R., D.J. Lomas, P.J. Rossman, J.F. Greenleaf, A. Manduca, and R.L. Ehman, *Magnetic Resonance Elastography by Direct Visualization of Propagating Acoustic Strain Waves.* Science, 1995. 269(5232): p. 1854-7.

47. Nightingale, K., *Acoustic Radiation Force Impulse (Arfi) Imaging: A Review.* Curr Med Imaging Rev, 2011. 7(4): p. 328-339.

48. Grabner, G., R. Eilmsteiner, C. Steindl, J. Ruckhofer, R. Mattioli, and W. Husinsky, *Dynamic Corneal Imaging.* J Cataract Refract Surg, 2005. 31(1): p. 163-74.

49. Manduca, A., T.E. Oliphant, M.A. Dresner, J.L. Mahowald, S.A. Kruse, E. Amromin, J.P. Felmlee, J.F. Greenleaf, and R.L. Ehman, *Magnetic Resonance*

Elastography: Non-Invasive Mapping of Tissue Elasticity. Med Image Anal, 2001. 5(4): p. 237-54.

50. McCracken, P.J., A. Manduca, J. Felmlee, and R.L. Ehman, *Mechanical Transient-Based Magnetic Resonance Elastography.* Magn Reson Med, 2005. 53(3): p. 628-39.

51. Ophir, J., I. Cespedes, H. Ponnekanti, Y. Yazdi, and X. Li, *Elastography: A Quantitative Method for Imaging the Elasticity of Biological Tissues.* Ultrason Imaging, 1991. 13(2): p. 111-134.

52. D'Onofrio, M., A. Gallotti, and R.P. Mucelli, *Tissue Quantification with Acoustic Radiation Force Impulse Imaging: Measurement Repeatability and Normal Values in the Healthy Liver.* AJR Am J Roentgenol, 2010. 195(1): p. 132-6.

53. Zhang, X. and J.F. Greenleaf, *Estimation of Tissue's Elasticity with Surface Wave Speed.* J Acoust Soc Am, 2007. 122(5): p. 2522-5.

54. Tanter, M., J. Bercoff, A. Athanasiou, T. Deffieux, J.L. Gennisson, G. Montaldo, M. Muller, A. Tardivon, and M. Fink, *Quantitative Assessment of Breast Lesion Viscoelasticity: Initial Clinical Results Using Supersonic Shear Imaging.* Ultrasound Med Biol, 2008. 34(9): p. 1373-86.

55. Bercoff, J., M. Tanter, and M. Fink, *Supersonic Shear Imaging: A New Technique for Soft Tissue Elasticity Mapping.* IEEE Trans Ultrason Ferroelectr Freq Control, 2004. 51(4): p. 396-409.

56. Hernandez-Andrade, E., S.S. Hassan, H. Ahn, S.J. Korzeniewski, L. Yeo, T. Chaiworapongsa, and R. Romero, *Evaluation of Cervical Stiffness During Pregnancy*

Using Semiquantitative Ultrasound Elastography. Ultrasound Obstet Gynecol, 2013. 41(2): p. 152-61.

57. Venkatesh, S.K., M. Yin, and R.L. Ehman, *Magnetic Resonance Elastography of Liver: Technique, Analysis, and Clinical Applications.* J Magn Reson Imaging, 2013. 37(3): p. 544-55.

58. Mohan, K.D. and A.L. Oldenburg, *Elastography of Soft Materials and Tissues by Holographic Imaging of Surface Acoustic Waves.* Opt Express, 2012. 20(17): p. 18887-97.

59. Scarcelli, G. and S.H. Yun, *In Vivo Brillouin Optical Microscopy of the Human Eye.* Opt Express, 2012. 20(8): p. 9197-202.

60. Scarcelli, G., P. Kim, and S.H. Yun, *In Vivo Measurement of Age-Related Stiffening in the Crystalline Lens by Brillouin Optical Microscopy.* Biophys J, 2011. 101(6): p. 1539-45.

61. Vaughan, J.M. and J.T. Randall, *Brillouin Scattering, Density and Elastic Properties of the Lens and Cornea of the Eye.* Nature, 1980. 284(5755): p. 489-491.

62. Orssengo, G.J. and D.C. Pye, *Determination of the True Intraocular Pressure and Modulus of Elasticity of the Human Cornea in Vivo.* Bull Math Biol, 1999. 61(3): p. 551-72.

63. Saad, A., Y. Lteif, E. Azan, and D. Gatinel, *Biomechanical Properties of Keratoconus Suspect Eyes.* Invest Ophthalmol Vis Sci, 2010. 51(6): p. 2912-6.

64. Kotecha, A., *What Biomechanical Properties of the Cornea Are Relevant for the Clinician?* Surv Ophthalmol, 2007. 52 Suppl 2: p. S109-14.

65. Tao, C., Z. Han, Y. Sun, C. Zhou, C. Roberts, D. Zhou, and Q. Ren, *Corneal Hysteresis with Intraocular Pressure of a Wide Range: A Test on Porcine Eyes.* J Refract Surg, 2013. 29(12): p. 850-4.

66. Tian, L., M.W. Ko, L.K. Wang, J.Y. Zhang, T.J. Li, Y.F. Huang, and Y.P. Zheng, *Assessment of Ocular Biomechanics Using Dynamic Ultra High-Speed Scheimpflug Imaging in Keratoconic and Normal Eyes.* J Refract Surg, 2014. 30(11): p. 785-91.

67. Hallahan, K.M., A. Sinha Roy, R. Ambrosio, Jr., M. Salomao, and W.J. Dupps, Jr., *Discriminant Value of Custom Ocular Response Analyzer Waveform Derivatives in Keratoconus.* Ophthalmology, 2014. 121(2): p. 459-68.

68. Huang, D., E.A. Swanson, C.P. Lin, J.S. Schuman, W.G. Stinson, W. Chang, M.R. Hee, T. Flotte, K. Gregory, C.A. Puliafito, and James G. Fujimoto, *Optical Coherence Tomography.* Science, 1991. 254(5035): p. 1178-1181.

69. Bezerra, H.G., M.A. Costa, G. Guagliumi, A.M. Rollins, and D.I. Simon, *Intracoronary Optical Coherence Tomography: A Comprehensive Review Clinical and Research Applications.* JACC Cardiovasc Interv, 2009. 2(11): p. 1035-46.

70. Yang, V., M. Gordon, B. Qi, J. Pekar, S. Lo, E. Seng-Yue, A. Mok, B. Wilson, and I. Vitkin, *High Speed, Wide Velocity Dynamic Range Doppler Optical Coherence Tomography (Part I): System Design, Signal Processing, and Performance.* Opt Express, 2003. 11(7): p. 794-809.

71. Boppart, S.A., W. Luo, D.L. Marks, and K.W. Singletary, *Optical Coherence Tomography: Feasibility for Basic Research and Image-Guided Surgery of Breast Cancer.* Breast Cancer Res Treat, 2004. 84(2): p. 85-97.

72. Syed, S.H., K.V. Larin, M.E. Dickinson, and I.V. Larina, *Optical Coherence Tomography for High-Resolution Imaging of Mouse Development in Utero.* J Biomed Opt, 2011. 16(4): p. 046004.

73. Sun, C., B. Standish, and V.X. Yang, *Optical Coherence Elastography: Current Status and Future Applications.* J Biomed Opt, 2011. 16(4): p. 043001.

74. Welzel, J., *Optical Coherence Tomography in Dermatology: A Review.* Skin Res Technol, 2001. 7(1): p. 1-9.

75. Otis, L.L., M.J. Everett, U.S. Sathyam, and B.W. Colston, Jr., *Optical Coherence Tomography: A New Imaging Technology for Dentistry.* J Am Dent Assoc, 2000. 131(4): p. 511-4.

76. Fujimoto, J.G., C. Pitris, S.A. Boppart, and M.E. Brezinski, *Optical Coherence Tomography: An Emerging Technology for Biomedical Imaging and Optical Biopsy.* Neoplasia, 2000. 2(1-2): p. 9-25.

77. Yi, J., A.J. Radosevich, J.D. Rogers, S.C. Norris, I.R. Capoglu, A. Taflove, and V. Backman, *Can Oct Be Sensitive to Nanoscale Structural Alterations in Biological Tissue?* Opt Express, 2013. 21(7): p. 9043-59.

78. Zysk, A.M., F.T. Nguyen, A.L. Oldenburg, D.L. Marks, and S.A. Boppart, *Optical Coherence Tomography: A Review of Clinical Development from Bench to Bedside.* J Biomed Opt, 2007. 12(5): p. 051403.

79. Wei, X., A.K.S. Lau, Y. Xu, K.K. Tsia, and K.K.Y. Wong, *28 Mhz Swept Source at 1.0 Mm for Ultrafast Quantitative Phase Imaging.* Biomedical Optics Express, 2015. 6(10): p. 3855-3864.

80. Youngquist, R.C., S. Carr, and D.E. Davies, *Optical Coherence-Domain Reflectometry: A New Optical Evaluation Technique.* Opt Lett, 1987. 12(3): p. 158-60.

81. Fercher, A.F., W. Drexler, C.K. Hitzenberger, and T. Lasser, *Optical Coherence Tomography - Principles and Applications.* Reports on Progress in Physics, 2003. 66(2): p. 239.

82. Leitgeb, R., M. Wojtkowski, A. Kowalczyk, C.K. Hitzenberger, M. Sticker, and A.F. Fercher, *Spectral Measurement of Absorption by Spectroscopic Frequency-Domain Optical Coherence Tomography.* Opt Lett, 2000. 25(11): p. 820-2.

83. Wojtkowski, M., R. Leitgeb, A. Kowalczyk, T. Bajraszewski, and A.F. Fercher, *In Vivo Human Retinal Imaging by Fourier Domain Optical Coherence Tomography.* Journal of Biomedical Optics, 2002. 7(3): p. 457-463.

84. Choma, M., M. Sarunic, C. Yang, and J. Izatt, *Sensitivity Advantage of Swept Source and Fourier Domain Optical Coherence Tomography.* Opt Express, 2003. 11(18): p. 2183-9.

85. Izatt, J.A., M.A. Choma, and A.-H. Dhalla, *Theory of Optical Coherence Tomography*, in *Optical Coherence Tomography: Technology and Applications*, W. Drexler and G.J. Fujimoto, Editors. 2015, Springer International Publishing: Cham. p. 65-94.

86. Choma, M.A., A.K. Ellerbee, C. Yang, T.L. Creazzo, and J.A. Izatt, *Spectral-Domain Phase Microscopy.* Opt Lett, 2005. 30(10): p. 1162-4.

87. Zhao, Y., Z. Chen, C. Saxer, S. Xiang, J.F. de Boer, and J.S. Nelson, *Phase-Resolved Optical Coherence Tomography and Optical Doppler Tomography for*

Imaging Blood Flow in Human Skin with Fast Scanning Speed and High Velocity Sensitivity. Opt Lett, 2000. 25(2): p. 114-6.

88. Vakoc, B.J., R.M. Lanning, J.A. Tyrrell, T.P. Padera, L.A. Bartlett, T. Stylianopoulos, L.L. Munn, G.J. Tearney, D. Fukumura, R.K. Jain, and B.E. Bouma, *Three-Dimensional Microscopy of the Tumor Microenvironment in Vivo Using Optical Frequency Domain Imaging.* Nat Med, 2009. 15(10): p. 1219-23.

89. Fingler, J., R.J. Zawadzki, J.S. Werner, D. Schwartz, and S.E. Fraser, *Volumetric Microvascular Imaging of Human Retina Using Optical Coherence Tomography with a Novel Motion Contrast Technique.* Opt Express, 2009. 17(24): p. 22190-200.

90. Manapuram, R.K., S.R. Aglyamov, F.M. Monediado, M. Mashiatulla, J. Li, S.Y. Emelianov, and K.V. Larin, *In Vivo Estimation of Elastic Wave Parameters Using Phase-Stabilized Swept Source Optical Coherence Elastography.* J Biomed Opt, 2012. 17(10): p. 100501.

91. Manapuram, R.K., V.G.R. Manne, and K.V. Larin, *Development of Phase-Stabilized Swept-Source Oct for the Ultrasensitive Quantification of Microbubbles.* Laser Physics, 2008. 18(9): p. 1080-1086.

92. Manapuram, R.K., V.G.R. Manne, and K.V. Larin, *Phase-Sensitive Swept Source Optical Coherence Tomography for Imaging and Quantifying of Microbubbles in Clear and Scattering Media.* Journal of Applied Physics, 2009. 105(10): p. 102040.

93. Liang, X., V. Crecea, and S.A. Boppart, *Dynamic Optical Coherence Elastography: A Review.* J Innov Opt Health Sci, 2010. 3(4): p. 221-233.

94. Kennedy, B.F., T.R. Hillman, R.A. McLaughlin, B.C. Quirk, and D.D. Sampson, *In Vivo Dynamic Optical Coherence Elastography Using a Ring Actuator*. Opt Express, 2009. 17(24): p. 21762-72.

95. Kennedy, B.F., M. Wojtkowski, M. Szkulmowski, K.M. Kennedy, K. Karnowski, and D.D. Sampson, *Improved Measurement of Vibration Amplitude in Dynamic Optical Coherence Elastography*. Biomed Opt Express, 2012. 3(12): p. 3138-52.

96. Ford, M.R., W.J. Dupps, Jr., A.M. Rollins, A.S. Roy, and Z. Hu, *Method for Optical Coherence Elastography of the Cornea.* J Biomed Opt, 2011. 16(1): p. 016005.

97. Schmitt, J., *Oct Elastography: Imaging Microscopic Deformation and Strain of Tissue.* Opt Express, 1998. 3(6): p. 199-211.

98. Wang, R.K., S. Kirkpatrick, and M. Hinds, *Phase-Sensitive Optical Coherence Elastography for Mapping Tissue Microstrains in Real Time.* Applied Physics Letters, 2007. 90(16): p. 164105.

99. De la Torre-Ibarra, M.H., P.D. Ruiz, and J.M. Huntley, *Double-Shot Depth-Resolved Displacement Field Measurement Using Phase-Contrast Spectral Optical Coherence Tomography.* Opt Express, 2006. 14(21): p. 9643-56.

100. Wang, S., J. Li, R.K. Manapuram, F.M. Menodiado, D.R. Ingram, M.D. Twa, A.J. Lazar, D.C. Lev, R.E. Pollock, and K.V. Larin, *Noncontact Measurement of Elasticity for the Detection of Soft-Tissue Tumors Using Phase-Sensitive Optical Coherence Tomography Combined with a Focused Air-Puff System.* Opt Lett, 2012. 37(24): p. 5184-6.

101. Li, C., G. Guan, Z. Huang, M. Johnstone, and R.K. Wang, *Noncontact All-Optical Measurement of Corneal Elasticity.* Opt Lett, 2012. 37(10): p. 1625-7.

102. Manapuram, R.K., S. Aglyamov, F.M. Menodiado, M. Mashiatulla, S. Wang, S.A. Baranov, J.S. Li, S. Emelianov, and K.V. Larin, *Estimation of Shear Wave Velocity in Gelatin Phantoms Utilizing Phs-Ssoct.* Laser Phys, 2012. 22(9): p. 1439-1444.

103. Liang, X., M. Orescanin, K.S. Toohey, M.F. Insana, and S.A. Boppart, *Acoustomotive Optical Coherence Elastography for Measuring Material Mechanical Properties.* Opt Lett, 2009. 34(19): p. 2894-6.

104. Razani, M., A. Mariampillai, C. Sun, T.W. Luk, V.X. Yang, and M.C. Kolios, *Feasibility of Optical Coherence Elastography Measurements of Shear Wave Propagation in Homogeneous Tissue Equivalent Phantoms.* Biomed Opt Express, 2012. 3(5): p. 972-80.

105. Sticker, M., C.K. Hitzenberger, R. Leitgeb, and A.F. Fercher, *Quantitative Differential Phase Measurement and Imaging in Transparent and Turbid Media by Optical Coherence Tomography.* Opt Lett, 2001. 26(8): p. 518-520.

106. Liang, X. and S.A. Boppart, *Biomechanical Properties of in Vivo Human Skin from Dynamic Optical Coherence Elastography.* IEEE Trans Biomed Eng, 2010. 57(4): p. 953-9.

107. Ford, M.R., A. Sinha Roy, A.M. Rollins, and W.J. Dupps, Jr., *Serial Biomechanical Comparison of Edematous, Normal, and Collagen Crosslinked Human Donor Corneas Using Optical Coherence Elastography.* J Cataract Refract Surg, 2014. 40(6): p. 1041-7.

108. Kennedy, B.F., S.H. Koh, R.A. McLaughlin, K.M. Kennedy, P.R.T. Munro, and D.D. Sampson, *Strain Estimation in Phase-Sensitive Optical Coherence Elastography.* Biomedical Optics Express, 2012. 3(8): p. 1865-1879.

109. Oldenburg, A.L. and S.A. Boppart, *Resonant Acoustic Spectroscopy of Soft Tissues Using Embedded Magnetomotive Nanotransducers and Optical Coherence Tomography.* Phys Med Biol, 2010. 55(4): p. 1189-201.

110. Akca, B.I., E.W. Chang, S. Kling, A. Ramier, G. Scarcelli, S. Marcos, and S.H. Yun, *Observation of Sound-Induced Corneal Vibrational Modes by Optical Coherence Tomography.* Biomed Opt Express, 2015. 6(9): p. 3313-9.

111. Chang, E.W., J.B. Kobler, and S.H. Yun, *Sub-Nanometer Optical Coherence Tomographic Vibrography.* Optics letters, 2012. 37(17): p. 3678-3680.

112. Qu, Y., T. Ma, Y. He, J. Zhu, C. Dai, M. Yu, S. Huang, F. Lu, K.K. Shung, Q. Zhou, and Z. Chen, *Acoustic Radiation Force Optical Coherence Elastography of Corneal Tissue.* IEEE Journal of Selected Topics in Quantum Electronics, 2016. PP(99): p. 1-1.

113. Li, J., S. Wang, R.K. Manapuram, M. Singh, F.M. Menodiado, S. Aglyamov, S. Emelianov, M.D. Twa, and K.V. Larin, *Dynamic Optical Coherence Tomography Measurements of Elastic Wave Propagation in Tissue-Mimicking Phantoms and Mouse Cornea in Vivo.* J Biomed Opt, 2013. 18(12): p. 121503.

114. Li, J., S. Wang, M. Singh, S. Aglyamov, S. Emelianov, M.D. Twa, and K.V. Larin, *Air-Pulse Oce for Assessment of Age-Related Changes in Mouse Cornea in Vivo.* Laser Phys Lett, 2014. 11(6): p. 065601.

115. Wang, S. and K.V. Larin, *Noncontact Depth-Resolved Micro-Scale Optical Coherence Elastography of the Cornea.* Biomed Opt Express, 2014. 5(11): p. 3807-21.

116. Wang, S. and K.V. Larin, *Shear Wave Imaging Optical Coherence Tomography (Swi-Oct) for Ocular Tissue Biomechanics.* Opt Lett, 2014. 39(1): p. 41-4.

117. Song, S., B.-Y. Hsieh, W. Wei, T. Shen, I. Pelivanov, M. O'Donnell, and R.K. Wang. *Optical Coherence Elastography Based on High Speed Imaging of Singles-Hot Laser-Induced Acoustic Waves at 16 Khz Frame Rate*. 2016.

118. Wang, S., K.V. Larin, J. Li, S. Vantipalli, R.K. Manapuram, S. Aglyamov, S. Emelianov, and M.D. Twa, *A Focused Air-Pulse System for Optical-Coherence-Tomography-Based Measurements of Tissue Elasticity.* Laser Phy Lett, 2013. 10(7): p. 075605.

119. Hall, T.J., M. Bilgen, M.F. Insana, and T.A. Krouskop, *Phantom Materials for Elastography.* IEEE Transactions on Ultrasonics, Ferroelectrics, and Frequency Control, 1997. 44(6): p. 1355-1365.

120. Doyle, J.F., *Wave Propagation in Structures: Spectral Analysis Using Fast Discrete Fourier Transforms* 2nd, ed. 1997, New York: Springer-Verlag.

121. Zhang, X., B. Qiang, and J. Greenleaf, *Comparison of the Surface Wave Method and the Indentation Method for Measuring the Elasticity of Gelatin Phantoms of Different Concentrations.* Ultrasonics, 2011. 51(2): p. 157-64.

122. Han, Z., J. Li, M. Singh, C. Wu, C.H. Liu, S. Wang, R. Idugboe, R. Raghunathan, N. Sudheendran, S.R. Aglyamov, M.D. Twa, and K.V. Larin, *Quantitative Methods for Reconstructing Tissue Biomechanical Properties in Optical*

Coherence Elastography: A Comparison Study. Phys Med Biol, 2015. 60(9): p. 3531-47.

123. Randleman, J.B., M. Woodward, M.J. Lynn, and R.D. Stulting, *Risk Assessment for Ectasia after Corneal Refractive Surgery.* Ophthalmology, 2008. 115(1): p. 37-50.

124. Wagner, H., J.T. Barr, and K. Zadnik, *Collaborative Longitudinal Evaluation of Keratoconus (Clek) Study: Methods and Findings to Date.* Cont Lens Anterior Eye, 2007. 30(4): p. 223-32.

125. Ertan, A. and O. Muftuoglu, *Keratoconus Clinical Findings According to Different Age and Gender Groups.* Cornea, 2008. 27(10): p. 1109-13.

126. Elsheikh, A., D. Wang, M. Brown, P. Rama, M. Campanelli, and D. Pye, *Assessment of Corneal Biomechanical Properties and Their Variation with Age.* Curr Eye Res, 2007. 32(1): p. 11-9.

127. Ytteborg, J., *Further Investigations of Factors Influencing Size of Rigidity Coefficient.* Acta Ophthalmol (Copenh), 1960. 38: p. 643-57.

128. Pallikaris, I.G., G.D. Kymionis, H.S. Ginis, G.A. Kounis, and M.K. Tsilimbaris, *Ocular Rigidity in Living Human Eyes.* Invest Ophthalmol Vis Sci, 2005. 46(2): p. 409-14.

129. Randleman, J.B., D.G. Dawson, H.E. Grossniklaus, B.E. McCarey, and H.F. Edelhauser, *Depth-Dependent Cohesive Tensile Strength in Human Donor Corneas: Implications for Refractive Surgery.* J Refract Surg, 2008. 24(1): p. S85-9.

130. Dorronsoro, C., D. Pascual, P. Perez-Merino, S. Kling, and S. Marcos, *Dynamic Oct Measurement of Corneal Deformation by an Air Puff in Normal and Cross-Linked Corneas.* Biomed Opt Express, 2012. 3(3): p. 473-87.

131. Alonso-Caneiro, D., K. Karnowski, B.J. Kaluzny, A. Kowalczyk, and M. Wojtkowski, *Assessment of Corneal Dynamics with High-Speed Swept Source Optical Coherence Tomography Combined with an Air Puff System.* Opt Express, 2011. 19(15): p. 14188-99.

132. Sarvazyan, A.P., O.V. Rudenko, S.D. Swanson, J.B. Fowlkes, and S.Y. Emelianov, *Shear Wave Elasticity Imaging: A New Ultrasonic Technology of Medical Diagnostics.* Ultrasound Med Biol, 1998. 24(9): p. 1419-35.

133. Wollensak, G., E. Spoerl, and T. Seiler, *Riboflavin/Ultraviolet-a-Induced Collagen Crosslinking for the Treatment of Keratoconus.* Am J Ophthalmol, 2003. 135(5): p. 620-7.

134. O'Brart, D.P.S., *Corneal Collagen Cross-Linking: A Review.* J Optom, 2014. 7(3): p. 113-24.

135. Kotecha, A., R.A. Russell, A. Sinapis, S. Pourjavan, D. Sinapis, and D.F. Garway-Heath, *Biomechanical Parameters of the Cornea Measured with the Ocular Response Analyzer in Normal Eyes.* BMC Ophthalmol, 2014. 14: p. 11.

136. Han, Z., C. Tao, D. Zhou, Y. Sun, C. Zhou, Q. Ren, and C.J. Roberts, *Air Puff Induced Corneal Vibrations: Theoretical Simulations and Clinical Observations.* J Refract Surg, 2014. 30(3): p. 208-213.

137. Shah, S., M. Laiquzzaman, R. Bhojwani, S. Mantry, and I. Cunliffe, *Assessment of the Biomechanical Properties of the Cornea with the Ocular Response Analyzer in Normal and Keratoconic Eyes.* Invest Ophthalmol Vis Sci, 2007. 48(7): p. 3026-31.

138. Bak-Nielsen, S., I.B. Pedersen, A. Ivarsen, and J. Hjortdal, *Dynamic Scheimpflug-Based Assessment of Keratoconus and the Effects of Corneal Cross-Linking.* J Refract Surg, 2014. 30(6): p. 408-14.

139. Gkika, M., G. Labiris, A. Giarmoukakis, A. Koutsogianni, and V. Kozobolis, *Evaluation of Corneal Hysteresis and Corneal Resistance Factor after Corneal Cross-Linking for Keratoconus.* Graefes Arch Clin Exp Ophthalmol, 2012. 250(4): p. 565-73.

140. Greenstein, S.A., K.L. Fry, and P.S. Hersh, *In Vivo Biomechanical Changes after Corneal Collagen Cross-Linking for Keratoconus and Corneal Ectasia: 1-Year Analysis of a Randomized, Controlled, Clinical Trial.* Cornea, 2012. 31(1): p. 21-5.

141. Goldich, Y., Y. Barkana, Y. Morad, M. Hartstein, I. Avni, and D. Zadok, *Can We Measure Corneal Biomechanical Changes after Collagen Cross-Linking in Eyes with Keratoconus?--a Pilot Study.* Cornea, 2009. 28(5): p. 498-502.

142. Nguyen, T.M., J.F. Aubry, M. Fink, J. Bercoff, and M. Tanter, *In Vivo Evidence of Porcine Cornea Anisotropy Using Supersonic Shear Wave Imaging.* Invest Ophthalmol Vis Sci, 2014. 55(11): p. 7545-52.

143. Elsheikh, A., M. Brown, D. Alhasso, P. Rama, M. Campanelli, and D. Garway-Heath, *Experimental Assessment of Corneal Anisotropy.* J Refract Surg, 2008. 24(2): p. 178-87.

144. Pinsky, P.M., D. van der Heide, and D. Chernyak, *Computational Modeling of Mechanical Anisotropy in the Cornea and Sclera.* J Cataract Refract Surg, 2005. 31(1): p. 136-145.

145. Meek, K.M. and C. Boote, *The Use of X-Ray Scattering Techniques to Quantify the Orientation and Distribution of Collagen in the Corneal Stroma.* Prog Retin Eye Res, 2009. 28(5): p. 369-92.

146. Hjortdal, J.O., *Regional Elastic Performance of the Human Cornea.* J Biomech, 1996. 29(7): p. 931-42.

147. Armstrong, B.K., M.P. Lin, M.R. Ford, M.R. Santhiago, V. Singh, G.H. Grossman, V. Agrawal, A.S. Roy, R.S. Butler, W.J. Dupps, and S.E. Wilson, *Biological and Biomechanical Responses to Traditional Epithelium-Off and Transepithelial Riboflavin-Uva Cxl Techniques in Rabbits.* J Refract Surg, 2013. 29(5): p. 332-41.

148. Torricelli, A.A., M.R. Ford, V. Singh, M.R. Santhiago, W.J. Dupps, Jr., and S.E. Wilson, *Bac-Edta Transepithelial Riboflavin-Uva Crosslinking Has Greater Biomechanical Stiffening Effect Than Standard Epithelium-Off in Rabbit Corneas.* Exp Eye Res, 2014. 125: p. 114-7.

149. Seiler, T.G., I. Fischinger, T. Koller, D. Zapp, B.E. Frueh, and T. Seiler, *Customized Corneal Crosslinking- One Year Results.* Am J Ophthalmol, 2016.

150. Crecea, V., A.L. Oldenburg, X. Liang, T.S. Ralston, and S.A. Boppart, *Magnetomotive Nanoparticle Transducers for Optical Rheology of Viscoelastic Materials.* Opt Express, 2009. 17(25): p. 23114-22.

151. Wu, C., Z. Han, S. Wang, J. Li, M. Singh, C.H. Liu, S. Aglyamov, S. Emelianov, F. Manns, and K.V. Larin, *Assessing Age-Related Changes in the Biomechanical Properties of Rabbit Lens Using a Coaligned Ultrasound and Optical Coherence Elastography System.* Invest Ophthalmol Vis Sci, 2015. 56(2): p. 1292-300.

152. Li, J., Z. Han, M. Singh, M.D. Twa, and K.V. Larin, *Differentiating Untreated and Cross-Linked Porcine Corneas of the Same Measured Stiffness with Optical Coherence Elastography.* J Biomed Opt, 2014. 19(11): p. 110502.

153. Twa, M.D., J. Li, S. Vantipalli, M. Singh, S. Aglyamov, S. Emelianov, and K.V. Larin, *Spatial Characterization of Corneal Biomechanical Properties with Optical Coherence Elastography after Uv Cross-Linking.* Biomed Opt Express, 2014. 5(5): p. 1419-27.

154. Han, Z., J. Li, M. Singh, S.R. Aglyamov, C. Wu, C. Liu, and K.V. Larin, *Analysis of the Effects of Curvature and Thickness on Elastic Wave Velocity in Cornea-Like Structures by Finite Element Modeling and Optical Coherence Elastography.* Appl Phys Lett, 2015. 106(23): p. 233702.

155. Palko, J.R., J. Tang, B.C. Perez, X. Pan, and J. Liu, *Spatially Heterogeneous Corneal Mechanical Responses before and after Riboflavin–Ultraviolet-a Crosslinking.* J Cataract Refract Surg, 2014. 40(6): p. 1021-1031.

156. Seifert, J., C.M. Hammer, J. Rheinlaender, S. Sel, M. Scholz, F. Paulsen, and T.E. Schaffer, *Distribution of Young's Modulus in Porcine Corneas after Riboflavin/Uva-Induced Collagen Cross-Linking as Measured by Atomic Force Microscopy.* PLoS One, 2014. 9(1): p. e88186.

157. Scarcelli, G., S. Kling, E. Quijano, R. Pineda, S. Marcos, and S.H. Yun, *Brillouin Microscopy of Collagen Crosslinking: Noncontact Depth-Dependent Analysis of Corneal Elastic Modulus.* Invest Ophthalmol Vis Sci, 2013. 54(2): p. 1418-1425.

158. Beshtawi, I.M., R. Akhtar, M.C. Hillarby, C. O'Donnell, X. Zhao, A. Brahma, F. Carley, B. Derby, and H. Radhakrishnan, *Biomechanical Changes of Collagen Cross-Linking on Human Keratoconic Corneas Using Scanning Acoustic Microscopy.* Curr Eye Res, 2015: p. 1-7.

159. Aglyamov, S.R., S. Wang, A.B. Karpiouk, J. Li, M. Twa, S.Y. Emelianov, and K.V. Larin, *The Dynamic Deformation of a Layered Viscoelastic Medium under Surface Excitation.* Phys Med Biol, 2015. 60(11): p. 4295-312.

160. Singh, M., C. Wu, C.H. Liu, J. Li, A. Schill, A. Nair, and K.V. Larin, *Phase-Sensitive Optical Coherence Elastography at 1.5 Million a-Lines Per Second.* Opt Lett, 2015. 40(11): p. 2588-91.

161. Kling, S., N. Bekesi, C. Dorronsoro, D. Pascual, and S. Marcos, *Corneal Viscoelastic Properties from Finite-Element Analysis of in Vivo Air-Puff Deformation.* PLoS One, 2014. 9(8): p. e104904.

162. Elsheikh, A., D.F. Wang, M. Brown, P. Rama, M. Campanelli, and D. Pye, *Assessment of Corneal Biomechanical Properties and Their Variation with Age.* Current Eye Research, 2007. 32(1): p. 11-19.

163. Cherfan, D., E.E. Verter, S. Melki, T.E. Gisel, F.J. Doyle, Jr., G. Scarcelli, S.H. Yun, R.W. Redmond, and I.E. Kochevar, *Collagen Cross-Linking Using Rose Bengal and Green Light to Increase Corneal Stiffness.* Invest Ophthalmol Vis Sci, 2013. 54(5): p. 3426-33.

164. Wollensak, G., E. Spoerl, and T. Seiler, *Stress-Strain Measurements of Human and Porcine Corneas after Riboflavin-Ultraviolet-a-Induced Cross-Linking.* J Cataract Refract Surg, 2003. 29(9): p. 1780-5.

165. Nguyen, T.M., J.F. Aubry, D. Touboul, M. Fink, J.L. Gennisson, J. Bercoff, and M. Tanter, *Monitoring of Cornea Elastic Properties Changes During Uv-a/Riboflavin-Induced Corneal Collagen Cross-Linking Using Supersonic Shear Wave Imaging: A Pilot Study.* Invest Ophthalmol Vis Sci, 2012. 53(9): p. 5948-54.

166. Thomasy, S.M., V.K. Raghunathan, M. Winkler, C.M. Reilly, A.R. Sadeli, P. Russell, J.V. Jester, and C.J. Murphy, *Elastic Modulus and Collagen Organization of the Rabbit Cornea: Epithelium to Endothelium.* Acta Biomater, 2014. 10(2): p. 785-91.

167. Wollensak, G. and E. Iomdina, *Long-Term Biomechanical Properties of Rabbit Cornea after Photodynamic Collagen Crosslinking.* Acta Ophthalmol, 2009. 87(1): p. 48-51.

168. Nguyen, T.M., S. Song, B. Arnal, Z. Huang, M. O'Donnell, and R.K. Wang, *Visualizing Ultrasonically Induced Shear Wave Propagation Using Phase-Sensitive Optical Coherence Tomography for Dynamic Elastography.* Opt Lett, 2014. 39(4): p. 838-41.

169. Song, S., Z. Huang, and R.K. Wang, *Tracking Mechanical Wave Propagation within Tissue Using Phase-Sensitive Optical Coherence Tomography: Motion Artifact and Its Compensation.* J Biomed Opt, 2013. 18(12): p. 121505.

170. Aglyamov, S., A. Skovoroda, H. Xie, K. Kim, J. Rubin, M. O'Donnell, W.W. T, D. Myers, and S. Emelianov, *Model-Based Reconstructive Elasticity Imaging Using Ultrasound.* Int J Biomed Imaging, 2007. 2007: p. 35830.

171. Zell, K., J.I. Sperl, M.W. Vogel, R. Niessner, and C. Haisch, *Acoustical Properties of Selected Tissue Phantom Materials for Ultrasound Imaging.* Phys Med Biol, 2007. 52(20): p. N475-84.

172. Kampmeier, J., B. Radt, R. Birngruber, and R. Brinkmann, *Thermal and Biomechanical Parameters of Porcine Cornea.* Cornea, 2000. 19(3): p. 355-63.

173. Haigis, W., *Corneal Power after Refractive Surgery for Myopia: Contact Lens Method.* J Cataract Refract Surg, 2003. 29(7): p. 1397-411.

174. Kling, S., L. Remon, A. Perez-Escudero, J. Merayo-Lloves, and S. Marcos, *Corneal Biomechanical Changes after Collagen Cross-Linking from Porcine Eye Inflation Experiments.* Invest Ophthalmol Vis Sci, 2010. 51(8): p. 3961-8.

175. Kling, S., I.B. Akca, E.W. Chang, G. Scarcelli, N. Bekesi, S.H. Yun, and S. Marcos, *Numerical Model of Optical Coherence Tomographic Vibrography Imaging to Estimate Corneal Biomechanical Properties.* J R Soc Interface, 2014. 11(101): p. 20140920.

176. Holopainen, J.M. and K. Krootila, *Transient Corneal Thinning in Eyes Undergoing Corneal Cross-Linking.* Am J Ophthalmol, 2011. 152(4): p. 533-6.

177. Greenstein, S.A., V.P. Shah, K.L. Fry, and P.S. Hersh, *Corneal Thickness Changes after Corneal Collagen Crosslinking for Keratoconus and Corneal Ectasia: One-Year Results.* J Cataract Refract Surg, 2011. 37(4): p. 691-700.

178. Vinciguerra, P., E. Albe, S. Trazza, P. Rosetta, R. Vinciguerra, T. Seiler, and D. Epstein, *Refractive, Topographic, Tomographic, and Aberrometric Analysis of Keratoconic Eyes Undergoing Corneal Cross-Linking.* Ophthalmology, 2009. 116(3): p. 369-78.

179. Elsheikh, A., D. Alhasso, and P. Rama, *Biomechanical Properties of Human and Porcine Corneas.* Exp Eye Res, 2008. 86(5): p. 783-90.

180. Graff, K.F., *Wave Motion in Elastic Solids*. 1975: Courier Corporation, London.

181. Nenadic, I.Z., M.W. Urban, S. Aristizabal, S.A. Mitchell, T.C. Humphrey, and J.F. Greenleaf, *On Lamb and Rayleigh Wave Convergence in Viscoelastic Tissues.* Phys Med Biol, 2011. 56(20): p. 6723-38.

182. Han, Z., X. Sui, D. Zhou, C. Zhou, and Q. Ren, *Biomechanical and Refractive Behaviors of Keratoconic Cornea Based on Three-Dimensional Anisotropic Hyperelastic Models.* J Refract Surg, 2013. 29(4): p. 282-90.

183. Nguyen, T.M., S. Song, B. Arnal, E.Y. Wong, Z. Huang, R.K. Wang, and M. O'Donnell, *Shear Wave Pulse Compression for Dynamic Elastography Using Phase-Sensitive Optical Coherence Tomography.* J Biomed Opt, 2014. 19(1): p. 16013.

184. Elsheikh, A. and D. Alhasso, *Mechanical Anisotropy of Porcine Cornea and Correlation with Stromal Microstructure.* Exp Eye Res, 2009. 88(6): p. 1084-91.

185. Wang, S., S. Aglyamov, A. Karpiouk, J. Li, S. Emelianov, F. Manns, and K.V. Larin, *Assessing the Mechanical Properties of Tissue-Mimicking Phantoms at Different Depths as an Approach to Measure Biomechanical Gradient of Crystalline Lens.* Biomed Opt Express, 2013. 4(12): p. 2769-80.

186. Aglyamov, S., S. Wang, A. Karpiouk, J. Li, S. Emelianov, and K.V. Larin. *Model-Based Optical Coherence Elastography Using Acoustic Radiation Force*. in *SPIE Proc*. 2014.

187. Liu, J. and X. He, *Corneal Stiffness Affects Iop Elevation During Rapid Volume Change in the Eye.* Invest Ophthalmol Vis Sci, 2009. 50(5): p. 2224-9.

188. Medeiros, F.A. and R.N. Weinreb, *Evaluation of the Influence of Corneal Biomechanical Properties on Intraocular Pressure Measurements Using the Ocular Response Analyzer.* J Glaucoma, 2006. 15(5): p. 364-70.

189. Singh, S.S., H.B. Bohidar, and S. Bandyopadhyay, *Study of Gelatin-Agar Intermolecular Aggregates in the Supernatant of Its Coacervate.* Colloids Surf B Biointerfaces, 2007. 57(1): p. 29-36.

190. Tao, C., Y. Sun, C. Zhou, Z. Han, and Q. Ren, *Effects of Collagen Cross-Linking on the Interlamellar Cohesive Strength of Porcine Cornea.* Cornea, 2013. 32(2): p. 169-73.

191. Meek, K.M., S.J. Tuft, Y. Huang, P.S. Gill, S. Hayes, R.H. Newton, and A.J. Bron, *Changes in Collagen Orientation and Distribution in Keratoconus Corneas.* Invest Ophthalmol Vis Sci, 2005. 46(6): p. 1948-56.

192. Meek, K.M., T. Blamires, G.F. Elliott, T.J. Gyi, and C. Nave, *The Organisation of Collagen Fibrils in the Human Corneal Stroma: A Synchrotron X-Ray Diffraction Study.* Curr Eye Res, 1987. 6(7): p. 841-6.

193. Komai, Y. and T. Ushiki, *The Three-Dimensional Organization of Collagen Fibrils in the Human Cornea and Sclera.* Invest Ophthalmol Vis Sci, 1991. 32(8): p. 2244-58.

194. Jalbert, I., F. Stapleton, E. Papas, D.F. Sweeney, and M. Coroneo, *In Vivo Confocal Microscopy of the Human Cornea.* The British Journal of Ophthalmology, 2003. 87(2): p. 225-236.

195. Han, M., G. Giese, and J. Bille, *Second Harmonic Generation Imaging of Collagen Fibrils in Cornea and Sclera.* Opt Express, 2005. 13(15): p. 5791-7.

196. Ducros, M.G., J.F. de Boer, H. Huai-En, L.C. Chao, C. Zhongping, J.S. Nelson, T.E. Milner, and H. Rylander, III, *Polarization Sensitive Optical Coherence*

Tomography of the Rabbit Eye. Selected Topics in Quantum Electronics, IEEE Journal of, 1999. 5(4): p. 1159-1167.

197. Latour, G., I. Gusachenko, L. Kowalczuk, I. Lamarre, and M.C. Schanne-Klein, *In Vivo Structural Imaging of the Cornea by Polarization-Resolved Second Harmonic Microscopy.* Biomed Opt Express, 2012. 3(1): p. 1-15.

198. Gotzinger, E., M. Pircher, M. Sticker, A.F. Fercher, and C.K. Hitzenberger, *Measurement and Imaging of Birefringent Properties of the Human Cornea with Phase-Resolved, Polarization-Sensitive Optical Coherence Tomography.* J Biomed Opt, 2004. 9(1): p. 94-102.

199. Drexler, W. and J.G. Fujimoto, *Optical Coherence Tomography in Ophthalmology.* J Biomed Opt, 2007. 12(4): p. 041201-041201-2.

200. Nguyen, T.D. and B.L. Boyce, *An Inverse Finite Element Method for Determining the Anisotropic Properties of the Cornea.* Biomech Model Mechanobiol, 2011. 10(3): p. 323-37.

201. Lankford, W., S. Snyder, and J. Bauscher, *New Criteria for Predicting the Press Performance of Deep Drawing Sheets.* Trans. ASM, 1950. 42: p. 1197-1232.

202. Drexler, W., M. Liu, A. Kumar, T. Kamali, A. Unterhuber, and R.A. Leitgeb, *Optical Coherence Tomography Today: Speed, Contrast, and Multimodality.* J Biomed Opt, 2014. 19(7): p. 071412.

203. Kirk, R.W., B.F. Kennedy, D.D. Sampson, and R.A. McLaughlin, *Near Video-Rate Optical Coherence Elastography by Acceleration with a Graphics Processing Unit.* Journal of Lightwave Technology, 2015. 33(16): p. 3481-3485.

204. Han, Z., S.R. Aglyamov, J. Li, M. Singh, S. Wang, S. Vantipalli, C. Wu, C.H. Liu, M.D. Twa, and K.V. Larin, *Quantitative Assessment of Corneal Viscoelasticity Using Optical Coherence Elastography and a Modified Rayleigh-Lamb Equation.* J Biomed Opt, 2015. 20(2): p. 20501.

205. Wang, S. and K.V. Larin, *Optical Coherence Elastography for Tissue Characterization: A Review.* J Biophotonics, 2014. 9999(9999).

206. Drain, L., *The Laser Doppler Technique, 1980.* John Wiley, Chichester. 1084: p. 186-194.

207. Castellini, P., G. Revel, and E. Tomasini, *Laser Doppler Vibrometry: A Review of Advances and Applications.* Shock Vib Dig, 1998. 30(6): p. 443-456.

208. Ball, G.R., A. Huber, and R.L. Goode, *Scanning Laser Doppler Vibrometry of the Middle Ear Ossicles.* Ear Nose Throat J, 1997. 76(4): p. 213-8, 220, 222.

209. Sokolowski, J., K. Niemczyk, R. Bartoszewicz, K. Morawski, A. Bruzgielewicz, and B. Rygalska, *Round Window's Movability Measurements with Helping of Ldv in Evaluation of Ossicular Chain Functioning.* Otolaryngol Pol, 2010. 64(7): p. 77-80.

210. Felver, B., D.C. King, S.C. Lea, G.J. Price, and A. Damien Walmsley, *Cavitation Occurrence around Ultrasonic Dental Scalers.* Ultrason Sonochem, 2009. 16(5): p. 692-7.

211. Lea, S.C., A.D. Walmsley, P.J. Lumley, and G. Landini, *A New Insight into the Oscillation Characteristics of Endosonic Files Used in Dentistry.* Phys Med Biol, 2004. 49(10): p. 2095-102.

212. De Melis, M., U. Morbiducci, and L. Scalise, *Identification of Cardiac Events by Optical Vibrocardiograpy: Comparison with Phonocardiography.* Conf Proc IEEE Eng Med Biol Soc, 2007. 2007: p. 2956-9.

213. Morbiducci, U., L. Scalise, M. De Melis, and M. Grigioni, *Optical Vibrocardiography: A Novel Tool for the Optical Monitoring of Cardiac Activity.* Ann Biomed Eng, 2007. 35(1): p. 45-58.

214. Scalise, L. and U. Morbiducci, *Non-Contact Cardiac Monitoring from Carotid Artery Using Optical Vibrocardiography.* Med Eng Phys, 2008. 30(4): p. 490-7.

215. Rixen, D.J. and T. Schuurman, *In Vivo Measurement of the Human Thorax and Abdomen Surface Using Laser Vibrometry: A New Diagnostic Tool?*, in *Topics in Modal Analysis Ii, Volume 6: Proceedings of the 30th Imac, a Conference on Structural Dynamics, 2012*, R. Allemang, et al., Editors. 2012, Springer New York: New York, NY. p. 235-245.

216. Yazicioglu, Y., T.J. Royston, T. Spohnholtz, B. Martin, F. Loth, and H.S. Bassiouny, *Acoustic Radiation from a Fluid-Filled, Subsurface Vascular Tube with Internal Turbulent Flow Due to a Constriction.* J Acoust Soc Am, 2005. 118(2): p. 1193-209.

217. De Melis, M., U. Morbiducci, L. Scalise, E.P. Tomasini, D. Delbeke, R. Baets, L.M. Van Bortel, and P. Segers, *A Noncontact Approach for the Evaluation of Large Artery Stiffness: A Preliminary Study.* Am J Hypertens, 2008. 21(12): p. 1280-3.

218. Dahl, M.C., P.A. Kramer, P.G. Reinhall, S.K. Benirschke, S.T. Hansen, and R.P. Ching, *The Efficacy of Using Vibrometry to Detect Osteointegration of the Agility Total Ankle.* J Biomech, 2010. 43(9): p. 1840-3.

219. Castellini, P., R. Huebner, and M. Pinotti. *Vibration Measurement on Artificial Heart Valve by Laser Doppler Vibrometry*. 2002.

220. Rondini, C., G. Rossi, and L. Scalise, *Laser Vibrometry and Stress Measurement by Thermoelasticity on Mechanical Heart Valve*. Proceedings of Spie - the International Society for Optical Engineering. 2004, Bellingham, Wash., USA: SPIE - The International Society of Optical Engineering.

221. Wang, S., A.L. Lopez, 3rd, Y. Morikawa, G. Tao, J. Li, I.V. Larina, J.F. Martin, and K.V. Larin, *Noncontact Quantitative Biomechanical Characterization of Cardiac Muscle Using Shear Wave Imaging Optical Coherence Tomography.* Biomed Opt Express, 2014. 5(7): p. 1980-92.

222. Skovoroda, A.R., S.Y. Emelianov, and M.O. Donnell, *Tissue Elasticity Reconstruction Based on Ultrasonic Displacement and Strain Images.* IEEE Transactions on Ultrasonics, Ferroelectrics, and Frequency Control, 1995. 42(4): p. 747-765.

223. Kennedy, K.M., L. Chin, R.A. McLaughlin, B. Latham, C.M. Saunders, D.D. Sampson, and B.F. Kennedy, *Quantitative Micro-Elastography: Imaging of Tissue Elasticity Using Compression Optical Coherence Elastography.* Sci Rep, 2015. 5: p. 15538.

First Author Journal Publications

1. **Jiasong Li**, Shang Wang, Ravi Kiran Manapuram, Manmohan Singh, Floredes M Menodiado, Salavat Aglyamov, Stanislav Emelianov, Michael D Twa and Kirill V Larin, "*Dynamic optical coherence tomography measurements of elastic wave propagation in tissue-mimicking phantoms and mouse cornea in vivo*", Journal of Biomedical Optics, 2013 Dec;18(12):121503.

2. **Jiasong Li**, Shang Wang, Manmohan Singh, Salavat Aglyamov, Stanislav Emelianov, Michael D Twa, and Kirill V Larin, "*Air-pulse OCE for assessment of age-related changes in mouse cornea in vivo*", Laser Physics Letters, 2014, Volume 11, Issue 6.

3. **Jiasong Li**, Zhaolong Han, Manmohan Singh, Michael D Twa, and Kirill V Larin, "*Differentiating untreated and cross-linked porcine corneas of the same measured stiffness with optical coherence elastography*", Journal of Biomedical Optics 19.11 (2014): 110502-110502.

4. **Jiasong Li**, Chih-Hao Liu, Alexander Schill, Manmohan Singh, Achuth Nair, Valery P. Zakharov, and Kirill V. Larin, "*Assessing mechanical properties of tissue phantoms with non-contact optical coherence elastography and Michelson interferometric vibrometry*", Journal of Biomedical Photonics & Engineering, 1(4), 229-235, 2016.

5. Zhaolong Han, **Jiasong Li**, Manmohan Singh, Chen Wu, Chih-hao Liu, Shang Wang, Rita Idugboe, Raksha Raghunathan, Narendran Sudheendran, Salavat R Aglyamov, Michael D Twa and Kirill V Larin, "*Quantitative methods for reconstructing tissue biomechanical properties in optical coherence elastography: a*

comparison study", Physics in Medicine and Biology. 60 3531 (2015). (**Equal Contribution**).

6. Zhaolong Han, **Jiasong Li**, Manmohan Singh, Salavat R Aglyamov, Chen Wu, Chih-hao Liu, and Kirill V Larin, "*Analysis of the effects of curvature and thickness on elastic wave velocity in cornea-like structures by finite element modeling and optical coherence elastography*", Applied Physics Letters. 106(23) (2015). (**Equal Contribution**).

7. Manmohan Singh, **Jiasong Li**, Srilatha Vantipalli, Shang Wang, Zhaolong Han, Achuth Nair, Salavat R. Aglyamov, Michael D. Twa, and Kirill V. Larin, "*Noncontact Elastic Wave Imaging Optical Coherence Elastography (EWI-OCE) for Evaluating Changes in Corneal Elasticity due to Cross-Linking*", Journal of Selected Topics in Quantum Electronics, pp(99), 2015 (**Equal Contribution**).

8. Zhaolong Han, **Jiasong Li**, Manmohan Singh, Srilatha Vantipalli, Salavat R. Aglyamov, Chen Wu, Chih-hao Liu, Raksha Raghunathan, Michael D. Twa, and Kirill V. Larin, "*Analysis of the effect of the fluid-structure interface on elastic wave velocity in cornea-like structures by OCE and FEM*", Laser Physics Letters, 13(3), 035602, 2016 (**Equal Contribution**).

9. Manmohan Sing, **Jiasong Li**, Zhaolong Han, Chen Wu, Salavat R Aglyamov, Michael D. Twa, and Kirill V. Larin, "*Investigating elastic anisotropy of the porcine cornea as a function of intraocular pressure with optical coherence elastography*", Journal of Refractive Surgery (**Equal Contribution, accepted**).

10. Manmohan Singh, **Jiasong Li**, Zhaolong Han, Srilatha Vantipalli, Chih-Hao Liu, Chen Wu, Raksha Raghunathan, Michael D Twa, Salavat R Aglyamov, and Kirill

V Larin, "*Evaluating the effects of riboflavin/UV-A and rose-bengal/green light cross-linking of the rabbit cornea by noncontact optical coherence elastography*", Investigative Ophthalmology & Visual Science, (**Equal Contribution, accepted**).